UNIVERSITY OF SOUTHAMPTON

Sound transmission through panels and shells filled with porous material in the presence of external flow

by

Jie Zhou

A thesis submitted in partial fulfillment for the
degree of Doctor of Philosophy

in the
FACULTY OF ENGINEERING AND THE ENVIRONMENT

May 2014

UNIVERSITY OF SOUTHAMPTON

ABSTRACT

FACULTY OF ENGINEERING AND THE ENVIRONMENT
AERONAUTICS, ASTRONAUTICS AND COMPUTATIONAL ENGINEERING

Doctor of Philosophy

SOUND TRANSMISSION THROUGH PANELS AND SHELLS FILLED WITH POROUS MATERIAL IN THE PRESENCE OF EXTERNAL FLOW

by Jie Zhou

With increasingly tighter regulations on noise exposure during flight, aircraft designers have been compelled to innovate structures that minimise noise transmission into the cabin space. Porous material is widely used as a passive noise control medium because of their light weight, low cost, and broad band sound abatement effectiveness. The present work, inspired by the need to be able to predict noise transmission characteristics for commonly used constructions, incorporates the effect of flow into the calculations. Three types of sandwich configurations–bonded-bonded, bonded-unbonded and unbonded-unbonded–are considered. Biot's theory is used to simulate the poroelastic material.

The sound transmission though a double-walled panel lined with porous material in the presence of external mean flow is considered, first. The transmission loss is found to increase with increasing Mach number of the external mean flow. This is then explained on the basis that external mean flow increases the impedance of the panel. Mismatch in the characteristic acoustic impedances of the exterior and the interior results in the change of transmission loss. Transmission loss increases gradually when the pressure difference between air gap and that in the exterior decreases. A bi-objective optimization study is carried out to simultaneously minimize the sound transmission and the structural weight. The effect of laminated composite face plate in the structure is also brought out.

Sound transmission through a system of double shells, lined with poroelastic material in the presence of external mean flow, is studied next. The transmission characteristics of the sandwich construction are presented for different incidence angles and Mach numbers over a wide frequency range. It is noted that the transmission loss exhibits three dips on the frequency axis as opposed to flat panels where there are only two such frequencies. Results are discussed in the light of these observations. Flow is shown to decrease the transmission loss below the ring frequency, but to increase this above the ring frequency due to the reduction of stiffness and the damping effect added by the flow.

Finally, sound transmission through double-walled cylindrical shell lined with poroelastic material in the core excited by the exterior pressure fluctuation due to the turbulent boundary layer is investigated. The peaks of power spectral density of the inner shell kinetic energy due to shell resonance, hydrodynamic coincidence and acoustic coincidence are discussed. The results show that if the high frequency is interested, an air gap, even if very thin, between the two face shells provide superior sound insulation.

Contents

List of Figures

List of Tables

Nomenclature

Roman Symbols

A	Lame's constant
D	Bending stiffness of the plate
D_s	Membrane stiffness of the plate
e	Solid volumetric strain
E_f	Bulk modulus of elasticity of the fluid
E_s	Young's modulus of the solid
f	Frequency
f_c	Critical frequency
f_{co}	Coincidence frequency
f_f	Fundamental frequency
f_{hy}	Hydrodynamic coincidence frequencies
f_{sh}	Natural frequencies of the finite shell
h	Thickness
H_n^0	Hankel function of first kind of n order
H_n^1	Hankel function of second kind of n order
i	$=\sqrt{-1}$ Unit imaginary number
J_0	Bessel function of first kind of zero order

J_1	Bessel function of first kind of first order
k	Wave number
K_{eq}	Complex bulk modulus of porous material in rigid frame model
L	Length of the shell
L_j	Differential operators
M	Mach number
N	Shear modulus of the solid
N_{Pr}	Prandtl number of fluid medium
p	Sound wave pressure
Q	$= (1-\phi)E_f$ Coefficient in Biot's model
R	$= \phi E_f$ Coefficient in Biot's model
s	Parameter describes the changes in the viscosity of porous material
S_{EK}	Power spectral density of the total kinetic energy of the inner shell
Sh	Strouhal number
S_p	Cross spectral density of the pressure induced by a TBL
S_{pmn}	Modal power spectral density of TBL
$\mathbf{U}$	Displacement vector of fluid phase
$\mathbf{u}$	Displacement vector of solid phase
u	Displacement component
U_c	Convection velocity
U_∞	Free stream velocity
U_τ	Friction velocity
V	Velocity of external mean flow
v	Displacement component

w	Displacement component

Greek Symbols

α	Angle of incidence wave in the cylindrical system
α_c	Constant parameter in Corcos's model
α_e	Constant parameter in Efimtsov's model
α_∞	Tortuosity
β_c	Constant parameter in Corcos's model
β_e	Constant parameter in Efimtsov's model
δ	Boundary layer thickness
δ^*	Boundary layer displacement thickness
ϵ	Fluid volumetric strain
Λ	Characteristic viscous length
Λ'	Characteristic thermal length
ν	Poisson's ratio
ω	Circular frequency
ϕ	Porosity of the porous material
ϕ_1	Incident angle
Φ_p	Autospectrum of the wall pressure
Ψ_{mn}	Orthogonal basis functions
ρ_1	$= (1 - \phi)\rho_s$ Bulk density of solid phase
ρ_{12}	$= -\rho_a = \rho_2(1 - \varepsilon')$ Coupling coefficient
ρ_2	$= \phi\rho_f$ Bulk density of fluid phase
ρ_{eq}	Complex density of porous material in rigid frame model
ρ_f	Density of fluid phase

ρ	Density
ρ_s	Density of solid phase
σ_{ij}	Stresses of solid phase in the porous material
σ_f	Fluid pressure
τ	Transmission coefficient

Superscripts

$*$	Superscript denoting the complex conjugate
I, T	Superscripts denoting incidence side and transmission side

Subscripts

i, t	Subscripts denoting incidence side and transmission side
x, y, z	Subscripts denoting the coordinate directions

Other Symbols

∇	Vector differential operator

Acronyms

BB, BU, UU	Bonded-bonded, Bonded-unbonded, Unbonded-unbonded
MOP	Multiobjective optimization problem
PSD	Power spectral density
TBL	Turbulent boundary layer
TL	Transmission loss

Declaration of Authorship

I, Jie Zhou , declare that the thesis entitled 'Sound transmission through panels and shells filled with porous material in the presence of external flow' and the work presented in the thesis are both my own, and have been generated by me as the result of my own original research. I confirm that:

- this work was done wholly or mainly while in candidature for a research degree at this University;
- where any part of this thesis has previously been submitted for a degree or any other qualification at this University or any other institution, this has been clearly stated;
- where I have consulted the published work of others, this is always clearly attributed;
- where I have quoted from the work of others, the source is always given. With the exception of such quotations, this thesis is entirely my own work;
- I have acknowledged all main sources of help;
- where the thesis is based on work done by myself jointly with others, I have made clear exactly what was done by others and what I have contributed myself;
- parts of this work have been published as:
    1. Zhou, J., Bhaskar, A., Zhang, X., 2014. "Sound transmission though double cylindrical shells lined with porous material under turbulent boundary layer excitation". *Journal of Sound and Vibration* (to be submitted).

2. Zhou, J., Bhaskar, A., Zhang, X., 2014. ”The effect of external mean flow on sound transmission through double-walled cylindrical shells lined with poroelastic material”. *Journal of Sound and Vibration*, *333*(7), pp. 1972-1990.
3. Zhou, J., Bhaskar, A., Zhang, X., 2013. ”Sound transmission through a double-panel construction lined with poroelastic material in the presence of mean flow”. *Journal of Sound and Vibration*, *332*(16), pp. 3724-3734.
4. Zhou, J., Bhaskar, A., Zhang, X., 2013. ”Optimization for sound transmission through a double-wall panel”. *Applied Acoustics*, *74*(12), pp. 1422-1428.
5. Zhou, J., Bhaskar, A., Zhang, X., 2013. ”Sound transmission through sandwich shell constructions lined with poroelastic material”. 17th International Conference on Composite Structures.
6. Zhou, J., Bhaskar, A., Zhang, X., 2012. ”Sound transmission through laminated composite double-wall panel lined with poroelastic material”. ISMA 2012-International Conference on Noise and Vibration Engineering.
7. Zhou, J., Bhaskar, A., Zhang, X., 2012. ”Bi-objective optimization for the vibro-acoustic performance of a double-wall panel”. Acoustic 2012 Hong Kong.

Signed:..

Date:...

Acknowledgements

On a family level, I wish to thank my wife, for her contribution which is beyond words, and my little son was born in last December, for the great enjoyment and happiness he has brought to us. I would like to thank my mother, for all the love and supports from her.

I would like to thank my supervisors, Atul Bhaskar and Xin Zhang, who gave me an opportunity to study at the University of Southampton. Their valuable advice and supervision were major contributors to the achievement of my objectives. I appreciate their availability, insightful discussions and expertise shared. I thank them also for encouraging me to attend several international conferences. They gave me not only guidance on my PhD study, but also a big help for my living in Southampton. Additionally, I should thank for the useful discussion with Stephen Elliott of ISVR at University of Southampton and Paolo Gardonio in Università degli Studi di Udine.

Thanks to all my colleagues in our research group, for their help and friendly atmosphere that I have been shared. Some specific gentlemen include: Aditya Deshpande, who will be back UK and work in Rolls-Royce from April, always gave me programming advice; Sanjay Pant, who is now a postdoctoral at INRIA in France, discussed with me for the problems I have met in my study. Further, I would like to thank all my friends for their friendship in Southampton: Nanhang Dong, Zhuo Cao, Longtao Dong, Leran Wang, Xu Zhang, Fuyang Tao and many others.

Chapter 1

Introduction

Following the increase of link between regions and countries around the world, long-haul flights are becoming more frequent than those in the past. Since the cruise stage of aircraft operation constitutes a significant part of its flight envelope, maximizing travel comfort is a key goal of civil aircraft design. Aircraft interior noise induces fatigue to the passengers and the crew. In addition to the discomfort to passengers, a more serious impact of noise is on the pilot's ability to communicate and control the aircraft with maximum efficiency and attentiveness. Various measures of noise control must, therefore, be implemented. However, this usually results in penalties such as added structural weight, reduced cabin volume, or increased maintenance cost. The balance between the performance of noise control and the associated penalties is an area of continuing research [1].

1.1 Source of aircraft interior noise

Internal as well as external sources can contribute to aircraft interior noise. The main internal sources of noise are the Environmental Control System (ECS) or air distribution system (ADS) and avionics cooling system [2]. The external sources are generally classified into two types according to their transmission path [3]:

1. Airborne sources of noise:

   (a) Aerodynamic noise arises from the airflow around the aircraft fuselage, generally the turbulent boundary layer (TBL). It is a significant contributor to the mid and high frequency cabin sound pressure levels [4, 5].
   (b) Propeller noise can be characterized by discrete tones at the blade passage frequency (BPF) of the propeller or fan and its harmonics [6, 7].
   (c) Jet noise, primarily a broadband excitation, mainly originates from aircraft that have wing-mounted engines, and it affects the rear of the passenger cabin, particularly when the engines are mounted close to the fuselage [8, 9].

2. Structure-borne sources of noise:
   Structure-borne noise has its source in the vibration of the wings or other structural members of the aircraft. It is mainly caused by the imbalanced forces within the engine. This vibration energy propagates along structural paths into the aircraft where it causes vibration of various surfaces in the cabin and ultimately radiates noise [10].

1.2 Types of noise control

Reducing the aircraft interior noise level requires a system-level treatment technique that is designed to manage both the airborne noise and the structure-borne noise. In order to obtain the highest performance with minimal cost, the treatment requires not only a suitable choice of materials, but also an understanding of sound propagation and dissipation. Based on the existing literature, noise control systems can be divided in two large categories: passive control systems or active control systems.

1.2.1 Passive noise control

Passive noise control systems involve the reduction of noise levels without injecting energy into the system. The following material and method can be used for passive noise control: barriers (e.g. interior trim), absorption materials (e.g. foams, fibrous bats or blankets, acoustical tiles), damping materials (e.g. elastomeric composites, adhesive films) and vibration isolators (e.g. trim panel isolators, engine mounts). The first two categories deal with airborne noise, the noise already present in the environment.

The last two items deal with structure-borne noise, or vibration, which will appear as airborne noise after being radiated by a structure, unless it is either isolated or damped. In general, effective noise control measures make use of absorption as well as barriers for airborne noise and isolation as well as damping for structure-borne noise. Passive control systems are widely used because they are inexpensive, easy to implement and effective for broadband noise control, especially in the mid- and high-frequency range, as shown in Figure 1.1 [11].

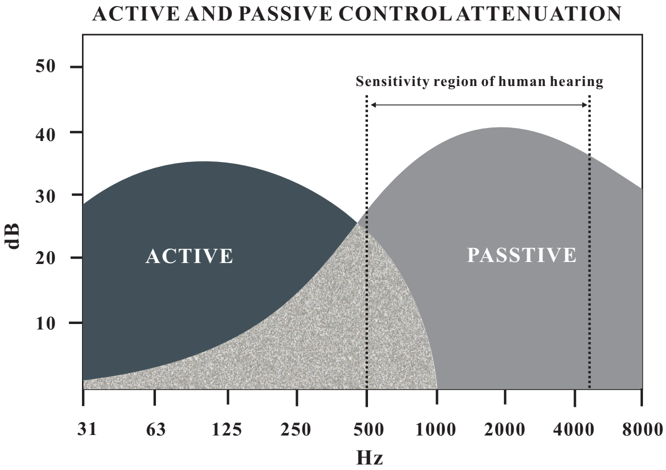

Figure 1.1: A sketch showing range of working frequencies for active and passive methods of vibration control [11].

Trim panel

Since, the interior trim panels were previously composed of either limp or light weight fabrics on thin-gauge aluminium panels, the critical frequency (at which the speed of bending wave propagation in the panel is equal to the speed of acoustic wave propagation in the surrounding medium at normal incidence of the trim panel) use to be very high [3]. With the development of composite material, the traditional aluminium fuselage is increasingly replaced by composite materials due to their light weight and high stiffness. Roussos et al. [12] experimentally and theoretically studied noise transmission characteristics of composite materials in aircraft fuselages to achieve a lower weight and more cost effective structure. Their results showed that composite general aviation panels had less transmission loss than an aluminium panel over most of the frequency range due to their lighter weight and lower critical frequencies. However, the composite panels could provide a better sound transmission loss than the conventional aluminium panels did with finite size.

Absorption materials

The absorbing materials, also known as poroelastics, are passive media that convert the acoustic energy into heat through a number of mechanisms. In porous materials at high frequencies, an adiabatic process takes place that produces heat due to friction when the sound wave transmits through the irregular pores. On the other hand, at low frequencies, poroelastic materials absorb sound by energy loss caused by heat exchange. This is an isothermal process. In general, poroelastic acoustic absorption efficiency is limited to high frequencies [13].

Typical absorption materials for an aircraft used to be fiberglass. Glass fibre blankets for aircraft insulation are usually encased in a polymeric film bagging material, because the glass fibre cannot hold the shape itself (see Figure 1.2). The density of the glass fibre bag is usually in the range from 5.4 to 24 kg/m^3. The glass fibre can provide optimum thermal and acoustical insulating performance for applications up to 230 °C [14]. However, the glass fibre possesses certain toxicity [15].

Figure 1.2: Fuselage panel added with bagged fiberglass blanket [16].

Polyimide foam was created in the early 1970s. It has superior properties, e.g. fire resistance, lightweight. It, initially, was only used in space vehicles due to the high cost of manufacture. Following the increase of manufacture technique and the economic control, it was put into application as insulation in commercial aircraft, aboard naval ships and submarines. Today, commercial appliance designers and manufacturers use the polyimide foam to replace the fiberglass or silica insulation products [17]. It has several advantages compared to normal insulation products like fiberglass which is widely used in the aircraft industry. Polyimide foams can withstand temperatures up to 300 to 400 °C and down to -250 °C, and even at -217 °C the material still stays flexible. Polyimide foams are also produced at low densities ranging from 3.2 to 16 kg/m^3. In industry, less weight means less fuel consumption and more payload, especially in the aerospace and aviation field. They can be modelled as any shape which results in lowered installation and maintenance costs (see Figure 1.3). The foam is non-flammable and non-toxic. Silcox et al. [18] pointed out that polyimide foam may offer an attractive alternative to other acoustic materials in certain situations.

Figure 1.3: AC-530 polyimide foam [19].

Damping materials

As shown in Figure 1.4, damping materials often consist of constrained layer damping tape with a viscoelastic adhesive and an aluminum backing layer. In order to reduce the skin vibration caused by boundary layer excitation, engine exhaust impingement and engine vibration, damping materials are typically attached directly to the aircraft skin. It is effective only at frequencies above the panel fundamental frequency, which can be relatively high for a pressurized, cylindrical fuselage [3]. If they are applied to the surfaces of the interior trim panel, the effect of airborne-induced vibration and engine vibration can be reduced. Generally, 50 to 75 percent coverage of the surface is considered to be effective [20]. The temperature is the key factor affecting the dynamic properties of damping materials during cruise of aircraft, because the loss factor of damping materials depends strongly on the temperature [3, 21].

Figure 1.4: Fuselage panel added with damping material [16].

A constrained-layer damping treatment, which consists of a sandwich of two outer elastic layers with a viscoelastic material as the core, works by creating shear deformation in the adhesive when the structure bends. However, there is very little shear deformation at lower order modes of the fuselage panel, and hence associated with very little damping can be provided by the damping material. To overcome this, one technique is the introduction of a spacer layer between the viscoelastic layer and the base structure as shown in Figure 1.5 [21]. Such a spacer layer could increase the strain in the damping material and, therefore, the damping. This spacer layer is called 'stand-off' layer and acts as a strain magnifier. The spacer material is supposed to ideally have infinite shear stiffness and zero bending stiffness. Figure 1.5 shows one method of avoiding this increase in flexural strength of the treated beam is to use 'slotted stand-off layer' of very high shear strength compared to the viscoelastic material.

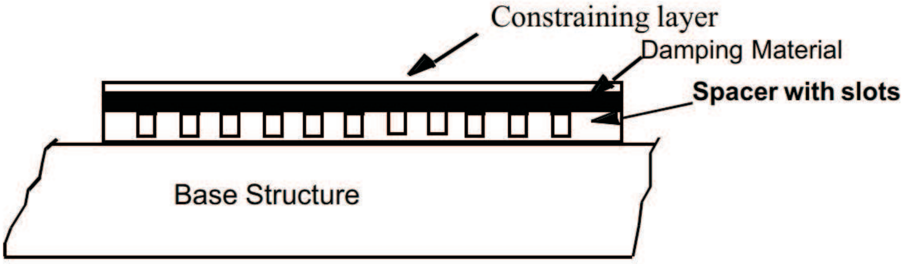

Figure 1.5: Stand-off layer damping system [21].

Vibration isolators

Vibration isolators are flexible components used to provide a means of connecting two structures so as to control relative motion between them under dynamic loads. Transmissibility is commonly used measure to quantify the performance of such isolators. It is defined as the ratio of the transmitted force to the input force under steady static harmonic loading as a function of frequency. Therefore, the lower transmissibility shows the better isolation performance. The main design criterion is that the isolator must be effective over the range of interest of frequencies. If the noise above 250 Hz is required to control, the mount should be a relatively stiff to have low-deflection response. Isolation of very low frequency vibration, such as the fundamental rotation speed of a jet engine at 125 Hz, requires the mount to be significantly soft in order to act as an isolator [20].

1.2.2 Active control

As shown in Figure 1.1, active noise control is mainly employed to reduce transmitted noise at low frequencies [2]. An active noise control includes sensors and actuators, which are mounted on the structure. However, the use of active control systems in aircraft should consider the following aspects: sufficient control authority (to achieve control objective), high bandwidth (frequency range) of operation, robust, inexpensive, low-power, efficient, accurate model for design, scaling, and control, broadband input, flat frequency response and linearity. Active control systems rely on acoustic and vibration actuators and sensors transducers, which often involve magnetic or piezoelectric components with inherent high masses. Normally these transducers have complex designs which involve the fabrication and assembly of many components which make them expensive and prone to durability issues. Also, these systems often rely on multi-channel controllers, which require expensive fast acting digital controllers and complex wiring systems to connect the sensors and actuators to the control unit [22]. This introduces additional weight issues and more importantly installation and maintenance costs. At the same time, it should be kept in mind that active systems can often be efficient in one area, but probably inefficient in another one.

1.3 Motivation and literature review

1.3.1 Motivation

Ozcan and Nemlioglu [23] measured the in-cabin noise in two Airbus A321 commercial passenger planes for a distance of 1,000 km for a 1 hour and 45 minutes flight duration. Continuous noise levels were seen to be 60-65 dB(A) prior to takeoff, and 70-85 dB(A) and 75-80 dB(A) during flight and landing, respectively, as shown in Figure 1.6. The noise generated by full-power engine operation during takeoff and by reverse thrust during landing can exceed levels during cruise, but the takeoff and landing phases are of sufficiently short duration that the passengers can accept the additional noise without undue discomfort. As the cruise portions of the flight are of relatively long duration, the associated noise levels must be controlled for a steady state level for passenger comfort. The most stringent requirements are usually associated with long flights that may last 12 to 16 hours [1]. Therefore, the flight condition should be considered for the design and analysis in the aircraft industry.

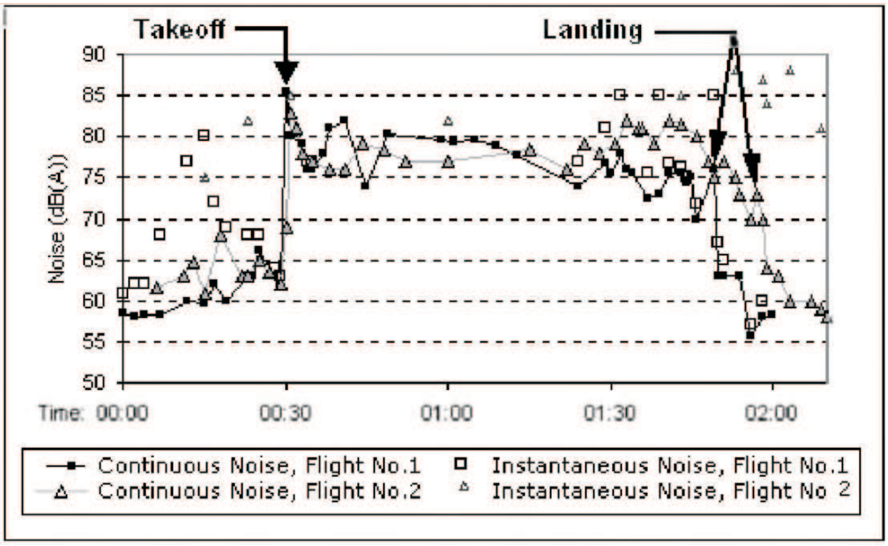

Figure 1.6: Fitted presentation of noise levels for both flights, referenced to takeoff stage [23].

However, the data on fuselage interior noise are generally collected through the ground tests, and then converted to in-flight conditions through simulation. In the ground tests, the excitation source cannot fully simulate the in-flight conditions. For flight tests, it is difficult to separate the transmitted exterior noise and interior noise source, because the number of sensors are limited. Analytical approaches provide a way to consider the flight condition. Although analytical methods only allow the study of simple constructions such as panels and cylindrical shells, they are still an important tool to use due to their inherent advantages [2] : (i) easy manipulation, (ii) a wide frequency range, and (iii) fast speed of calculation. This is the reason that analytical methods have been used for pre-design or parametric studies and the understanding of phenomena.

Almost all aircraft make exclusive use of passive methods to control interior noise. The basic noise control treatment frequently consists of one or more layers of porous material [3]. The goal of this research is to predict the aircraft interior noise caused by the airborne noise in order to make subsequent corrective action. Therefore, this work focus on predicting sound transmission through a sandwich structure in the presence of external flow.

1.3.2 Literature review

As shown in Figure 1.7, an aircraft fuselage is typically a double-walled cylindrical shell. It consists in an assembly of curved stiffened panels, made classically of aluminium, or more recently of Composite Fibre Reinforced Plastic. The panels are further stiffened in both directions by frames and stringers. The trim panel is indirectly connected with fuselage skin by stiffener and vibration isolator. The air gap between the fuselage skin and the trim panel is always filled by thermal and acoustical insulation materials.

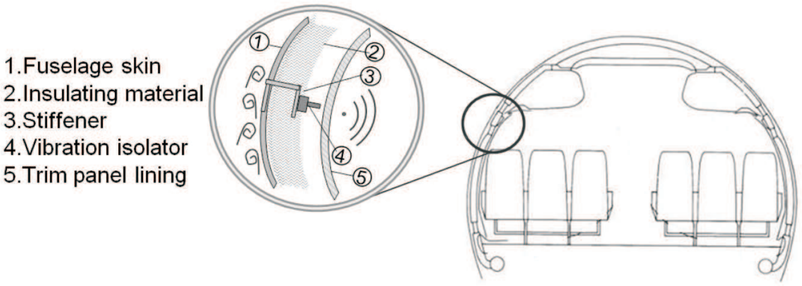

Figure 1.7: Aircraft sidewall panel components [24].

Sound transmission through such a double-walled panel system has been studied by many researchers in the past and the problem is of great current interest. London [25] addressed the problem of sound transmitted through two identical parallel plates and compared the theoretical results with experimental measurements in a reverberant sound field. Only the mass of the panels and their separation were considered in the model. Another model developed by Mulholland et al. [26] took into account the effect of sound-absorbing material in the cavity between two face plates, by introducing the reflection coefficient of the sound absorbing material, into account. Legault et al. [27] presented a model to consider the influence of trim mounts on the sound transmission of double panel structures. They found that the elastic mounts could reduce the structure-borne noise transmission when they are designed appropriately. Bolton et al. [28] built an analytical model to predict the sound transmission through flat double panels lined with poroelastic media in the absence of any mean flow while using Biot's model [29] for the porous material. Biot's model is a frequently used constitutive model for wave propagation in fluid-saturated porous material. Wang et al. [30] presented a theoretical model of sound transmission loss through double-leaf lightweight partitions stiffened with periodically placed studs by using a 'smeared method' and periodic structure theory. In this approach, the stiffness and the inertia effects are uniformly distributed and the structure is treated as an equivalent homogeneous continuum.

As mentioned above, the flight parameters should be considered in the analysis of the sound transmission through the fuselage. In an ideal case, an external mean flow with constant velocity can simulate the cruise condition. Ingard [31] investigated the effect of fluid motion past a plane boundary on the reflection and absorption of sound. Koval [32] studied the sound transmission loss through a single-walled panel in the diffuse sound field including the effect of external air flow, panel curvature and internal fuselage pressurization. Xin et al. [33] extended Koval's work [32] for the case of double-leaf plates for a prescribed angle of incidence with the external mean flow. Xin et al. [34] also built a model to account for the effects of mean flow on sound transmission through a simply supported rectangular aeroelastic panel. However, these studies do not consider the effect of porous material when external mean flow is present.

The flat plate model when used to simulate an aircraft cabin is not adequate, especially under flight conditions. Since the in-plane vibration is coupled with the transverse vibration for cylindrical shells structures. This will change the acoustic characteristics of the system. Koval [35–38] carried out a series of analytical studies which investigated sound transmitted into single walled cylindrical shells including the effect of external mean flow. Liu et al. [39] analyzed the sound transmission through curved, aircraft panels under the influence of overpressure at the concave side by using shallow shell theory. Lee et al. [40, 41] analyzed the sound transmission through single and double-walled cylindrical shells by using the acoustic wave equations and Love's theory of the thin shell vibration. The effect of some design parameters were also studied by them computationally. Tang et al. [42] used the thin and thick shell theories to compute sound transmission through a cylindrical sandwich shell with honeycomb core. They further extended the analysis to two concentric cylindrical sandwich shells in the presence of external mean flow but excluding the effect of any porous lining [43]. However, none of the studies cited above [35–43] consider any effect of such poroelastic lining in the presence of external mean flow. Liu et al. [44] used Donnel-Mushtari shell equations to study the effect of the thickness of the annular space and damping material on sound transmission through a double-walled cylindrical shell in the absence of the external flow.

The mean flow is an idealised condition to include the flow physics in the simplest possible way. In reality, the sound created from a turbulent boundary layer increases more rapidly with respect to the vehicle velocity, than other noise sources [45]. So in practice, in the cruise condition, the pressure fluctuation due to the turbulent boundary layer is the major contributor to the interior noise of an aircraft (see Figure 1.8). The TBL leads to the vibration response of the fuselage skin. Then the fuselage skin radiates noise into the aircraft.

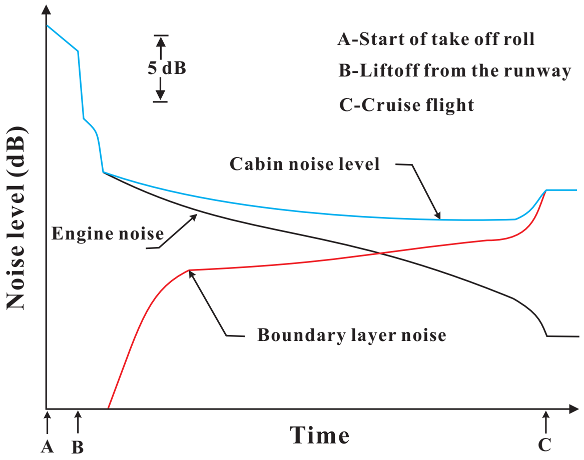

Figure 1.8: Typical variation of noise levels in airplane cabin during takeoff and climb to cruising altitude [46].

In the open literature, the analytical work of sound transmission through panels under turbulent boundary layer excitation can be classified into two main methods. The first method works in the space-frequency domain [47–51]. Alternative formulations are in the wavenumber-frequency domain [52–56]. These two methods are equivalent. Comparing with the wavenumber-frequency domain formulations, the former method is more intuitive to derive. In the wavenumber-frequency domain analysis, the spectral densities of the system response are expressed in terms of the spectral density of the turbulent excitation 'filtered' by the sensitivity function of the plate [52, 53, 57].

Most researchers have paid attention to the noise radiated by a single plate [47, 48, 52–56]. However, it is still quite far away from the real industrial problems. The analytical study based on the plate model neglects the curvature of the fuselage or the effect of the neighbouring panel and even both. The plate model is only suitable for describing the subsystem instead of the whole fuselage. For more accurate prediction, these effects need to be included. Therefore, the cylindrical geometry structure, which the real fuselage is, should be considered. Only a few studies focused on such geometry of the structure. Tang et al. [49] used the modal expansion analysis and Galerkin approach to develop an analytical model of sound transmission through cylindrical shell structures excited by a TBL. Gardonio [57] gave an introduction the general process for analyzing the interior noise in a cylindrical enclosure with a flexible thin wall caused by a TBL using Green's function.

However, in practice, the aircraft fuselage is not a single wall structure. It is a double wall system which consists of a skin panel and a trim panel with an annular space between them. Therefore, Tang et al. [50] extended their previous work [49] to predict the sound transmission into two concentric cylindrical sandwich shells subject to turbulent flow on the exterior surface of the outer shell. Unfortunately, Tang et al. [50] did not consider the effect of the porous lining in their study, which is widely used to control interior noise. Maury et al. [51] studied the case of sound transmission through a double-panel wall representative of an aircraft sidewall excited by a TBL. The effect of porous material filled in the air gap between the skin and trim panels was included by them. An empirical model [58] is used to model the porous material as equivalent fluid. Several active control approaches for reducing the interior noise were also developed and compared. Although the effect of the porous lining was considered, the plate model was used here in [51]. However, due to neglecting the frame waves in the fiberglass material, their result was not reasonable for the case when the fiberglass is directly bonded to both of the two face plates. This drawback is overcome in the current study. More details about the modelling of sound propagation in the porous material will be discussed in the next chapter.

The literature review reveals that, only one article [51] considered the effect of porous material and external flow in a model. Unfortunately, their model is not accurate in some cases due to the reason mentioned above. In order to build an accurate model to predict interior noise in aircraft, this work will investigate the sound transmission through a double-walled panel lined with porous material in the presence of external flow.

1.4 Organization of Thesis

The thesis is organized as follow. Chapter 2 describes and compares the existing models of sound propagation in porous materials. In Chapter 3, an analytical model of sound transmission characteristics through flat double-walled panel lined with poroelastic material in the presence of external mean flow is developed. The effects of Mach number, the pressure in the air gap and the laminated composite face plate are brought out. A bi-optimization is also carried out in this chapter. As the flat panel model can only simulate the subsystem–fuselage sidewall, for whole cabin simulation, the cylindrical shell system should be considered. Therefore, in Chapter 4, the effect of external mean flow on sound transmission through cylindrical shells line with porous material is studied. The turbulent boundary layer, in fact, will be the dominant noise source of interior noise in the cabin due to the increase of external flow velocity. Chapter 5 will give the effect of such a factor. The sound transmission through cylindrical shell lined with porous material under turbulent boundary layer excitation is analysed here. Finally, the conclusions and the plan for the future work are presented in Chapter 6.

Chapter 2

Models of the acoustics of porous materials

2.1 Description of porous material

Porous material is a material containing pores (voids). The skeletal portion of the material is often called the walls or frames. The pores are typically filled with a fluid (liquid or gas). The skeletal material is usually a solid, but structures like foams are frequently treated as porous media to be analyzed. Generally, the porous material can be divided into two groups: open-celled foam and closed-celled foam (see Figure 2.1a and 2.1b respectively). Open-celled foams contain the struts, while the closed-celled foams are made of faces and each cell is sealed off from its neighbours [59].

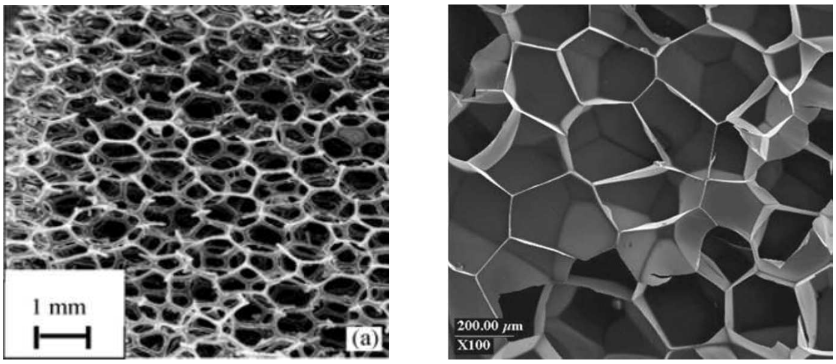

(a) Open-celled foam [60]

(b) Closed-celled foam [61]

Figure 2.1: The scanning electron microscope image of the foams.

As a complex structural material, porous materials need various parameters to describe their properties. Some important parameters specific to the acoustics of porous media in addition to well known elasticity parameters such as Young's modulus, Poisson's ratio, loss factor etc. will be discussed next.

2.1.1 Porosity

The porosity ϕ is the ratio of the air volume V_a to the total volume of the porous material V_T defined as [62]

$$\phi = V_a/V_T. \tag{2.1}$$

If V_b represents the volume of the frame, the relation between the three volumes is

$$V_a + V_b = V_T. \tag{2.2}$$

In the air volume V_a, only the volume not restrained in the frame is considered, and therefore the closed pores in the frame are associated with the volume of the frame V_b. The value of porosity ranges between 0 and 1. For absorbing materials, e.g. fibrous materials and polymer foams, it lies in the range 0.95 to 0.99.

The porosity can be measured by using the methods proposed by Champoux et al. [63]. The idea is based on the Boyle's law. As shown in Figure 2.2, the porous material is placed into a sealed chamber. The residual volume in the chamber is denoted by V_0. Initially, the pressure in the chamber is P_0. The piston produces the changes in the pressure and the volume in the chamber ΔP and ΔV, respectively. According to the Boyle's law, the product of the pressure and volume is constant so that

$$P_0(V_a + V_0) = (P_0 + \Delta P)(V_a + V_0 + \Delta V). \tag{2.3}$$

The air volume V_a of the porous material is deduced from Eq. (2.3) as

$$V_a = -\left(\frac{P_0 + \Delta P}{\Delta P}\Delta V + V_0\right). \tag{2.4}$$

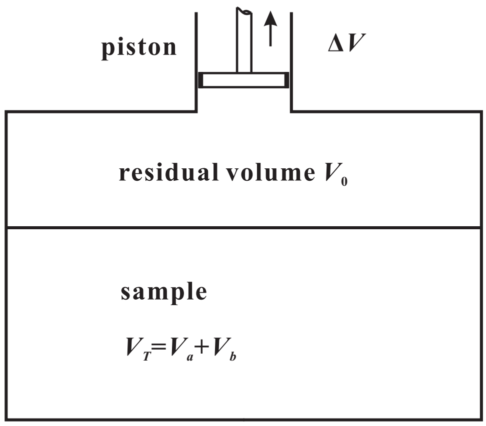

Figure 2.2: The principle of operation of an idealized system for measuring porosit [63].

The porosity can now be obtained by substituting Eq. (2.4) into Eq. (2.1).

2.1.2 Flow resistivity

Flow resistivity indicating the absorptive ability of a material can be obtained by evaluating the ratio of the static pressure drop ΔP to the normal flow velocity through the material. Flow resistivity σ is given by [62]

$$\sigma = \Delta P/Vh, \tag{2.5}$$

where the quantities V and h denote the mean flow of air per unit area of material and the thickness of the material, respectively. The unit of flow resistance is $\mathrm{N \cdot s/m^4}$ or Rayls/m. The flow resistivity of fibreglass and open-celled foams generally lies between 1000 and 100000 $\mathrm{N \cdot s/m^4}$ [62]. The technique of the measurement is presented in the book written by Bies and Hansen [58].

2.1.3 Tortuosity

Tortuosity, α_∞, sometimes called geometrical structure factor, is the indicator of the non-straightness of the pores inside the porous material. If the pores are straight and uniform, the tortuosity will equal unity; it increases as the pores become more tortuous.

As shown schematically in Figure 2.3 shown, a porous material has cylindrical pores with radius R at an angle of φ with respect to the normal to the surface. The porosity in a porous material with n pores per unit area of surface is given by [62]

$$\phi = \frac{n\pi R^2}{\cos\varphi}. \tag{2.6}$$

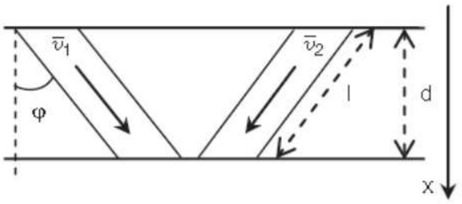

Figure 2.3: A porous material with cylindrical pores at an angle of φ with respect to the normal of the surface [62].

In the x direction, the flow resistivity σ is given by

$$\sigma = \frac{8\eta}{n\pi R^2 \cos\varphi}, \tag{2.7}$$

where η is the shear viscosity. Considering the expression of porosity in Eq. (2.6), the flow resistivity σ can be rewritten as

$$\sigma = \frac{8\eta}{\phi R^2 \cos^2\varphi}. \tag{2.8}$$

The parameter s, describes the changes in the viscosity, is given by [13, 62]

$$s = \left(\frac{8\omega\rho_0}{\sigma\phi\cos^2\varphi}\right)^2, \tag{2.9}$$

where ω is circular frequency and ρ_0 is the fluid density in the porous material. Here, the quantity $1/\cos^2\varphi$ is defined as the tortuosity of the material. If the porous material is not conductive, we can measure the tortuosity by saturating the material with an electrically conducting fluid and measuring the electrical resistivity of the saturated sample, R_s, and comparing with the resistivity of the fluid itself, R_f. The tortuosity can then be obtained as [13, 62]

$$\alpha_\infty = \phi\frac{R_s}{R_f}. \tag{2.10}$$

2.1.4 Characteristic lengths

Characteristic lengths include the characteristic viscous length Λ and the characteristic thermal length Λ'. The former, the viscous characteristic length, describes the effects of viscosity at high frequencies. Johnson et al. [62, 64] defined the viscous length Λ as

$$\Lambda = 2\frac{\int_V v_i^2(r)dV}{\int_A v_i^2(r_w)dA}, \tag{2.11}$$

where $v_i(r_w)$ is the velocity of the fluid on the pore surface, and the $v_i(r)$ is the velocity inside the pores. A represents the surface area of the pores; V denotes the volume of the pores. The parameter Λ given by Eq. (2.11) only depends on the geometry of the frame [62].

The thermal characteristic length describes the effects of thermal dissipation at high frequencies. The value of the characteristic thermal length is twice the ratio of volume to surface area, $2V/A$, in the pores. If the cylindrical pores are identical in the material, the two characteristic lengths will be equal to each other [62].

2.2 Empirical model

Delany and Bazley [65] developed a simple empirical model of the acoustic impedance of porous material based on its flow resistivity. They gave the expressions of the characteristic impedance Z_c and the complex wavenumber k_c for a large range of frequencies in many fibrous materials with porosity from 0.95 to 0.99. The empirical expressions which fit to experimental measurements are given by [62]

$$Z_c = \rho_0 c_0(1 + 0.0571\chi^{-0.754} - j0.087\chi^{-0.732}) \tag{2.12}$$

$$k_c = \frac{\omega}{c_0}(1 + 0.0978\chi^{-0.7} - j0.189\chi^{-0.595}), \tag{2.13}$$

where the non-dimensional parameter χ is defined as

$$\chi = \frac{\rho_0 f}{\sigma}, \tag{2.14}$$

where ρ_0 and c_0 are the density and sound speed of fluid in the absence of the porous material. Delany and Bazley suggested that the two expressions are valid over the range $0.01 < \chi < 0.1$. Bies and Hansen [58] provided a formulation to extend both the low and high frequency ranges for any value of χ. The impedance Z_c and the complex wavenumber k_c were given as

$$Z_c = \rho_0 c_0 (1 + C_1 \chi^{-C_2} - jC_3 \chi^{-C_4}) \tag{2.15}$$

$$k_c = \frac{\omega}{c_0}(1 + C_5 \chi^{-C_6} - jC_7 \chi^{-C_8}). \tag{2.16}$$

The values of the constants C_1-C_8 were listed by Bies and Hansen [58] for various materials.

Porous material come in many forms, so it is not expected that a single expressions will provide an accurate prediction of acoustic behaviour of all the porous material. Bies and Hansen [66] showed that for fibrous materials, the flow resistivity adequate to describe impedance, but the flow resistivity was in turn a linear function of bulk density. However, empirical models do not fully describe the dynamics of the materials, so the accuracy of any detailed design or optimization of the absorption and transmission properties of the materials is limited.

2.3 Wave propagation models within porous material with rigid frame

In 1868, Kirchhoff proposed a theory of sound propagation in cylindrical tubes including the effects of the viscosity and thermal conductivity of the air. However, if the cross section is non-circular, the fundamental equations used by Kirchhoff are very difficult to solve [62]. Zwikker and Kosten [67] used this theory only in a narrow frequency range and a narrow radius range. Therefore, viscous and thermal effects can be treated separately using a complex mass density and a complex bulk modulus (in some references known as 'compressibility modulus') properties denoted as ρ_{eq} and K_{eq} respectively. The wave propagation equation for the compressive waves in the porous material is given by [62]

$$\nabla^2 p + \omega^2 \frac{\rho_{eq}}{K_{eq}} p = 0, \tag{2.17}$$

where p is the pressure in the porous material. The complex mass density $\rho_{eq} = \rho/\phi$ and the complex bulk modulus $K_{eq} = K/\phi$ are functions of frequency and of the pore shape. The goal of the rigid frame model is to define the two parameters, ρ_{eq} and K_{eq}, in Eq. (2.17). These models are known as equivalent fluid models.

2.3.1 Analytical models

For porous materials that have the simple structures, e.g. parallel cylindrical pores with a regular cross-section (circle, square, equilateral triangle, rectangular slit), analytical expression of ρ and K can be obtained. Two analytical models are presented next.

If the pore in the material is cylindrical with a circular cross-section of radius R and normal to the surface of the material, then the expressions of the ρ and K respectively is given by [62, 67]

$$\rho = \rho_0 \left\{ 1 - (2/s\sqrt{-i}) T_c[s\sqrt{-i}] \right\}^{-1} \tag{2.18}$$

$$K = \gamma P_0 \left\{ 1 + (\gamma - 1)(2/N_{\mathrm{Pr}}^{1/2} s\sqrt{-i}) T_c[N_{\mathrm{Pr}}^{1/2} s\sqrt{-i}] \right\}^{-1}, \tag{2.19}$$

where P_0 is the ambient mean pressure, γ is the ratio of specific heats, $i = \sqrt{-1}$, N_{Pr} is the Prandtl number of fluid medium and $s = (8\omega\rho_0/\phi\sigma)^{1/2}$. $T_c[s\sqrt{-i}] = J_1[s\sqrt{-i}]/J_0[s\sqrt{-i}]$, where J_0 and J_1 are Bessel functions of first kind of zero and first order, respectively.

If the cross-section of the cylindrical pores is of a slit shape with width $2a$, then ρ and K take the following form

$$\rho = \rho_0 \left\{ 1 - (1/s'\sqrt{i}) \tanh(s'\sqrt{i}) \right\}^{-1} \tag{2.20}$$

$$K = \gamma P_0 \left\{ 1 + (\gamma - 1) \frac{\tanh(N_{\mathrm{Pr}}^{1/2} s'\sqrt{i})}{N_{\mathrm{Pr}}^{1/2} s'\sqrt{i}} \right\}^{-1}. \tag{2.21}$$

Here s' in Eqs. (2.20) and (2.21) equals $(3\omega\rho_0/\phi\sigma)^{1/2}$.

2.3.2 Semi-phenomenological models

As shown in Figure 2.1, the microstructure of the porous material is very complex. The models based on idealised geometry, e.g. cylindrical pores with regular cross-section mentioned above, is often inadequate to give accurate prediction of the sound propagation in the porous material. It is impossible to consider all the geometrical information of the microstructure in an analytical study of sound propagation in porous material. Therefore, the models that study sound propagation through porous material are mostly phenomenological and provide a continuum description of the material representing effective properties [62].

Johnson-Champoux-Allard model

Johnson et al. [64] derived the dynamic tortuosity $\alpha(\omega)$ of a rigid isotropic porous medium saturated with a Newtonian fluid by using the viscous characteristic length Λ. The effective density based on this dynamic tortuosity is given by [62, 64]

$$\rho = \rho_0 \alpha(\omega) = \rho_0 \alpha_\infty \left[1 + \frac{\sigma\phi}{j\omega\rho_0\alpha_\infty} \sqrt{1 + j\frac{4\alpha_\infty^2 \eta \rho_0 \omega}{\sigma^2 \Lambda^2 \phi^2}} \right]. \tag{2.22}$$

Champoux and Allard [68] involved the thermal characteristic length and obtained the effective bulk modulus by using the dynamic tortuosity $\alpha'(\omega)$. The expression of K is [62]

$$\begin{aligned} K &= P_0 / \left(1 - \frac{\gamma - 1}{\gamma \alpha'(\omega)} \right) \\ &= \gamma P_0 \left\{ \gamma - (\gamma - 1) \left[1 + \frac{\sigma\phi}{j N_{\mathrm{Pr}} \omega \rho_0 \alpha_\infty} \sqrt{1 + \frac{4\alpha_\infty^2 \eta \rho_0 \omega N_{\mathrm{Pr}}}{\sigma^2 \Lambda'^2 \phi^2}} \right]^{-1} \right\}^{-1}. \end{aligned} \tag{2.23}$$

Champoux and Allard [68] pointed out that this model did not describe the exact behaviour of the dynamic tortuosity as ω tends to zero. The real part of the dynamic tortuosity is not correct at low frequencies.

Pride and Lafarge model

Considering the limitations of the model of Johnson et al. [64], Pride et al. [69] modified the dynamic tortuosity with a parameter b as [62]

$$\alpha(\omega) = \frac{\nu\phi}{j\omega q_0}\left\{1 - b + b\left[1 + \left(\frac{2\alpha_\infty q_0}{b\phi\Lambda}\right)^2 \frac{j\omega}{\nu}\right]^{1/2}\right\} + \alpha_\infty \tag{2.24}$$

where $\nu = \eta/\rho_0 = N_{\mathrm{Pr}}\nu'$. $q_0 = \eta/\sigma$ is the static viscous permeability. The parameter b is expressed in terms of α_0, which is the limit of α_ω when ω is reduced towards 0, as

$$b = \frac{2q_0\alpha_\infty^2}{\phi\Lambda^2(\alpha_0 - \alpha_\infty)}. \tag{2.25}$$

Similarly, Lafarge et al. [70] derived the dynamic tortuosity to express the dynamic thermal permeability. The resulting expression is given by [62]

$$\alpha'(\omega) = \frac{\nu'\phi}{j\omega q_0'}\left\{1 - b' + b'\left[1 + \left(\frac{2q_0'}{b'\phi\Lambda'}\right)^2 \frac{j\omega}{\nu'}\right]^{1/2}\right\} + 1. \tag{2.26}$$

If a porous medium with circular cylindrical pores having a radius $R = \Lambda'$, the thermal static permeability $q_0' = \phi\Lambda'^2/8$, then the effective density and the bulk modulus are obtained as

$$\rho = \rho_0\alpha(\omega) \tag{2.27}$$

$$K = P_0 \Big/ \left(1 - \frac{\gamma - 1}{\gamma\alpha'(\omega)}\right). \tag{2.28}$$

2.4 Biot's model

If the porous material is used as a lining between two elastic walls, the frames in the porous material will vibrate upon external excitation. The rigid frame models mentioned above are not valid for such a case. In his seminal paper, Biot [29] took a fresh approach to build constitutive model for wave propagation in fluid-saturated poroelastic material. This model is derived based on the following assumptions [71]:

(a). The medium is statistically isotropic, quasi-homogeneous and that the porosity is uniform throughout;

(b). The wavelength of interest is very much larger than the pore size;

(c). Scattering, in the sense of diffraction around individual grains or particles can be ignored;

(d). Pore walls are impervious and the pore size is concentrated around an average value.

The wave propagation equations for the porous material with dissipation effect as proposed by Biot [29] are given by the following pair of coupled partial differential equations

$$N\nabla^2\mathbf{u} + \mathrm{grad}[(A+N)e + Q\epsilon] = \frac{\partial^2}{\partial t^2}(\rho_{11}\mathbf{u} + \rho_{12}\mathbf{U}) + b\frac{\partial}{\partial t}(\mathbf{u} - \mathbf{U}) \tag{2.29}$$

$$\mathrm{grad}[Qe + R\epsilon] = \frac{\partial^2}{\partial t^2}(\rho_{12}\mathbf{u} + \rho_{22}\mathbf{U}) - b\frac{\partial}{\partial t}(\mathbf{u} - \mathbf{U}). \tag{2.30}$$

In Eqs.(2.29) and (2.30), $e = \nabla \cdot \mathbf{u} = e_x + e_y + e_z$ which is the volumetric strain of solid phase and $\mathbf{u} = (u_x, u_y, u_z)$ is the displacement vector of solid phase; $\epsilon = \nabla \cdot \mathbf{U}$ is the fluid volumetric strain and $\mathbf{U} = (U_x, U_y, U_z)$ is the displacement vector of fluid phase; $N = E_s/[2(1+\nu)]$ is the shear modulus of the solid, and $A = \nu E_s/[(1+\nu)(1-2\nu)]$ is the Lame's constant (E_s is the Young's modulus of the solid and ν is the Poisson's ratio); the coefficient Q equals $(1-\phi)E_f$ which represents the coupling between the volume change of the solid and that of the fluid; the coefficient R equals ϕE_f measuring the pressure on the fluid to keep the total volume constant. ϕ is the porosity of the porous media. E_f is the bulk modulus of elasticity of the fluid in the pores. $\rho_{11} = \rho_1 + \rho_a$ is the total effective mass of the solid and $\rho_{22} = \rho_2 + \rho_a$ is the total effective mass of the fluid where $\rho_{12} = -\rho_a$ is a coupling coefficient ($\rho_1 = (1-\phi)\rho_s$ is the solid mass of unit volume of porous material, and $\rho_2 = \phi\rho_f$ is the fluid mass of unit volume of porous material where ρ_s and ρ_f are the densities for the solid and fluid, respectively); the coefficient b equals $\mu\phi^2/k$ where μ is the fluid viscosity and k is Darcy's coefficient of permeability.

It should be noted that the parameter b here is not the same as that in Eq. (2.24) of the rigid frame model mentioned previously. The relevant solid stress components σ_{ij} and fluid pressure s are

$$\begin{aligned} \sigma_{ij} &= 2Ne_{ij} + (Ae + Q\epsilon)\delta_{ij} \qquad (i, j = 1, 2, 3) \\ s &= Qe + R\epsilon, \end{aligned} \tag{2.31}$$

where δ_{ij} is the Kronecker delta.

Applying the divergence operation to Eqs.(2.29) and (2.30), we obtain

$$\nabla^2(Pe + Q\epsilon) = \frac{\partial^2}{\partial t^2}(\rho_{11}e + \rho_{12}\epsilon) + b\frac{\partial}{\partial t}(e - \epsilon) \tag{2.32}$$

$$\nabla^2(Qe + R\epsilon) = \frac{\partial^2}{\partial t^2}(\rho_{12}e + \rho_{22}\epsilon) - b\frac{\partial}{\partial t}(e - \epsilon) \tag{2.33}$$

with the definition $P = A + 2N$. These two equations govern the propagation of two dilatational waves: a fast wave and a slow wave. Generally, the two compression waves are classified as a frame-borne wave and an airborne wave. The airborne wave mainly propagates in the air of the pore space, while the frame borne wave propagates in both of the frame and air of the pores [62].

Similarly, applying the curl operation to Eqs.(2.29) and (2.30), we obtain

$$\frac{\partial^2}{\partial t^2}(\rho_{11}\boldsymbol{\omega} + \rho_{12}\boldsymbol{\Omega}) + b\frac{\partial}{\partial t}(\boldsymbol{\omega} - \boldsymbol{\Omega}) = N\nabla^2\omega \tag{2.34}$$

$$\frac{\partial^2}{\partial t^2}(\rho_{12}\boldsymbol{\omega} + \rho_{22}\boldsymbol{\Omega}) - b\frac{\partial}{\partial t}(\boldsymbol{\omega} - \boldsymbol{\Omega}) = 0 \tag{2.35}$$

where $\boldsymbol{\omega} = \nabla \times \mathbf{u}$ and $\boldsymbol{\Omega} = \nabla \times \mathbf{U}$. These equations govern the propagation of pure rotational waves. It is obvious that the rotation of the solid and the rotation of fluid are coupled. The shear wave, another kind of frame borne wave, is very similar to the shear wave propagating in the frame when in vacuum [62].

Atalla et al. [72] rewrote the Biot's equations Eqs.(2.29) and (2.30) as the mixed displacement pressure formulations. The fluid phase equation is given by

$$\nabla^2 p + \frac{\rho_{22}^*}{R}\omega^2 p + \frac{\rho_{22}^*}{\phi^2}\gamma^* \omega^2 e = 0 \tag{2.36}$$

where the equivalent density is given by $\rho_{22}^* = \rho_{22} + b/i\omega$. The coefficient $\gamma^* = \phi(\rho_{12}^*/\rho_{22}^* - Q/R)$. If the frame is rigid, the displacements of the solid phase $\mathbf{u}$ and the related volume strain e will equal zero. Therefore, the Eq. (2.36) can be deducted as

$$\nabla^2 p + \omega^2 \frac{\rho_{22}^*}{R} p = 0. \tag{2.37}$$

Comparing the above with the Eq. (2.17), the equivalent density $\rho_{eq} = \rho_{22}^*/\phi$, and equivalent bulk modulus $K_{eq} = R/\phi$, it can be calculated that the rigid frame model is the special case of the Biot's model without considering the wave propagation in the solid phase.

2.5 Summary

The empirical model, the rigid frame model and the Biot's model of sound wave propagation in porous material were presented in this chapter. The empirical model estimates the impedance and the complex wave number of the porous material in view of the experimental measurements. It is still widely used due to its simplicity. Only the flow resistance σ is needed to describe the acoustic behaviour of the porous material. The empirical model gives a good prediction in the broad band trend, but it still cannot predict the resonant behaviour of foam layers [73]. The rigid frame model gives reasonable description of sound wave propagation in the material when its frame is motionless. This model only can be used at the frequencies which are higher than the decoupling frequency, $F_d = \sigma \times \phi^2/(2\pi\rho_1)$, because the interaction between the solid and the fluid phase is very weak in this frequency range. There also exists another restriction that, if the porous material is directly bonded to a vibrating structure, the rigid frame model cannot be used [62]. It is now generally accepted that Biot's description of the dynamics of poroelastic material is perhaps the most accurate model available. Since fewer assumptions are required, it yields accurate solutions to predict the acoustic and structural response of poroelastic material. As a result of this, Biot's model has been applied in many diverse fields including acoustics [74, 75], geo-mechanics [76, 77] and bio-dynamics [78, 79]. However, Biot's model (poroelastic model) not only makes use of the parameters used in the rigid frame models (porosity, tortuosity, air flow resistivity, thermal and viscous characteristic lengths), but also includes the parameters of the skeleton in the porous material (Young's modulus, Poisson's ration, shear modulus and damping) [13]. Therefore, the implementation of Biot's model is far more complicated than the other models (empirical model and rigid frame model).

Chapter 3

Sound transmission through flat double-walled panel

A fuselage consists in an assembly of stiffened panels, often made of aluminium alloys, and the interior trim panels. An air gap is formed between the two panels. The shape of the fuselage is one of a shell. A simple abstraction to study the transmission of sound through double-walled panels is one of flat infinite geometry. This chapter focuses on a simplified geometry of flat double-walled panel lined with porous material, to understand the effect of external flow on the sandwich structure. The curvature effects of the fuselage will be considered in Chapter 4. A bi-objective optimization of a double-walled panel is also carried out for simultaneously minimizing weight while maximizing the acoustic transmission loss.

3.1 Description of the system

The model considered consists of two infinite parallel plates that are homogeneous and lined with poroelastic material as shown in Figure 3.1. A plane pressure wave transmits through the system from the external mean flow side into the interior (having a stationary fluid medium). The flow is assumed to align with the x-axis and has a constant velocity V. This, of course, is a simplification because the velocity profile will have a significant gradient in the boundary layer. However, we ignore this higher order effect to sound propagation in the present work. Disregarding the boundary layer effect is common in many simple theories of sound transmission [32, 33, 42, 43]. The angle between the incident pressure wave and the $x - y$ plane is φ_1 and the projection of the normal to the incident and reflected wavefront, in the $x - y$ plane, makes an angle θ with x-axis. Similarly, the angles in the transmitted region are φ_t and θ, respectively. The fluid medium on the incident side and the transmitted side have the density and the speed of sound given by (ρ_i, c_i) and (ρ_t, c_t), respectively.

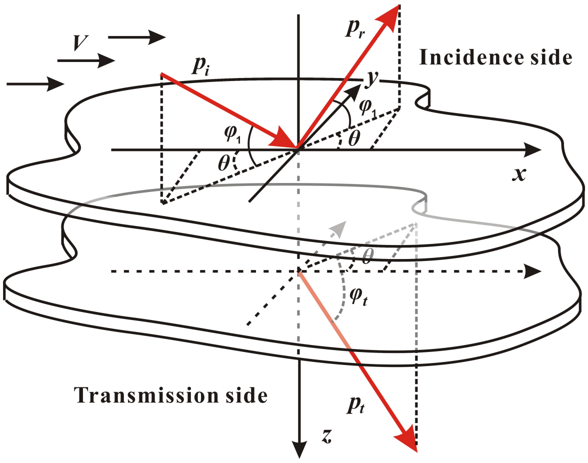

Figure 3.1: A sketch of the sound wave transmission through the double-panel system. The porous material lining is not shown here.

In the region of the external flow, the pressure can be written as harmonic function of space and time using the complex exponential notation as

$$p_1 = p_i + p_r = P_i e^{i\omega t - i(k_{1x}x + k_{1y}y + k_{1z}z)} + P_r e^{i\omega t - i(k_{1x}x + k_{1y}y - k_{1z}z)}, \tag{3.1}$$

where p_i is the incident pressure, p_r is the reflected pressure (P_i and P_r are the amplitudes), ω is the circular frequency and $i = \sqrt{-1}$. The wave number components are $k_{1x} = k_1 \cos\varphi_1 \cos\theta$, $k_{1y} = k_1 \cos\varphi_1 \sin\theta$ and $k_{1z}^2 = k_1^2 - (k_{1x}^2 + k_{1y}^2)$, where k_1 is the wave number in the exterior which accounts for the mean flow in the region—this can be related to the mean flow Mach number and the parameters of the problem. Pressure p_1 satisfies the wave equation which includes the convection term $\mathbf{V} \cdot \nabla$ and is given by

$$\frac{D^2 p_1}{Dt^2} = \left(\frac{\partial}{\partial t} + \mathbf{V} \cdot \nabla\right)^2 p_1 = c_i^2 \nabla^2 p_1 \tag{3.2}$$

where $\mathbf{V} = V\vec{i}$ is the external flow velocity vector in the x-direction. Therefore Eq. (3.2) can be simplified further as

$$\left(\frac{\partial}{\partial t} + V\frac{\partial}{\partial x}\right)^2 p_1 = c_i^2 \nabla^2 p_1. \tag{3.3}$$

Substituting Eq. (3.1) into Eq. (3.3), we obtain

$$k_1 = \omega(c_i + V\cos\theta\cos\varphi_1)^{-1} = k_1^*(1 + M\cos\theta\cos\varphi_1)^{-1} \tag{3.4}$$

where $k_1^* = \omega/c_i$ is the wave number in the stationary medium and $M = V/c_i$ is the Mach number of the external flow.

The speed of the trace wave, which is the structural wave propagating parallel to the plane of the plate, in the plate is represented by c_p, so that the trace wave number is given by $k_p = \omega/c_p = 2\pi/\lambda_p$, where λ_p is the wavelength of the panel trace wave. The transverse displacements of the two plates induced by the incident sound can be expressed as a travelling wave in the form

$$w_1 = W_1 e^{i\omega t - i(k_{1p}\cos\theta)x - i(k_{1p}\sin\theta)y} \tag{3.5}$$

$$w_2 = W_2 e^{i\omega t - i(k_{2p}\cos\theta)x - i(k_{2p}\sin\theta)y} \tag{3.6}$$

where W_1 and W_2 are the corresponding amplitudes.

Similarly, the transmitted pressure can be expressed as

$$p_t = P_t e^{i\omega t - i(k_{tx}x + k_{ty}y + k_{tz}z)}, \tag{3.7}$$

where P_t is the amplitude of transmitted wave pressure. The wave number components are $k_{tx} = k_t\cos\varphi_t\cos\theta$, $k_{ty} = k_t\cos\varphi_t\sin\theta$ and $k_{tz}^2 = k_t^2 - (k_{tx}^2 + k_{ty}^2)$, respectively. Here, the transmitted wave number k_t equals ω/c_t.

3.2 Wave propagation in porous material

In Chapter 2, three kinds of models for sound propagation in the porous materials were discussed. Due to the greater accuracy of Biot's model than that of the other two, Biot's model will be used here. The governing equations for the two dilatational waves and the rotational wave in the porous material are given by

$$\nabla^2(Pe+Q\epsilon)=-\omega^2(\rho_{11}^*e+\rho_{12}^*\epsilon),\ \nabla^2(Qe+R\epsilon)=-\omega^2(\rho_{12}^*e+\rho_{22}^*\epsilon),\text{and} \tag{3.8}$$

$$-\omega^2(\rho_{11}^*e+\rho_{12}^*\epsilon)=N\nabla^2\boldsymbol{\omega},\ -\omega^2(\rho_{12}^*\boldsymbol{\omega}+\rho_{22}^*\boldsymbol{\Omega})=0 \tag{3.9}$$

respectively, where $e=\nabla\cdot\mathbf{u}=e_x+e_y+e_z$ is the volumetric strain of the solid phase and $\mathbf{u}=(u_x,u_y,u_z)$ is the displacement vector of the solid phase; $\boldsymbol{\omega}=\nabla\times\mathbf{u}$ is the rotational strain within the solid phase. $\epsilon=\nabla\cdot\mathbf{U}$ is the fluid volumetric strain and $\mathbf{U}=(U_x,U_y,U_z)$ is the displacement vector of the fluid phase; $\boldsymbol{\Omega}=\nabla\times\mathbf{U}$ is the rotational strain of the fluid phase. By eliminating ϵ from the two equations within (3.8), we obtain

$$\nabla^4e+A_{\mathrm{I}}\nabla^2e+A_{\mathrm{II}}e=0 \tag{3.10}$$

where $A_{\mathrm{I}}=\omega^2(\rho_{11}^*R-2\rho_{12}^*eQ+\rho_{22}^*P)/(PR-Q^2)$ and $A_{\mathrm{II}}=\omega^4(\rho_{11}^*\rho_{22}^*-(\rho_{12}^*)^2)/(PR-Q^2)$. P equals $A+2N$ with $N=E_s/[2(1+\nu)]$ is the shear modulus of the solid, and $A=\nu E_s/[(1+\nu)(1-2\nu)]$ is the Lame's constant (E_s is the Young's modulus of the solid and ν is the Poisson's ratio). In order to consider the internal frictional losses, the in vacuo Young's modulus of solid E_s is represented by $E_m(1+i\eta)$, where E_m is the static Young's modulus and η is the loss factor [80]. The coefficient Q equals $(1-\phi)E_f$ representing the coupling between the volume change of the solid and that of the fluid, and the coefficient R equals ϕE_f measuring the pressure on the fluid to keep the total volume constant. ϕ is the porosity of the porous medium. E_f is the bulk modulus of elasticity of the fluid in the pores. If the pores are cylindrical, E_f can be expressed as [28, 71]

$$E_f=E_0\left\{1+[2(\gamma-1)/N_{\mathrm{Pr}}^{1/2}\lambda_c\sqrt{-i}]T_c[N_{\mathrm{Pr}}^{1/2}\lambda_c\sqrt{-i}]\right\}^{-1} \tag{3.11}$$

where $E_0 = \rho_f c^2$, $T_c[N_{\mathrm{Pr}}^{1/2}\lambda_c\sqrt{-i}] = J_1[N_{\mathrm{Pr}}^{1/2}\lambda_c\sqrt{-i}]/J_0 T_c[N_{\mathrm{Pr}}^{1/2}\lambda_c\sqrt{-i}]$, γ is the ratio of specific heats, N_{Pr} is the Prandtl number of fluid medium, $\lambda_c^2 = 8\omega\rho_f\alpha_\infty/\phi\sigma$ (α_∞ is the tortuosity and σ is the steady-state, macroscopic flow resistivity), J_0 and J_1 are Bessel functions of first kind of zero and first order, respectively.

The equivalent density $\rho_{11}^* = \rho_{11} + b/i\omega$, $\rho_{12}^* = \rho_{12} - b/i\omega$ and $\rho_{22}^* = \rho_{22} + b/i\omega$; $\rho_{11} = \rho_1 + \rho_a$ is the total effective density of the solid and $\rho_{22} = \rho_2 + \rho_a$ is the total effective density of the fluid where $\rho_{12} = -\rho_a = \rho_2(1 - \alpha_\infty)$ is a coupling coefficient. Further, $\rho_1 = (1 - \phi)\rho_s$ is the apparent solid mass of unit volume of porous material, and $\rho_2 = \phi\rho_f$ is the fluid mass of unit volume of porous material where ρ_s and ρ_f is the densities for the solid and fluid phases, respectively; the coefficient b is a viscous coupling factor defined as

$$b = i\omega\alpha_\infty\rho_2\left(\frac{\rho_c^*}{\rho_f} - 1\right) \tag{3.12}$$

where $\rho_c^* = \rho_f\left\{1 - (2/\lambda_c\sqrt{-i})T_c[\lambda_c\sqrt{-i}]\right\}^{-1}$.

A solution of Eq. (3.10) can be expressed as

$$e = e^{i\omega t - i(k_x x + k_y y)}(C_1 e^{-ik_{\mathrm{I}z}z} + C_2 e^{ik_{\mathrm{I}z}z} + C_3 e^{-ik_{\mathrm{II}z}z} + C_4 e^{ik_{\mathrm{II}z}z}) \tag{3.13}$$

where C_1 through to C_4 are complex amplitudes. Substituting Eq. (3.13) for e into Eq. (3.8) results in the solution for ϵ as

$$\epsilon = e^{i\omega t - i(k_x x + k_y y)}(b_1 C_1 e^{-ik_{\mathrm{I}z}z} + b_1 C_2 e^{ik_{\mathrm{I}z}z} + b_2 C_3 e^{-ik_{\mathrm{II}z}z} + b_2 C_4 e^{ik_{\mathrm{II}z}z}) \tag{3.14}$$

where $k_{\mathrm{I,II}z}^2 = k_{\mathrm{I,II}}^2 - (k_x^2 + k_y^2)$, $k_{\mathrm{I,II}}^2 = (A_{\mathrm{I}} \pm \sqrt{A_{\mathrm{I}}^2 - 4A_{\mathrm{II}}})/2$, $b_1 = a_1 - a_2 k_{\mathrm{I}}^2$, $b_2 = a_1 - a_2 k_{\mathrm{II}}^2$, $a_1 = (\rho_{11}^* R - \rho_{12}^* Q)/(\rho_{22}^* Q - \rho_{12}^* R)$, $a_2 = (PR - Q^2)/[\omega^2(\rho_{22}^* Q - \rho_{12}^* R)]$. The wave related to the complex wave number k_{I} is referred to as the airborne wave, while the wave related to k_{II} is referred to as the frame wave.

Similarly, by eliminating $\mathbf{\Omega}$ from the two equations in Eq. (3.9), we obtain

$$\nabla^2\boldsymbol{\omega} + k_r^2\boldsymbol{\omega} = 0 \tag{3.15}$$

where $k_r^2 = (\omega^2/N)[\rho_{11}^* - (\rho_{12}^*)^2/\rho_{22}^*]$. Note that Eq. (3.15) is a vector equation having three components. $\bar{\omega}$ is the scalar amplitude of the rotational wave. This rotational wave in the porous medium cannot have any component in the z-direction, and, therefore, it can be expressed as

$$\boldsymbol{\omega} = \omega_x \vec{i} + \omega_y \vec{j} + \omega_z \vec{k} = \bar{\omega} \sin\theta \vec{i} - \bar{\omega} \cos\theta \vec{j} + 0\vec{k}. \tag{3.16}$$

A solution of Eq. (3.15) is

$$\bar{\omega} = e^{i\omega t - i(k_x x + k_y y)}(C_5 e^{-ik_{rz}z} + C_6 e^{ik_{rz}z}), \tag{3.17}$$

where $k_{rz}^2 = k_r^2 - (k_x^2 + k_y^2)$. One can obtain the rotational strain of fluid phase similarly from Eq. (3.9) as

$$\Omega = g e^{i\omega t - i(k_x x + k_y y)}(C_5 e^{-ik_{rz}z} + C_6 e^{ik_{rz}z}), \tag{3.18}$$

where $g = -\rho_{11}^*/\rho_{22}^*$. The components of the vector wave $\mathbf{\Omega}$ can be expressed similar to those in Eq. (3.16) as

$$\mathbf{\Omega} = \mathit{\Omega}_x \vec{i} + \mathit{\Omega}_y \vec{j} + \mathit{\Omega}_z \vec{k} = \mathit{\Omega} \sin\theta \vec{i} - \mathit{\Omega} \cos\theta \vec{j} + 0\vec{k}. \tag{3.19}$$

The displacement vector $\mathbf{u}$ in the solid phase and $\mathbf{U}$ in the fluid must contain all the components of displacements in the expressions for the two dilatational waves and the rotational wave. Hence the vector $\mathbf{u}$ can be rewritten as

$$\begin{aligned} \mathbf{u} = u_x \vec{i} + u_y \vec{j} + u_z \vec{k} &= (u_{dx} + u_{rx})\vec{i} + (u_{dy} + u_{ry})\vec{j} + (u_{dz} + u_{rz})\vec{k} \\ &= (u_{dx}\vec{i} + u_{dy}\vec{j} + u_{dz}\vec{k}) + (u_{rx}\vec{i} + u_{ry}\vec{j} + u_{rz}\vec{k}) = \mathbf{u}_d + \mathbf{u}_r \end{aligned} \tag{3.20}$$

where u_{dx}, u_{dy} and u_{dz} represent the displacements caused by dilatational waves, and u_{rx}, u_{ry} and u_{rz} represent the displacements caused by rotational waves. The three directional components of $\mathbf{u}$ can be assumed as the following spatial harmonics

$$\begin{aligned} u_x &= e^{i\omega t - i(k_x x + k_y y)} \Big(D_1 e^{-ik_{\mathrm{I}z}z} + D_2 e^{ik_{\mathrm{I}z}z} + D_3 e^{-ik_{\mathrm{II}z}z} + D_4 e^{ik_{\mathrm{II}z}z} \\ &\quad + D_5 e^{-ik_{rz}z} + D_6 e^{ik_{rz}z} \Big) \qquad (3.21) \\ u_y &= e^{i\omega t - i(k_x x + k_y y)} \Big(D_7 e^{-ik_{\mathrm{I}z}z} + D_8 e^{ik_{\mathrm{I}z}z} + D_9 e^{-ik_{\mathrm{II}z}z} + D_{10} e^{ik_{\mathrm{II}z}z}) \\ &\quad + D_{11} e^{-ik_{rz}z} + D_{12} e^{ik_{rz}z} \Big) \qquad (3.22) \\ u_z &= e^{i\omega t - i(k_x x + k_y y)} \Big(D_{13} e^{-ik_{\mathrm{I}z}z} + D_{14} e^{ik_{\mathrm{I}z}z} + D_{15} e^{-ik_{\mathrm{II}z}z} + D_{16} e^{ik_{\mathrm{II}z}z}) \\ &\quad + D_{17} e^{-ik_{rz}z} + D_{18} e^{ik_{rz}z} \Big) \qquad (3.23) \end{aligned}$$

where D_1 through to D_{18} are complex amplitudes.

The rotational component of the displacement field does not contribute to the divergence. The divergence of a displacement field then equals the volumetric strain. Similarly, the curl of the displacement gives the rotational strain, because the irrotational component does not contribute to the curl. Therefore, the following relations hold for the displacements in the solid

$$\nabla\cdot \mathbf{u} = \nabla\cdot \mathbf{u}_d = e,\ \nabla\cdot \mathbf{u}_r = 0,\ \nabla\times\mathbf{u} = \nabla\times\mathbf{u}_r = \boldsymbol{\omega},\ \nabla\times\mathbf{u}_d = \mathbf{0}. \qquad (3.24)$$

Finally, the displacement components of the solid are given by

$$\begin{aligned} u_x &= ik_x e^{i\omega t - i(k_x x + k_y y)} \Bigg[\bigg(\frac{C_1}{k_{\mathrm{I}}^2} e^{-ik_{\mathrm{I}z}z} + \frac{C_2}{k_{\mathrm{I}}^2} e^{ik_{\mathrm{I}z}z} + \frac{C_3}{k_{\mathrm{II}}^2} e^{-ik_{\mathrm{II}z}z} \\ &\quad + \frac{C_4}{k_{\mathrm{II}}^2} e^{ik_{\mathrm{II}z}z} \bigg) - i\frac{k_{rz}}{k_r^2}\cos\theta (C_5 e^{-ik_{rz}z} - C_6 e^{ik_{rz}z}) \Bigg] \qquad (3.25) \\ u_y &= ik_y e^{i\omega t - i(k_x x + k_y y)} \Bigg[\bigg(\frac{C_1}{k_{\mathrm{I}}^2} e^{-ik_{\mathrm{I}z}z} + \frac{C_2}{k_{\mathrm{I}}^2} e^{ik_{\mathrm{I}z}z} + \frac{C_3}{k_{\mathrm{II}}^2} e^{-ik_{\mathrm{II}z}z} \\ &\quad + \frac{C_4}{k_{\mathrm{II}}^2} e^{ik_{\mathrm{II}z}z} \bigg) - i\frac{k_y k_{rz}}{k_x k_r^2}\cos\theta (C_5 e^{-ik_{rz}z} - C_6 e^{ik_{rz}z}) \Bigg] \qquad (3.26) \\ u_z &= i e^{i\omega t - i(k_x x + k_y y)} \Bigg[\bigg(\frac{k_{\mathrm{I}z}}{k_{\mathrm{I}}^2} C_1 e^{-ik_{\mathrm{I}z}z} - \frac{k_{\mathrm{I}z}}{k_{\mathrm{I}}^2} C_2 e^{ik_{\mathrm{I}z}z} + \frac{k_{\mathrm{II}z}}{k_{\mathrm{II}}^2} C_3 e^{-ik_{\mathrm{II}z}z} \\ &\quad - \frac{k_{\mathrm{II}z}}{k_{\mathrm{II}}^2} C_4 e^{ik_{\mathrm{II}z}z} \bigg) + i\frac{k_x^2 + k_y^2}{k_x k_r^2}\cos\theta (C_5 e^{-ik_{rz}z} + C_6 e^{ik_{rz}z}) \Bigg] \qquad (3.27) \end{aligned}$$

where all the complex amplitudes D_1 through to D_{18} are expressed by the wave number, incident angle θ and coefficients C_1 through to C_6.

Similarly, for the fluid phase,

$$\nabla\cdot \mathbf{U} = \nabla\cdot \mathbf{U}_d = \epsilon,\ \nabla\cdot \mathbf{U}_r = 0,\ \nabla\times \mathbf{U} = \nabla\times \mathbf{U}_r = \mathbf{\Omega},\ \nabla\times \mathbf{U}_d = 0 \tag{3.28}$$

and, therefore, the fluid displacement components can be expressed as

$$\begin{aligned} U_x &= ik_x e^{i\omega t - i(k_x x + k_y y)}\left[\left(b_1\frac{C_1}{k_{\mathrm{I}}^2}e^{-ik_{\mathrm{I}z}z} + b_1\frac{C_2}{k_{\mathrm{I}}^2}e^{ik_{\mathrm{I}z}z} + b_2\frac{C_3}{k_{\mathrm{II}}^2}e^{-ik_{\mathrm{II}z}z}\right.\right. \\ &\quad \left.\left. +b_2\frac{C_4}{k_{\mathrm{II}}^2}e^{ik_{\mathrm{II}z}z}\right) - ig\frac{k_{rz}}{k_r^2}\cos\theta(C_5e^{-ik_{rz}z} - C_6e^{ik_{rz}z})\right] \end{aligned} \tag{3.29}$$

$$\begin{aligned} U_y &= ik_y e^{i\omega t - i(k_x x + k_y y)}\left[\left(b_1\frac{C_1}{k_{\mathrm{I}}^2}e^{-ik_{\mathrm{I}z}z} + b_1\frac{C_2}{k_{\mathrm{I}}^2}e^{ik_{\mathrm{I}z}z} + b_2\frac{C_3}{k_{\mathrm{II}}^2}e^{-ik_{\mathrm{II}z}z}\right.\right. \\ &\quad \left.\left. +b_2\frac{C_4}{k_{\mathrm{II}}^2}e^{ik_{\mathrm{II}z}z}\right) - ig\frac{k_y k_{rz}}{k_x k_r^2}\cos\theta(C_5e^{-ik_{rz}z} - C_6e^{ik_{rz}z})\right] \end{aligned} \tag{3.30}$$

$$\begin{aligned} U_z &= ie^{i\omega t - i(k_x x + k_y y)}\left[\left(b_1\frac{k_{\mathrm{I}z}}{k_{\mathrm{I}}^2}C_1e^{-ik_{\mathrm{I}z}z} - b_1\frac{k_{\mathrm{I}z}}{k_{\mathrm{I}}^2}C_2e^{ik_{\mathrm{I}z}z} + b_2\frac{k_{\mathrm{II}z}}{k_{\mathrm{II}}^2}C_3e^{-ik_{\mathrm{II}z}z}\right.\right. \\ &\quad \left.\left. -b_2\frac{k_{\mathrm{II}z}}{k_{\mathrm{II}}^2}C_4e^{ik_{\mathrm{II}z}z}\right) + ig\frac{k_x^2 + k_y^2}{k_x k_r^2}\cos\theta(C_5e^{-ik_{rz}z} + C_6e^{ik_{rz}z})\right]. \end{aligned} \tag{3.31}$$

The relevant stresses σ_{ij} in the solid and the fluid pressure σ_f are given by [29]

$$\begin{aligned} \sigma_{ij} &= 2Ne_{ij} + (Ae + Q\epsilon)\delta_{ij} \qquad (i,j = 1,2,3) \\ \sigma_f &= Qe + R\epsilon \end{aligned} \tag{3.32}$$

where δ_{ij} is the Kronecker delta. The stress components σ_z, τ_{xy}, τ_{xz} and τ_{yz} in solid phase and the fluid pressure σ_f can be obtained by using Eqs. (3.25)-(3.27) and Eqs. (3.29)-(3.31) and the relationship of the displacements and the strains as

$$\begin{aligned}\sigma_z &= e^{i\omega t-i(k_x x+k_y y)}\left[\left(2N\frac{k_{\mathrm{I}z}^2}{k_{\mathrm{I}}^2}+A+b_1Q\right)C_1e^{-ik_{\mathrm{I}z}z}\right.\\&\quad+\left(2N\frac{k_{\mathrm{I}z}^2}{k_{\mathrm{I}}^2}+A+b_1Q\right)C_2e^{ik_{\mathrm{I}z}z}+\left(2N\frac{k_{\mathrm{II}z}^2}{k_{\mathrm{II}}^2}+A+b_2Q\right)C_3e^{-ik_{\mathrm{II}z}z}\\&\quad+\left(2N\frac{k_{\mathrm{II}z}^2}{k_{\mathrm{II}}^2}+A+b_2Q\right)C_4e^{ik_{\mathrm{II}z}z}\\&\quad\left.+2N\frac{(k_x^2+k_y^2)k_{rz}}{k_xk_r^2}\cos\theta(C_5e^{-ik_{rz}z}-C_6e^{ik_{rz}z})\right]\end{aligned}\tag{3.33}$$

$$\begin{aligned}\tau_{xy} &= Ne^{i\omega t-i(k_x x+k_y y)}\left[2k_xk_y\left(\frac{C_1}{k_{\mathrm{I}}^2}e^{-ik_{\mathrm{I}z}z}+\frac{C_2}{k_{\mathrm{I}}^2}e^{ik_{\mathrm{I}z}z}+\frac{C_3}{k_{\mathrm{II}}^2}e^{-ik_{\mathrm{II}z}z}\right.\right.\\&\quad\left.\left.+\frac{C_4}{k_{\mathrm{II}}^2}e^{ik_{\mathrm{II}z}z}\right)-\frac{k_yk_{rz}}{k_r^2}\cos\theta(C_5e^{-ik_{rz}z}-C_6e^{ik_{rz}z})\right]\end{aligned}\tag{3.34}$$

$$\begin{aligned}\tau_{xz} &= Ne^{i\omega t-i(k_x x+k_y y)}\left[\frac{2k_xk_{\mathrm{I}z}}{k_{\mathrm{I}}^2}(C_1e^{-ik_{\mathrm{I}z}z}-C_2e^{ik_{\mathrm{I}z}z})\right.\\&\quad+\frac{2k_xk_{\mathrm{II}z}}{k_{\mathrm{II}}^2}(C_3e^{-ik_{\mathrm{II}z}z}-C_4e^{ik_{\mathrm{II}z}z})\\&\quad\left.+\frac{k_x^2+k_y^2-k_{rz}^2}{k_r^2}\cos\theta(C_5e^{-ik_{rz}z}+C_6e^{ik_{rz}z})\right]\end{aligned}\tag{3.35}$$

$$\begin{aligned}\tau_{yz} &= Ne^{i\omega t-i(k_x x+k_y y)}\left[\frac{2k_yk_{\mathrm{I}z}}{k_{\mathrm{I}}^2}(C_1e^{-ik_{\mathrm{I}z}z}-C_2e^{ik_{\mathrm{I}z}z})\right.\\&\quad+\frac{2k_yk_{\mathrm{II}z}}{k_{\mathrm{II}}^2}(C_3e^{-ik_{\mathrm{II}z}z}-C_4e^{ik_{\mathrm{II}z}z})\\&\quad\left.+\frac{k_y(k_x^2+k_y^2-k_{rz}^2)}{k_xk_r^2}\cos\theta(C_5e^{-ik_{rz}z}+C_6e^{ik_{rz}z})\right]\end{aligned}\tag{3.36}$$

$$\begin{aligned}\sigma_f &= e^{i\omega t-i(k_x x+k_y y)}[(Q+b_1R)C_1e^{-ik_{\mathrm{I}z}z}+(Q+b_1R)C_2e^{ik_{\mathrm{I}z}z}\\&\quad+(Q+b_2R)C_3e^{-ik_{\mathrm{II}z}z}+(Q+b_2R)C_4e^{ik_{\mathrm{II}z}z}].\end{aligned}\tag{3.37}$$

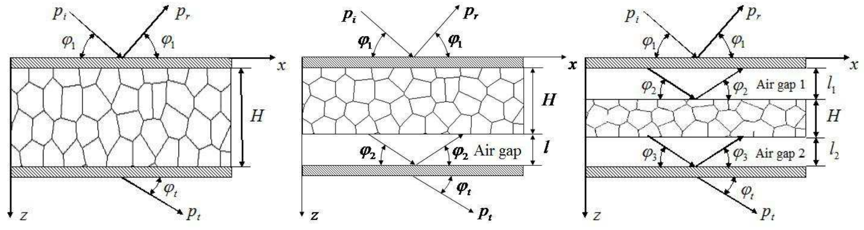

(a) BB (b) BU (c) UU

Figure 3.2: Through the thickness view of the sound wave transmission for different skin-plate configurations.

Here σ_z is the normal stress of the porous material's solid phase along the z-axis, τ_{xy}, τ_{xz} and τ_{yz} are the shear stresses acting on the solid phase. σ_f is the pressure acting on the fluid element.

3.3 Three configurations and the associated boundary conditions

Three configurations of the skin-plates, the porous material and the air gap (when applicable) are to be considered as shown schematically in Figure 3.2. We consider them because they have been frequently studied by other researchers in the past [28, 51, 81–83]. They are described, in turn, next. A bonded-bonded (BB) configuration, as shown in Figure 3.2a, is the one having both sides of porous material bonded directly to the two elastic panels. A bonded-unbonded (BU) configuration has one side of porous material bonded directly to an elastic panel and the second side is separated from the second elastic plate by an air gap (see Figure 3.2b). An unbonded-unbonded (UU) configuration has both sides of porous material unbonded to the two elastic plates (Figure 3.2c). We will present a comparative study of the vibro-acoustic performance of the three configurations in the present work.

At the free surface of a porous layer (that is exposed to a stationary medium and not bonded directly to a plate as in BU and UU configurations), the five boundary conditions that should be satisfied are

(i). $-\phi p = \sigma_f$

(ii). $-(1-\phi)p = \sigma_z$

(iii). $(1-\phi)\frac{D^2 u_z}{Dt^2} + \phi\frac{D^2 U_z}{Dt^2} = -\frac{1}{\rho}\frac{\partial p}{\partial z}$

(iv). $\tau_{xz} = 0$

(v). $\tau_{yz} = 0$

where p is the pressure in the exterior acoustic field at the interface and ρ is the density of the exterior fluid. The first two conditions represent the relationship of the acoustical pressure acting on the fluid phase and the solid phase, respectively. The third condition represents the relation of the normal displacement in the porous material and the acoustical pressure. The last two conditions assert that there is no shear force acting on the interface due to the assumption of an inviscid exterior fluid.

When the porous material is bonded directly to an elastic panel, the following seven boundary conditions must be satisfied

(i). $\frac{D^2 w}{Dt^2} = -\frac{1}{\rho}\frac{\partial p}{\partial z}$

(ii). $u_z = w$

(iii). $U_z = w$

(iv). $u_x = u_s(-/+)\frac{h}{2}\frac{\partial w}{\partial x}$

(v). $u_y = v_s(-/+)\frac{h}{2}\frac{\partial w}{\partial y}$

(vi). $(+/-)\tau_{xz} = \left[D_s\left(k_x^2 + \frac{1-\nu}{2}k_y^2\right) - \omega^2 m_s\right]u_s + D_s\frac{1+\nu}{2}k_x k_y v_s$

(vii). $(+/-)p + (-/+)q_p - i\left(k_x\frac{h}{2}\tau_{xz} + k_y\frac{h}{2}\tau_{yz}\right) = [D(k_x^2 + k_y^2)^2 - \omega^2 m_s]w$

where the panel transverse displacement w equals $We^{i\omega t - i(k_x x + k_y y)}$ and the mid-plane and the in-plane panel displacements are u_s and v_s along the x-axis and the y-axis, respectively. D is the bending stiffness per unit width, D_s is the membrane stiffness per unit width. m_s is the panel mass per unit area of the panels and $q_p = -\sigma - \sigma_f$ is the normal force per unit area of the panel due to the interaction of the panel with the elastic porous material. The first condition represents the relationship of the transverse displacement of the plate and the acoustic pressure. The second and third conditions give the requirement of continuity of displacements normal to the plate. Conditions (iv) and (v) state that the tangential displacements of solid phase of porous material are equal to the in-plane surface displacements of the plate. The sixth condition represents the in-plane vibration of plate under the excitation of a shear force. The last condition is the Euler-Bernoulli transverse panel equation including the moment provided by the shear forces acting in the plane of the panel. In boundary conditions (iv) to (vii), the first signs are applicable when the porous material is attached to the positive z-facing surface of the panel, and the second signs when the porous material is attached to the negative z-facing surface.

When the porous material is not attached to the panel, the following boundary conditions should be satisfied at the mid-surface of the plates:

(i). $\frac{D^2 w}{Dt^2} = -\frac{1}{\rho_1}\frac{\partial p_1}{\partial z}$

(ii). $\frac{D^2 w}{Dt^2} = -\frac{1}{\rho_2}\frac{\partial p_2}{\partial z}$

(iii). $[D(k_x^2 + k_y^2)^2 - \omega^2 m_s]w = p_1 - p_2$

where p_1 and p_2 are the acoustic pressure in the air spaces on the two sides of the panel, and ρ_1 and ρ_2 are the respective density of the fluids in one side and the other side. Taking account of the three different configurations in Figure 3.2, the transmission problem is formulated for each one of them, in turn, next.

(I) BB configuration: The panel in this configuration can be divided into three regions: the incident region, the porous material region and the transmitted region (see Figure 3.2a). The incident region and the porous material region are separated by an isotropic thin elastic plate. The same is true at the interface between the porous material region and the transmitted region. The thickness of porous material is H. The boundary conditions relevant to this configuration can be expressed in a matrix form and are presented in Appendix A.

(II) BU Configuration: Figure 3.2b shows a double panel lined with porous material in the BU configuration. It consists of an incident region, a porous material region, an air gap and a transmitted region. The fluid medium in the air gap region has physical properties (ρ_2, c_2). The thickness of this gap is l as shown. The wave in air gap region makes angles φ_2 and θ relative to the x-y plane and the x-axis, respectively.

The wave pressure in air gap region is expressed as

$$p_2 = p_{2i} + p_{2r} = P_{2i} e^{i\omega t - i(k_{2x}x + k_{2y}y + k_{2z}z)} + P_{2r} e^{i\omega t - i(k_{2x}x + k_{2y}y - k_{2z}z)} \tag{3.38}$$

where

$$k_{2x} = k_2 \cos\varphi_2 \cos\theta,\ k_{2y} = k_2 \cos\varphi_2 \sin\theta,\ k_{2z} = \sqrt{k_2^2 - (k_{2x}^2 + k_{2y}^2)}. \tag{3.39}$$

Since, there is no flow in the air gap region, p_2 propagates according to the classical wave equation and

$$k_2 = \omega / c_2. \tag{3.40}$$

The boundary conditions for this configuration can again be expressed in a matrix form and are presented in Appendix B.

(III) UU Configuration: UU configuration has two air gaps with the thickness l_1 and l_2, respectively (see Figure 3.2c). The angles are φ_2 and θ in air gap 1 and φ_3 and θ in air gap 2 respectively. The fluid in the two air regions have physical properties (ρ_2, c_2) and (ρ_3, c_3), respectively.

The wave pressures in two air gaps can be written as a harmonic function in space and time

$$p_2 = p_{2i} + p_{2r} = P_{2i} e^{i\omega t - i(k_{2x}x + k_{2y}y + k_{2z}z)} + P_{2r} e^{i\omega t - i(k_{2x}x + k_{2y}y - k_{2z}z)} \tag{3.41}$$

$$p_3 = p_{3i} + p_{3r} = P_{3i} e^{i\omega t - i(k_{3x}x + k_{3y}y + k_{3z}z)} + P_{3r} e^{i\omega t - i(k_{3x}x + k_{3y}y - k_{3z}z)} \tag{3.42}$$

where

$$k_{2x} = k_2 \cos\varphi_2 \cos\theta,\ k_{2y} = k_2 \cos\varphi_2 \sin\theta,\ k_{2z} = \sqrt{k_2^2 - (k_{2x}^2 + k_{2y}^2)} \tag{3.43}$$

$$k_{3x} = k_3 \cos\varphi_3 \cos\theta,\ k_{3y} = k_3 \cos\varphi_3 \sin\theta,\ k_{3z} = \sqrt{k_3^2 - (k_{3x}^2 + k_{3y}^2)}. \tag{3.44}$$

Since, there is no flow in two air gaps, p_2 and p_3 propagate according to the classical wave equation and

$$k_2 = \omega / c_2,\ k_3 = \omega / c_3. \tag{3.45}$$

The boundary conditions as expressed in the matrix form are presented in Appendix C.

3.4 Random incidence transmission loss (TL)

The trace wavelengths must match at the boundary (see the three Appendices) and, therefore,

$$\cos\varphi_t = \frac{c_t}{c_i}\frac{\cos\varphi_1}{(1 + M\cos\theta\cos\varphi_1)}. \tag{3.46}$$

In the following, we consider two possible cases for the sign of $M\cos\theta$.

Case (1) In the equation above when $M\cos\theta > 0$, there exists a critical incident angle φ_{1c} for $\varphi_{tmax} = 180°$. The φ_{1c} can be obtained from Eq. (3.46),

$$\cos\varphi_{1c} = -\frac{1}{(c_t/c_i) + M\cos\theta} \tag{3.47}$$

It is obvious that $\varphi_{1c} > 90°$ because of the negative sign. For $\varphi_1 > \varphi_{1c}$, total reflection occurs at the boundary. In that case, the wave number component k_{tz} in the transmitted side becomes purely imaginary leading to evanescent waves. Therefore, no sound energy is transmitted into the interior for $\varphi_1 > \varphi_{1c}$.

Case(2) Similarly, when $M\cos\theta < 0$, the value of φ_{1c} can be obtained from Eq. (3.46) for $\varphi_t = 0°$,

$$\cos\varphi_{1c} = \frac{1}{(c_t/c_i) - M\cos\theta} \tag{3.48}$$

For $\varphi_1 < \varphi_{1c}$, the wave number component k_{tz} becomes purely imaginary and no sound energy is transmitted. We need to consider these two cases in our calculations for the average power transmission.

The power transmission coefficient τ is defined as

$$\tau = \frac{I_{\text{transmitted}}}{I_{\text{incident}}} = \frac{\rho_i c_i}{\rho_t c_t}\left|\frac{P_t}{P_i}\right|^2 \tag{3.49}$$

The average of the power transmission coefficient $<\tau>$ can be expressed as [32]

$$<\tau>=\frac{\int_{\theta=0}^{2\pi}\int_{\varphi_1=\varphi_m}^{\frac{\pi}{2}}\tau\sin\varphi_1\cos\varphi_1 d\varphi_1 d\theta}{\int_{\theta=0}^{2\pi}\int_{\varphi_1=\varphi_m}^{\frac{\pi}{2}}\sin\varphi_1\cos\varphi_1 d\varphi_1 d\theta} \tag{3.50}$$

where φ_m is the limiting angle below which it is assumed that no sound is received. In practice, the length of the panel is not infinite. Therefore, correct calculation of the average power transmission coefficient requires careful consideration to this limiting angle of incidence beyond which total reflection takes place. This choice is guided by our motivation to compare results with those of Bolton's [28] who studied a special case theoretically and experimentally when $M = 0$. They were forced to adopt this limiting value for calculations because of the limitations posed by experimental set up. Hence, when $M\cos\theta > 0$, φ_m is taken as 18° (the same limiting value as in Bolton et al. [28] for comparison); when $M\cos\theta < 0$, $\varphi_m = \varphi_{1c}$.

To calculate the power transmission coefficient, the integration of Eq. (3.50) is carried out numerically by the Simpson's rule in the range of φ_1 admissible by the restriction imposed by total reflection. The random incidence transmission loss is defined as

$$\mathrm{TL} = -10\log_{10} <\tau>. \tag{3.51}$$

Before discussing the numerical results, some basic idea of the sound transmission loss should be introduced first. Unlike fluids, solid materials can resist compressive stresses as well as shear stresses. Therefore, both longitudinal waves (also known as compression wave) and shear waves can propagate in solids. For longitudinal waves, the oscillations of the particles occur in the direction of the wave propagation as shown in Figure 3.3a. The contraction and expansion in the transverse directions of the plate is a result of the Poisson effect. The sound speed of longitudinal wave in such a medium is given by

$$c_L = \sqrt{\frac{E_p}{\rho_p(1-\nu_p^2)}}. \tag{3.52}$$

By contrast, for the shear waves, the particle displacement is perpendicular (or transverse) to the direction of wave propagation (see Figure 3.3b). Therefore, the shear wave

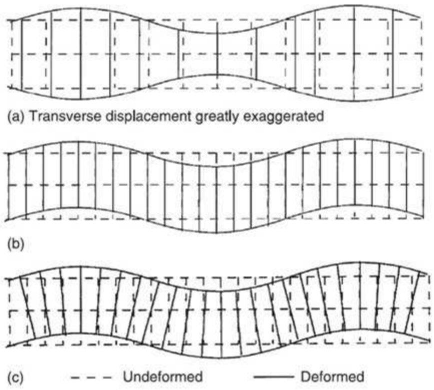

Figure 3.3: Deformation patterns of various types of wave in straight bars and flat plates [84]: (a) Longitudinal wave; (b) shear wave; (c) bending wave.

is also referred to a transverse wave in the literature. The speed of shear waves in the plate is given by

$$c_S = \sqrt{\frac{G_p}{\rho_p}} \tag{3.53}$$

where G_p is the shear modulus given by $G_p = E_p/2(1 + \nu_p)$, where E_p is the Young's modulus and ν_p is the Poisson's ratio. Generally, since G_p is smaller than E_p, the speed of the shear wave is lower than that of the longitudinal wave.

As shown in Figure 3.3c, the bending wave, or the flexural wave, propagates along the plate axis. This type of wave motion is accompanied by the rotation of the cross-section about the neutral axis for beams and the rotation of the line normal to the mid-plane about an axis perpendicular to the propagation direction for plates. Sound radiation in vibrating plates is caused principally by bending waves. This is because the transverse deformation caused by bending waves can effectively disturb an adjacent fluid [84]. The speed of bending wave in a thin plate is

$$c_B = \sqrt[4]{\frac{D\omega^2}{m}} \tag{3.54}$$

where D is the bending stiffness and m is the mass per unit area of the plate. Unlike the speed of longitude wave or shear wave, the speed of bending wave is not only a function of the properties of the plate, but also of the frequency of oscillation. Eq. (3.54) indicates that the speed will increase with increasing the wave frequency. Therefore, a bending wave is dispersive. A critical frequency exists when the speed of bending wave propagation is equal to the speed of acoustic wave propagation in the surrounding medium. The value of the critical frequency can be obtained from Eq. (3.54) as

$$f_c = \frac{c^2}{2\pi}\sqrt{\frac{m}{D}} \tag{3.55}$$

where c presents the speed of sound in air. If a plane wave is incident on a plate at an angle of ϕ measured from the normal of the plate, then the coincidence frequency, at which the bending wave length equals the trace wave length of the incident wave, is given by [84]

$$f_{co} = \frac{f_c}{\sin^2\phi}. \tag{3.56}$$

It is obvious that the critical frequency is lowest coincidence frequency with the angle of incidence at 90°.

As shown in Figure 3.4, the transmission loss of a bounded homogeneous, single panel can be schematically divided into four general regions of interest: stiffness controlled, resonance controlled, mass controlled, and coincidence controlled [85].

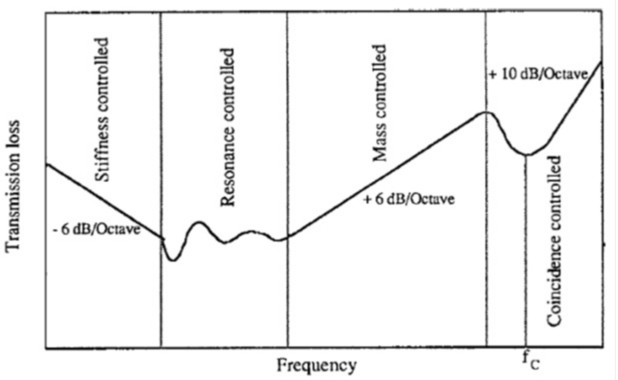

Figure 3.4: Characteristic transmission loss of a bounded, homogeneous, single panel [85].

The transmission loss characteristics are controlled by the stiffness of the panel at frequencies below the first fundamental natural frequency. In this region, the slope of the transmission loss is -6 dB/Octave with the increase in frequency. Due to the finite size of the panel, the structure has several natural frequencies. Therefore, the second region is controlled by the resonant structural modes. At frequencies between the first few natural frequencies and the *critical frequency*, the transmission loss is mass controlled. In this region, the transmission loss, increases with a slope of 6 dB/Octave, and is approximately linear dependent on the mass of the panel. Ultimately, due to the *coincidence*, there is a dip in the transmission loss when the frequency approaches the critical frequency. At frequencies above the critical frequency, the transmission loss again increases. The rise in this region is of the order of 10 dB/Octave. All the resonant responses are damping controlled.

3.5 Multiobjective optimization problem

In an industrial design, besides the acoustic performance, other design considerations, such as weight, structural stiffness and strength, operation constrains, etc., of the sandwich structure are still important. In general, a multiobjective optimization problem (MOP) has two or more objectives involving many decision variables and constraints. It can be mathematically expressed as

$$\min\{f_1(\mathbf{x}), f_2(\mathbf{x}), ..., f_k(\mathbf{x})\} \tag{3.57}$$

$$\text{subject to :} g(\mathbf{x}) \leq 0 \tag{3.58}$$

$$\mathbf{x}_L \leq \mathbf{x} \leq \mathbf{x}_U \tag{3.59}$$

where $\{f_1, f_2, ..., f_k\}$ is a set of k objective functions. The inequality constraints, $g(\mathbf{x})$ are due to the considerations for the problem. Here, $\mathbf{x}$ is the decision variables vector. $\mathbf{x}_L$ and $\mathbf{x}_U$ are the lower and upper bounds of $\mathbf{x}$, respectively. The solutions of an MOP are presented in terms of the Pareto optimal fronts. Pareto optimal solutions are not unique. There exists a set of solutions known as the Pareto optimal set if there is no other solution that can improve at least one of the objectives without degrading any other objective. The vectors $\mathbf{x}^*$ corresponding to the solutions included in the Pareto optimal set are called nondominated. The plot of the objective functions whose nondominated vectors are in the Pareto optimal set is called the Pareto front.

In practice, considering the severe weight and space constraints imposed on airplane soundproofing treatments, emphasis in many cases has been on minimizing the weight and depth of the treatment while maintaining adequate sound attenuation characteristics [3]. We now present results when the overall separation between the skins is fixed. In other word, it becomes a bi-optimization problem: one of maximising acoustic transmission loss while minimising weight. TL is a strong function of frequency. Since we have optimized the same function as Makris et al. [86] which is also in an acoustic context, the weighted average transmission coefficient $\bar{\tau}_{\text{avg}}$ over a range of frequency is defined as

$$\bar{\tau}_{\text{avg}} = \sum_{n=1}^{7} w_n \bar{\tau}_n \tag{3.60}$$

where w_n represents a normalized weighting assigned to seven different points of frequency. These weights have been tabulated later in Table 3.4 while discussing a numerical simulation. Further, the transmission loss can be redefined on the basis of such a band-averaged transmission coefficient as

$$\text{TL} = -10 \log_{10} \left| \bar{\tau}_{\text{avg}} \right| . \tag{3.61}$$

3.6 Results and discussion

In order to be able to compare and validate results for special cases (e.g. one without external flow), the parameters used in the numerical calculations are taken from that given by Bolton et al. [28] who considered a problem without exterior flow. Here we include the effect of exterior flow on sound transmission. The parameters used in the numerical calculations are listed in Table 3.1. h_1 and h_2 represent the thickness of aluminum sheet on the incident side and the transmitted side, respectively. The depth of air gap of the BU configuration is denoted by l (see Figure 3.2b). For the UU configuration, the depths of the two air gaps are l_1 and l_2, respectively (see Figure 3.2c).

When setting $M = 0$ and $\theta = 0$, the results are consistent with Bolton's results [28] as shown in Figure 3.5 for the three different configurations of the sandwich. Note that Bolton et al.'s study is considerably simple as the equations become two-dimensional

Table 3.1: Parameters of the physical system.

	Description	Value
Plate properties		
E_p	Young's modulus	70 GPa
ρ_p	Density	2700 kg/m^3
ν_p	Poisson's ratio	0.33
h_1	Thickness	1.27 mm
h_2	Thickness	0.762 mm
Porous material properties		
E_m	Bulk Young's modulus	8×10^5 Pa
ρ_1	Bulk density of solid phase	30 kg/m^3
ν	Bulk Poisson's ratio	0.4
η	Loss factor	0.265
σ	Flow resistivity	25000 MKS Rayls/m
α_∞	Tortuosity	7.8
ϕ	Porosity	0.9
H	Thickness	27 mm
Air gap geometry		
l	Thickness	14 mm
l_1	Thickness	2 mm
l_2	Thickness	6 mm

in the absence of mean flow. The agreement of our 3-D results for the special case of $M = 0$ provides a validation for the correctness of our results. The reason for the slight difference is that Bolton's results shown here has been captured from images of their figures and the accuracy of the data is therefore based on the finite resolution of the figures used.

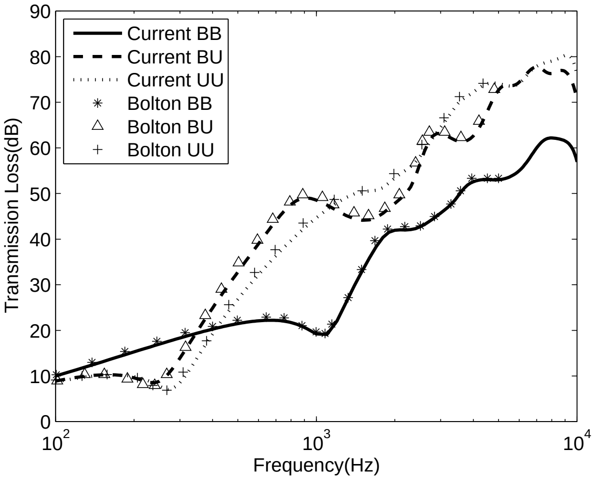

Figure 3.5: Transmission loss of current results ($M = 0$ and $\theta = 0$) vs. Bolton's results [28].

3.6.1 The effect of the external mean flow

The dependence of transmission loss with frequency for the BB configuration under a diffuse sound field excitation in the presence of external mean flow is shown in Figure 3.6. While the flow is considered on one side of the panel, the air properties on both sides are taken as those corresponding to the ground conditions. This deliberate simplification is to bring out the convective effect that the flow has on sound transmission. The variation of transmission loss with frequency is not seen to be monotonic. All these curves have two main dips at the fundamental resonance frequency f_f (lower) and the critical frequency (upper) f_c, respectively. The fundamental resonance frequency f_f, also known as mass-spring-mass resonance frequency, is a low frequency resonance which is due to the panels behaving like two masses coupled by an air-spring. It is a function of the panel masses and the air gap [85]. The critical frequency f_c, as mentioned previously in section 3.4, is the frequency at which the speed of bending wave in the plate equals the speed of acoustic wave in the surrounding medium.

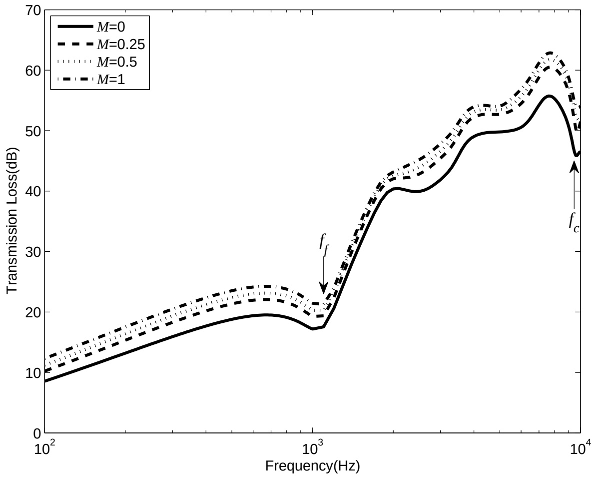

Figure 3.6: The variation of the transmission loss with frequency for different Mach numbers (BB configuration). The f_f and f_c are labelled here.

Trends similar to those presented above for the BB configuration are also found to be present in the case of the other two configurations. Transmission loss characteristics for the BU configuration and the UU configuration are presented in Figure 3.7 and Figure 3.8, respectively. Again, the values of the transmission loss are greater at all frequencies for both configurations with increasing flow velocity on one side of the panel. This highlights superior acoustic performance of these panels in the presence of convective

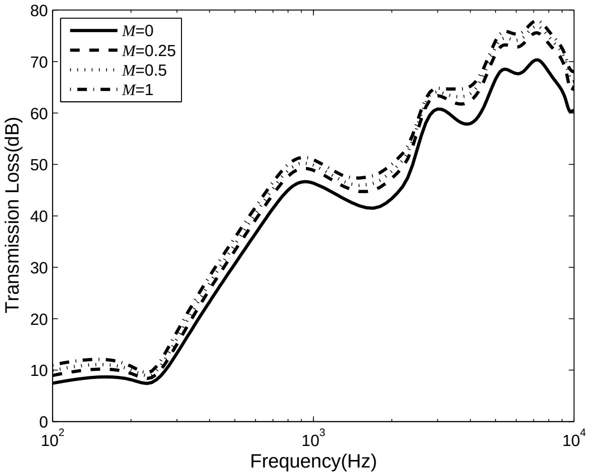

Figure 3.7: The variation of the transmission loss with frequency for different Mach numbers (BU configuration).

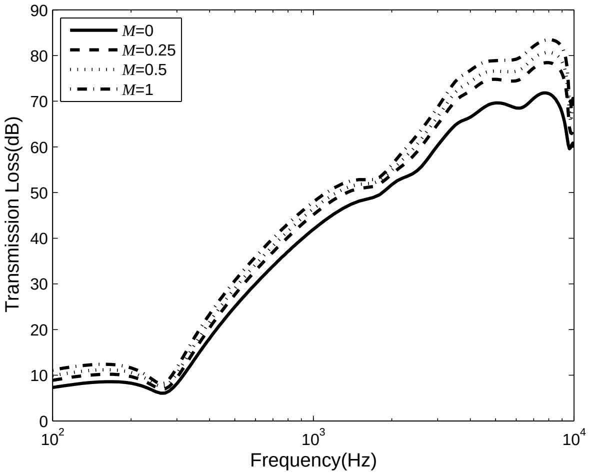

Figure 3.8: The variation of the transmission loss with frequency for different Mach numbers (UU configuration).

flow. In other words, a calculation based on static air on the incidence side provides a conservative estimate of sound insulation of such sandwich panels.

It is seen here that the transmission loss increases with the increase in Mach number for all the three configurations studied. This is pronounced for frequencies above 2 kHz in all configurations. This effect is significant in higher frequency range in the UU configuration. The increase of TL due to the increase of Mach number can be explained on the basis that the impedance of the panel will increase because of a Mach number dependent refraction [31, 32, 87]. Similar to the results of Bolton et al. [28], the BU configuration yields a transmission loss 2-6 dB higher than that of the UU configuration for frequencies below 1 kHz, but its high frequency performance is not quite as good as that of the UU configuration under the flight conditions. However, we note that this result is based on the fact that the distances between the two plates in the three configurations are different. This is due to the fact that the parameters used in this calculation are the same as that of Bolton's [28] (see Table 3.1) therefore allowing a direct comparison of the data.

If no porous material is present, the construction becomes one of the classic double wall problem. The fundamental resonance frequency and the critical frequency for this special case can be expressed as [25, 84, 88]

$$f_f = \frac{1}{2\pi \sin\varphi}\sqrt{\frac{\rho c^2}{dm'}} \tag{3.62}$$

$$f_c = \frac{c^2}{2\pi \cos^2\varphi}\sqrt{\frac{m_s}{D}} \tag{3.63}$$

where ρ, c and φ are air density, air sound speed and pressure incident angle in the gap; d is the depth of the air gap; $m' = m_1 m_2/(m_1 + m_2)$ (m_1 and m_2 are the mass per unit area of the two plates, respectively). The random incidence is taken into account, so f_f and f_c will vary with the incident angles. Their minimum values are

$$f_f = \frac{1}{2\pi}\sqrt{\frac{\rho c^2}{dm'}} \tag{3.64}$$

$$f_c = \frac{c^2}{2\pi}\sqrt{\frac{m_s}{D}}. \tag{3.65}$$

Table 3.2 shows the minimum values (with respect to the direction of incidence) of the fundamental resonance frequency and the critical frequency of different configurations without porous material. As shown in Figure 3.6 to Figure 3.8, the critical frequency of each configuration is the same and even similar to the case when no porous material is present. Therefore, porous material has no significant effect on the critical frequency. The critical frequency only depends on the properties of the plates. However, the fundamental resonance frequency is directly related to other geometric and material parameters according to Eq. (3.62). Due to the stiffening effect of the directly attached foam lining in the BB configuration, the fundamental resonance frequency is higher than that without the porous material. For the other two configurations, this remains unchanged. Cavity resonances occur that may reduce the transmission loss, when the dimension of the air gap matches the wavelength of sound waves in air. This effect can be reduced by filling the air gap between the plates with porous material. In a diffuse sound field, the dips caused by the cavity resonances will vanish due to the averaging effect that takes place over a hemisphere. Below the cavity resonance frequency, the curves are seen to follow an approximate mass law behaviour.

Table 3.2: The minimum value of f_f and f_c of different configurations.

Configurations	f_f(Hz)	f_c(Hz)
BB	322	9469
BU	262	9469
UU	283	9469

3.6.2 The effect of the pressure within the air gap

The effect of the pressure in the air gap (the region between the two face plates) is studied next. In the cruising condition, the properties of air at various altitudes have been taken from Tang et al. [42] for simulations and are shown in Table 3.3. The condition on the incidence side and the transmission side are kept corresponding to an altitude of 35000 ft and 10000 ft, respectively. The frequency dependence of transmission loss corresponding to the three configurations, i.e. BB, BU and UU conditions, with the air gap pressure at $M = 0.5$ is shown in Figure 3.9 to Figure 3.11, respectively. This effect is significant for the BU and the UU configurations (Figures 3.10 and 3.11 respectively), but almost absent for the BB configuration (Figure 3.9). The increase in the TL is seen to be about 15-20 dB when the pressure in the air gap is reduced to a level corresponding to an altitude of 35000 ft in the BU configuration and about 8-16 dB in the UU configuration. The impedance mismatch between the incidence region and the air gap due to different air properties for the BU and UU configurations alters the transmission loss very significantly. This agrees with the observation of Tang et al. [43] who studied the vibroacoustics of a similar system in the absence of porous lining. Liu et al. [39] demonstrated that the mismatch of acoustics properties between the panels increases the transmission loss. According to Eq. (3.54), bending waves of different frequencies travel at different speeds. This means that for every frequency above the critical frequency, there will be an angle of incidence at which the speed of the bending wave is equal to the speed of the incidence sound wave. If we research transmission loss for the frequencies higher than 10000 Hz, the resonant responses will appear in all three configurations BB, BU and UU. At the frequencies above the critical frequency, all the resonant responses are damping controlled. Since the porous material provides less damping in the UU configuration than that in other two configurations, the resonant responses can only be seen near the critical frequency in the UU configuration as shown in Figure 3.11. In addition, the fundamental resonance frequency for the BU and the UU configurations becomes lower, but the critical frequency is still the same. The fundamental resonance is caused by the mass-air-mass resonance (see Eq. (3.64)). Thus the property of air has a key role. However, the critical frequency is only affected by the properties of the panel (see Eq. (3.65)). Therefore, the BU and UU configuration offers a better performance of sound insulation than the BB configuration does above 300 Hz by comparing the Figures 3.9 to 3.11. Due to practical considerations, the BU configuration may be easier to implement in practice than the UU configuration.

Table 3.3: The properties of fluid at different altitudes.

Altitude ft	Density of air kg/m^3	Speed of sound m/s
10,000	0.9041	328.558
25,000	0.5489	309.966
35,000	0.3795	296.556

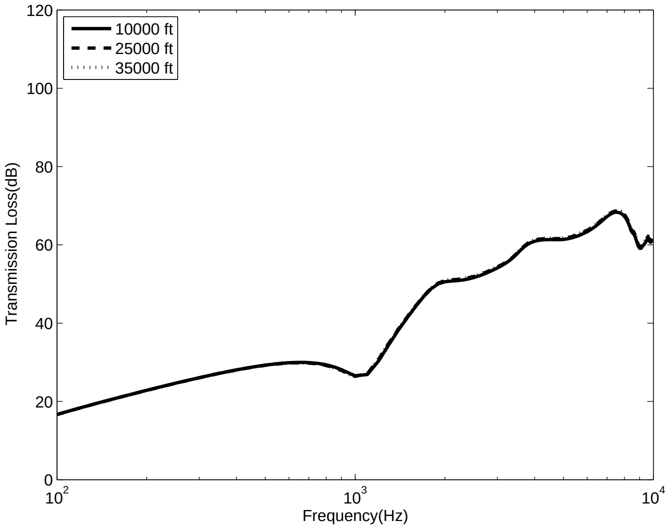

Figure 3.9: The variation of the transmission loss with frequency for different air gap pressures at $M = 0.5$ (BB).

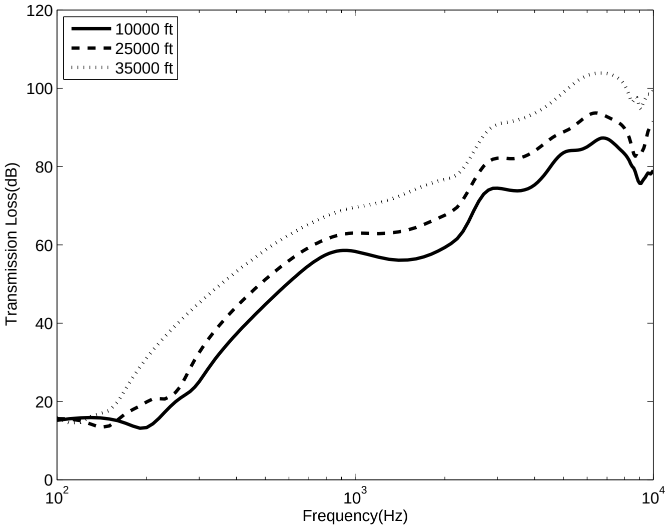

Figure 3.10: The variation of the transmission loss with frequency for different air gap pressures at $M = 0.5$ (BU).

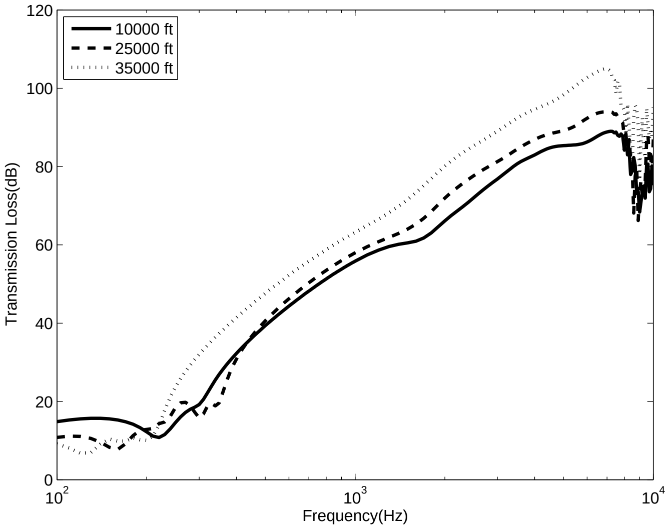

Figure 3.11: The variation of the transmission loss with frequency for different air gap pressures at $M = 0.5$ (UU).

3.6.3 The bi-objective optimisation problem and the Pareto front

Consider the problem of maximising the transmission loss through panels while simultaneously minimising the weight of the structure. Since the two objectives may, in general, require a trade-off the problem is one of determining the Pareto front of the bi-objective problem. As discussed previously, the BU configuration provides satisfactory transmission loss in both the low and the high frequency ranges. Therefore, we only consider this configuration here. The separation between the two plates here is fixed at 27 mm.

The density and the thickness of the porous material will be used as the variables for the optimization. The thickness H of the porous material takes values in the range 2-25 mm for the BU configuration. The bulk density of solid phase of porous ρ_1 takes values in the range of 10-30 kg/m^3. Correspondingly, the mass of the porous material equals $\rho_1 H$. Other parameters used in the calculations are the same as those used in the previous analysis. People have different hearing sensitivity to different frequencies of sound. The ear is most sensitive in the frequency range 500-5000 Hz [89]. A-weighting function is used here for the seven frequencies (1000, 1250, 1600, 2000, 2500, 3150 and 4000 Hz) in the range of 1000-4000 Hz. The normalized weights w_n are listed in Table 3.4 [86].

Table 3.4: Normalized weights using the A-weighting [86].

Frequency Hz	A-weighting dB(A)	Multiplier $10^{\mathrm{dB(A)}/10}$	Normalized weights
1000	0	1.000	0.1156
1250	+0.6	1.148	0.1327
1600	+1.0	1.259	0.1455
2000	+1.2	1.318	0.1524
2500	+1.3	1.349	0.1559
3150	+1.2	1.318	0.1156
4000	+1.0	1.259	0.1455
			1.0000

In order to satisfy the coincidence, minimizing the inverse of TL (1/TL) is minimised instead of maximizing TL. An open source code (Cao [90]) was used here for searching the Pareto front. Cao implemented the algorithm as a mex function, which is called a gateway function in programming language C. The algorithm considers the logical relationship between dominated and nondominated points to avoid unnecessary comparisons as much as possible so that the overall operations reduced from $n \times n \times m$ for an $n \times m$ problem to $r \times n \times m$, where r is the size of the final Pareto Front. In order to compare results with the work of Bolton et al. [28] for special cases, we initially discuss the case without flow at ground condition. The Pareto front is shown in Figure 3.12. It can be seen that increasing the mass of the porous material, until about 0.2 kg/m^2, increases the transmission loss. If we continue increasing the weight of the structure, the transmission loss will decrease, because the space of air gap is decreased which makes the whole construction tend to the BB configuration. The BB configuration only provides good performance at lower frequency. The design considered by Bolton et al. [28] for the BU configuration is also presented in Figure 3.12 using a ‘square’. It can be seen that there exist several designs that are superior to the one studied by Bolton [28] on both counts of weight and acoustic performance. These points are in the rectangle below and left of the point representing the design studied by Bolton. When we choose the weight of Pareto optimal solution equal to 0.2 kg/m^2, the relevant density and thickness (non-dominated point) are $\rho_1 = 10$ kg/m^3 and $H = 20$. Figure 3.13 shows the optimum result compared with Bolton's result for the BU configuration. Except for the mass control region [58] (here 260 Hz-1000Hz), the optimum result yields a better transmission loss, but it costs less mass and space. It should be noted here that the optimization is carried out in the frequency range 1 to 4 KHz. Therefore, if we focus on the frequency band of the mass control region, another optimized panel can be found to provide a better sound insulation than that of Bolton et al. [28] in the mass control region. Of course, this optimized panel possesses greater mass.

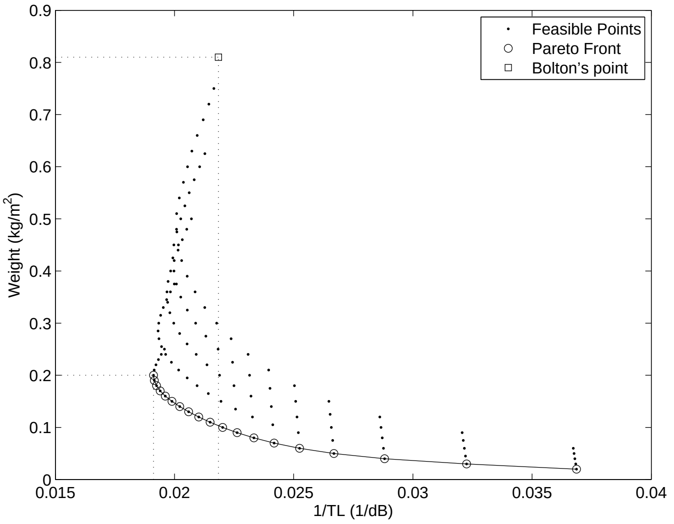

Figure 3.12: Obtained Pareto front in the objective space 1/TL and weight.

When taking the cruising condition (by means of the air gap pressure and the external mean flow) into account, the Pareto front shifts outwards with the air gap pressure. For $M = 0.5$, this is shown in Figure 3.14. It is also assumed that the condition on the incidence side and the transmission side are kept corresponding to an altitude of 35000 ft and 10000 ft, respectively. At a given value of weight, the lower pressure between the two face plates provides a better sound insulation, which is consistent with the result obtained in section 3.6.2. TL is more sensitive to the weight at the higher pressure condition between the two face plates. When the weight increases from 0.02 kg/m^2 to 0.14 kg/m^2, the TL of the pressure according to 10000 ft and 35000 ft increases by 52.09% and 12.75%, respectively.

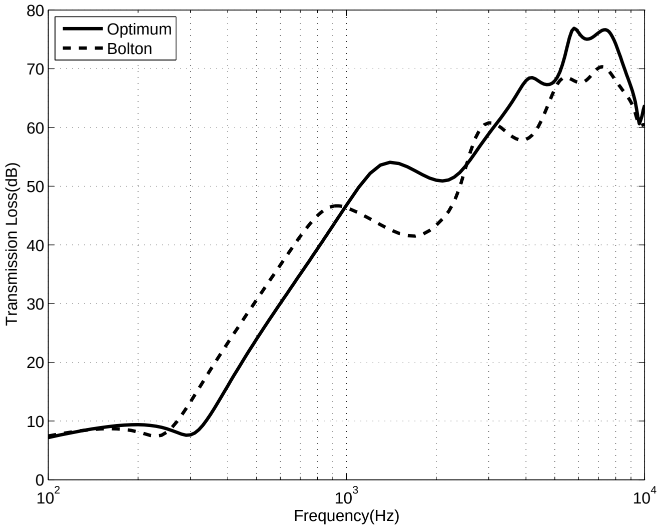

Figure 3.13: Comparison of transmission loss for the BU configurations.

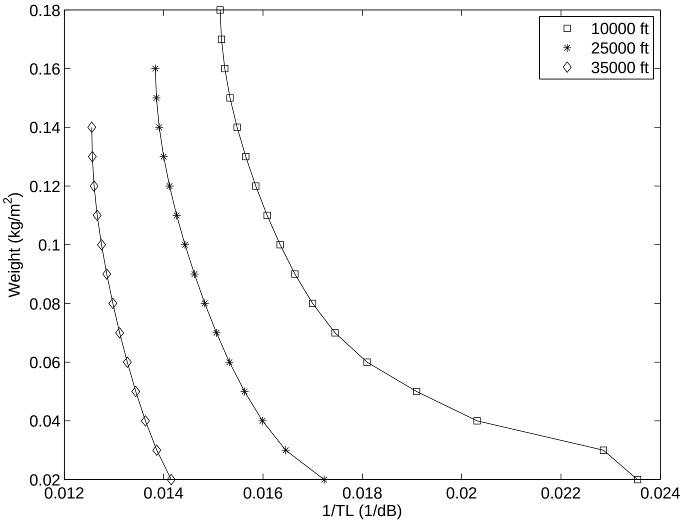

Figure 3.14: Pareto front in different pressures between two face plates at $M = 0.5$.

3.6.4 Laminated composite face plate and the effect of stacking sequence

Composite materials are widely used in various engineering applications including mechanical, marine, automotive, as well as aerospace engineering due to their light weight and high stiffness. Besides the accessories, the fuselage and the wings increasingly being made of composite material, e.g. these in A350 XWB of Airbus or B787 of Boeing. Therefore, a good understanding of the sound transmission through the sandwich structures with laminated composite face plates is of great current interest.

In this sub-section, we employ a simplification in the analysis by the use of the so-called 'equivalent fluid model' for the porous material as proposed by Lee et al. [81]. Lee et al. [81] noticed that, for different configurations, the relative importance of the strain energy associated with the three types of waves is considerably different. We adapt this simplification in the present work and model the porous material as an equivalent fluid by using the wave number of the strongest wave and its corresponding equivalent density in our calculations. The strength of the waves through porous medium depends on the material properties and the configuration of the sandwich lay-up. The relative importance of the wave types can be inferred from analysis on a full Biot's model described in section 3.2–this is summarized in Table 3.5. The expressions of k_{I}, k_{II}, ρ_{11}^* and ρ_{22}^* have been presented in section 3.2. The strongest wave in the BB configuration is the frame wave. In the low frequency range, the airborne wave is the dominant wave, while the frame wave is the strongest wave in high frequency range. The airborne wave is the dominant wave in the UU configuration [81]. It has been pointed out by Lee et al. [81] that the difference between the equivalent method and the full method including all the waves is less than 5 dB. Since the equivalent fluid method reduces the porous material to a fluid, most of the widely available analysis methods can be used without any modifications. This is the reason why the reduced method (equivalent fluid model) is applied in this work.

Table 3.5: The equivalent parameters of porous material for different configurations

Configurations	Strongest wave	Bulk density
BB	k_{II}	ρ_{11}^*
BU	k_{I} (low frequency range)	ρ_{22}^* (low frequency range)
BU	k_{II} (high frequency range)	ρ_{11}^* (high frequency range)
UU	k_{I}	ρ_{22}^*

Consider the BB configuration (see Figure 3.2a) of the panel. Since the equivalent fluid model of porous material is used, the problem is similar to that of sound transmission through double-leaf. The only difference is that the fluid between the two face plates is the equivalent fluid of the porous material, but not the air. The equations of motion of the two ply composite thin plates can be written as follows, respectively:

$$\begin{bmatrix} L_{11} & L_{12} & L_{13} \\ L_{21} & L_{22} & L_{23} \\ L_{31} & L_{32} & L_{33} \end{bmatrix} \begin{bmatrix} u_1 \\ v_1 \\ w_1 \end{bmatrix} + \begin{bmatrix} -I_1 & 0 & 0 \\ 0 & -I_1 & 0 \\ 0 & 0 & I_1 \end{bmatrix} \frac{\partial^2}{\partial t^2} \begin{bmatrix} u_1 \\ v_1 \\ w_1 \end{bmatrix} = \begin{bmatrix} 0 \\ 0 \\ p_1 - p_2 \end{bmatrix} \quad (3.66)$$

$$\begin{bmatrix} L_{11} & L_{12} & L_{13} \\ L_{21} & L_{22} & L_{23} \\ L_{31} & L_{32} & L_{33} \end{bmatrix} \begin{bmatrix} u_2 \\ v_2 \\ w_2 \end{bmatrix} + \begin{bmatrix} -I_2 & 0 & 0 \\ 0 & -I_2 & 0 \\ 0 & 0 & I_2 \end{bmatrix} \frac{\partial^2}{\partial t^2} \begin{bmatrix} u_2 \\ v_2 \\ w_2 \end{bmatrix} = \begin{bmatrix} 0 \\ 0 \\ p_2 - p_t \end{bmatrix} \tag{3.67}$$

in which $\{u_1, v_1, w_1\}$ and $\{u_2, v_2, w_2\}$ are the displacement components corresponding to the x, y and z axes for the incident side plate and the transmitted side plate, respectively. L_{ij} are the differential operators and I_i are the inertia terms of the plate, which can be found in the reference [91]. The expressions for the pressures p_1, p_2 and p_t in each region are same as those in section 3.3.

At the interfaces, the following boundary conditions must be satisfied

$$\frac{\partial p_1}{\partial z} = -\rho_i \left(\frac{\partial}{\partial t} + V \cdot \frac{\partial}{\partial x} \right)^2 w_1 \bigg|_{z=0} \tag{3.68}$$

$$\frac{\partial p_2}{\partial z} = -\rho_2 \frac{\partial^2 w_1}{\partial t^2} \bigg|_{z=0} \tag{3.69}$$

$$\frac{\partial p_2}{\partial z} = -\rho_2 \frac{\partial^2 w_2}{\partial t^2} \bigg|_{z=H} \tag{3.70}$$

$$\frac{\partial p_t}{\partial z} = -\rho_t \frac{\partial^2 w_2}{\partial t^2} \bigg|_{z=H} . \tag{3.71}$$

Since the frame wave is the dominant wave in this configuration, the bulk density $\rho_2 = \rho_{11}^*$ is chosen as the density of the equivalent fluid. Substitution of the harmonic expressions of the displacements and the pressure into the equations of motion of the plates and boundary conditions yields to ten algebraic equations. The transmission loss of the laminated composite sandwich structure can then be obtained by using the same analysis procedure as that described in section 3.4.

For the numerical calculations, the material constants of the laminated graphite/epoxy panels are $\rho = 1600$ kg/m^3, $E_\alpha = 221$ GPa, $E_\beta = 6.9$ GPa, $\mu_{\alpha\beta} = 0.25$, and $G_{\alpha\beta} = 4.8$ GPa, where α and β denote the local coordinates of fibers [91]. The plies of the panels in the incident side and transmitted side are arranged in the stacking sequence [90°/0°/90°/0°] and [0°/90°/0°/90°], respectively. The thicknesses of the two face plates are the same equal to 1.59 mm. The parameters of the porous material are taken from Table 3.1.

Figure 3.15 shows that the transmission loss increases with the increase of Mach number for ground conditions. The external mean flow yields 3-6 dB increase in TL when compared with the no flow condition. This phenomenon is same as that of the isotropic plates (see section 3.6.1), because the Mach number increases the impedance of the panel. When the thickness of the plate is fixed at 1.59 mm, the effect of the stacking sequence is shown in Figure 3.16. For both of the symmetric cross-ply (Figure 3.16a) and the antisymmetric cross-ply (Figure 3.16b), as the number of ply groups increases, the dip at the critical frequency goes down. This phenomenon is more obvious in the case of symmetric cross-ply. This is because the stacking of many ply groups reduces the orthotropy and the laminate becomes quasi-homogeneous [92]. The stacking sequence cannot change the transmission loss in the mass-controlled region, but alter the transmission loss in the coincidence-controlled region. This effect is more pronounced for the case of symmetric cross-ply. It is obvious that the case of symmetric cross-ply provides a better performance than the case of antisymmetric cross-ply does when the frequency is higher than the critical frequency.

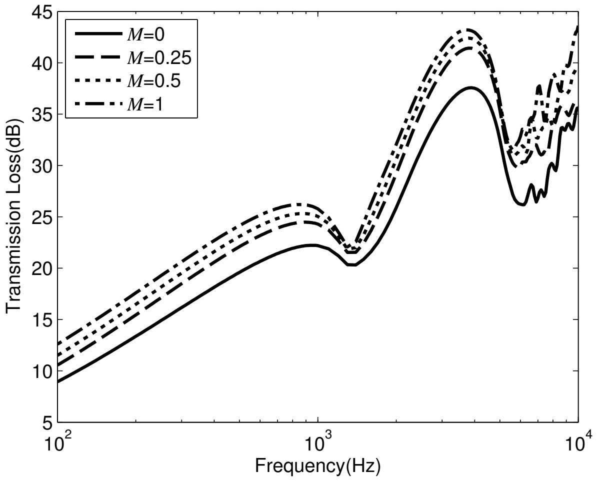

Figure 3.15: The variation of the transmission loss with frequency for different Mach numbers (BB with laminated composite face plates).

3.7 Conclusions

In this chapter, a mathematical model is developed incorporating the effects of external mean flow on the sound transmission through double-panel sandwich lined with poroelastic material. Flow on one side of the double-panel constructions is considered in order

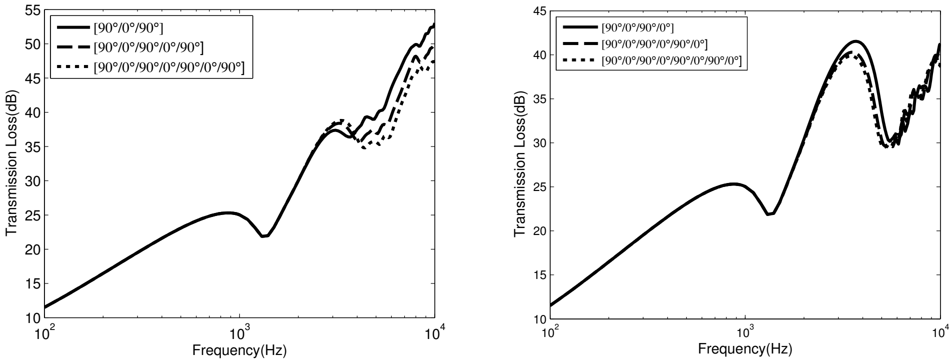

(a) Symmetric Cross-Ply (b) Antisymmetric Cross-Ply

Figure 3.16: The variation of the transmission loss with frequency for different stacking sequence at $M = 0.5$.

to make the modelling realistic for simulating flight condition. Of course, fuselage is not flat. However, it is common to consider a simplified geometry for sound transmission study in order to gain physical insight. Biot's model is used to describe the porous material as a continuum. The transmission loss for three types of configurations (BB, BU and UU) is calculated as a function of frequency in a diffuse sound field. The effect of the mean flow is brought out. The following general conclusions can be drawn:

i. The transmission loss increases with increasing the Mach number of the external mean flow. The reason is that the external mean flow increases the impedance of the panel.

ii. The BB configuration provides more stiffness in the air gap, due to the mechanical bonding of the layers. This increases the stiffness of the system and, therefore, the resonance frequency. The critical frequency is only affected by the panels' geometry and properties. The dips in the TL curves move according to this stiffening effect.

iii. TL increases gradually when the pressure difference between air gap and that on the exterior decreases. This effect is significant for the BU and the UU configurations, but not so much for the BB configuration. This is mainly attributed to the mismatch in the characteristic impedances of the exterior and the interior. The BU and UU configurations offer a better performance of sound insulation than the BB configuration does, in most of the frequency range. The reason is that the BB configuration provides more stiffness in the air gap between two face plates due to the mechanical bonding of the layers. The air gap plays a very important role in sound insulation.

iv. There is a clear trade-off between the acoustic performance and the weight of the panel. There exists a critical point on the weight vs. acoustic performance (quantified by 1/TL) plane indicating that the acoustic performance cannot be improved further. Below the critical point identified on the Pareto-front, the transmission loss increases at the expense of increasing the weight. In this way, we are able to find structures that are superior acoustically as well as with regards to the total weight when compared with some previously studied configurations (e.g. that studied by Bolton et al. [28]) When the effect of the pressure between the two face plates is taken into account, the Pareto-fronts move outwards with increasing pressure inside the panels.

v. The number of ply groups of symmetric cross-ply laminated composite sandwich panel has a significant effect on the transmission loss. The stacking sequence can alter the transmission loss, especially for the symmetric cross-ply. This work shows that the symmetric cross-ply panel provides a better performance than the antisymmetric cross-ply panel. It should be noted that this may be only a valid conclusion for sound insulation performance. For other aircraft preliminary design factors, e.g. structural loading, this may be not true. Therefore, the balance needs to be found which maximizes the performance in one field without degrading it in another.

Chapter 4

Sound transmission through double-walled cylindrical shells

In Chapter 3, the sound transmission through a double-walled flat panel was studied. However, the flat plate model is not adequate to simulate aircraft cabin, especially under flight conditions. The in-plane vibration is coupled with the transverse vibration for cylindrical shells structures. This changes the acoustic characteristics of the system. Therefore, the effect of the curvature and the porous material on sound transmission should be considered simultaneously under flight condition. With these motivations, sound transmission through a system of double shells, lined with poroelastic material in the presence of external mean flow, is investigated in this Chapter.

4.1 Description of the system

A typical fuselage is a double-shell system. To simulate the cruising condition, an external mean flow V is assumed to align with the axis of two infinite concentric cylindrical shells; see Figure 4.1. The radii of the shells are R_1 and R_2 and the wall thicknesses are h_1 and h_2 for the outer and the inner shells, respectively. A plane pressure wave transmits through the system from the external mean flow side into the cavity with static air. Without loss of generality, the incident angle α is in the plane for which $\theta = \pi$, see Figure 4.2. The fluid media on the incident side and the transmitted side have physical properties (ρ_i, c_i) and (ρ_t, c_t), respectively. Recently, the porous material was investigated for replacing the glass fiber in the aircraft sidewall [18]. The poroelastic material is placed in the annular space as shown. Three types of configurations are again considered here as shown on the right side of Figure 4.1. The equivalent fluid of porous material proposed by Lee et al. [81] is used to describe the porous material. They noticed that the relative importance of the strain energy associated with the three types of waves in the porous material, two compression waves and one shear wave (see section 2.4 of Chapter 2), is considerably different. This method is also adapted in the study of section 3.6.4 in Chapter 3.

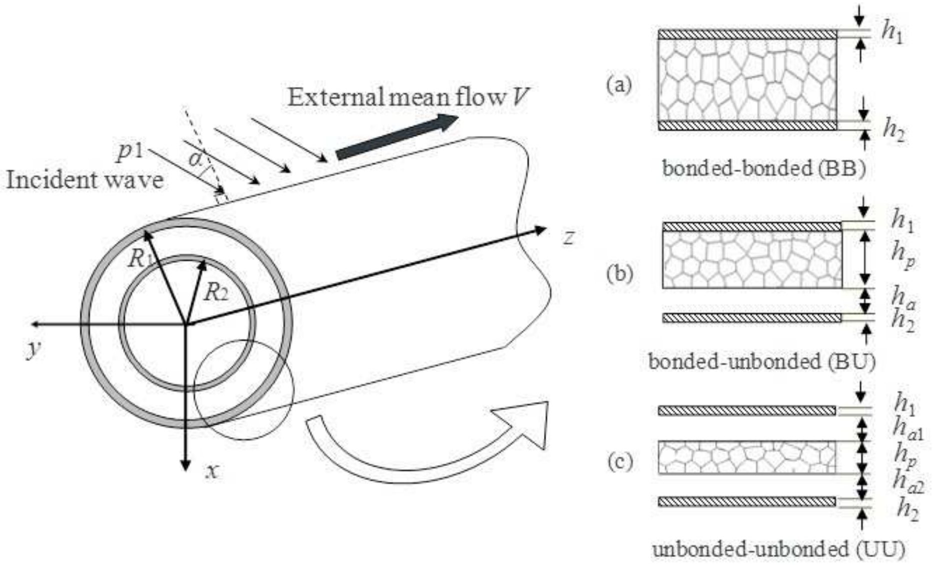

Figure 4.1: A sketch showing the sound wave transmission problem through the double shells system. Different configurations: (a) bonded-bonded (BB); (b) bonded-unbonded (BU); (c) unbonded-unbonded (UU).

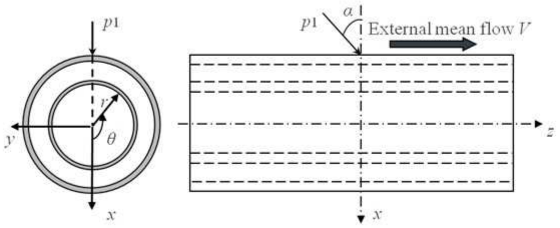

Figure 4.2: Two views of the double shells system.

4.2 Governing equations

For the shells, let $\{u_j^0, v_j^0, w_j^0\}$ be the displacement components at the neutral surface in the axial, circumferential and the radial directions, where the subscript j denotes the shell numbering which for the outer shell is $j = 1$ and for the inner shell is $j = 2$. Love's thin shell theory [93] is used to describe the motion of the two shells. The equations of motion can be expressed as

$$
\begin{aligned}
L_1\{u_j^0, v_j^0, w_j^0\} &= \rho_{sj} h_j \ddot{u}_j^0 && (4.1)\\
L_2\{u_j^0, v_j^0, w_j^0\} &= \rho_{sj} h_j \ddot{v}_j^0 \qquad (j = 1, 2) && (4.2)\\
L_3\{u_j^0, v_j^0, w_j^0\} + \Delta p_j &= \rho_{sj} h_j \ddot{w}_j^0 && (4.3)
\end{aligned}
$$

where ρ_{sj} are h_j are the density and the thickness of the shell, respectively. Δp_j is the pressure difference between the two sides of the shell. L_1, L_2 and L_3 are linear differential operators for the circular cylindrical shell which are presented in the Appendix D.

Figure 4.1a shows the details of two concentric shells lined with porous in the BB configuration. The exterior and the interior can be divided into three regions: the incident region, the porous material region and the transmitted region. In the exterior space, the pressure wave equation is given by

$$
c_i^2 \nabla^2 (p_1^I + p_1^R) + \left(\frac{\partial}{\partial t} + \mathbf{V} \cdot \nabla \right)^2 (p_1^I + p_1^R) = 0 \tag{4.4}
$$

where ∇^2 is the Laplacian operator and ∇ is the gradient operator. $\mathbf{V} = V\vec{k}$ is the external flow velocity vector in the z-direction. Note the influence of the flow velocity on the acoustic wave propagation via the convective term in the operator that appears in the second term. p_1^I is the incident wave and p_1^R is the scattered wave. As stated previously, the porous material is treated as an equivalent fluid. Thus, we can assume that there exist both a scattered acoustic wave p_2^R and a transmitted wave p_2^T in the porous layer. The wave equation in the porous material layer therefore becomes

$$
c_2^2 \nabla^2 (p_2^T + p_2^R) + \frac{\partial^2}{\partial t^2} (p_2^T + p_2^R) = 0. \tag{4.5}
$$

In the interior cavity, the wave equation can be expressed as

$$c_t^2\nabla^2 p_3^T + \frac{\partial^2 p_3^T}{\partial t^2} = 0. \tag{4.6}$$

The pressure term in Eq. (4.3) on the incidence side is given by

$$\Delta p_1 = (p_1^I + p_1^R) - (p_2^T + p_2^R), \tag{4.7}$$

and that on the transmitted side is given by

$$\Delta p_2 = (p_2^T + p_2^R) - p_3^T, \tag{4.8}$$

which differ from the equations of motion of the outer shell in terms of the pressure term in the last equation and the shell displacement variable being related to the inner shell.

At the interfaces between the elastic shells and the fluids, the following boundary conditions must be satisfied

$$\frac{\partial(p_1^I + p_1^R)}{\partial r} = -\rho_i \left(\frac{\partial}{\partial t} + \mathbf{V}\cdot\nabla\right)^2 w_1^0 \bigg|_{r=R_1} \tag{4.9}$$

$$\frac{\partial(p_2^T + p_2^R)}{\partial r} = -\rho_2 \frac{\partial^2 w_1^0}{\partial t^2}\bigg|_{r=R_1} \tag{4.10}$$

$$\frac{\partial(p_2^T + p_2^R)}{\partial r} = -\rho_2 \frac{\partial^2 w_2^0}{\partial t^2}\bigg|_{r=R_2} \tag{4.11}$$

$$\frac{\partial p_3^T}{\partial r} = -\rho_t \frac{\partial^2 w_2^0}{\partial t^2}\bigg|_{r=R_2}. \tag{4.12}$$

Since the frame wave is the dominant wave in the BB configuration, the bulk density $\rho_2 = \rho_{11}^*$ is chosen as the density of the equivalent fluid.

In the cylindrical coordinates, a harmonic incident wave p_1^I can be expressed as

$$P_1^I(r,\theta,z,t) = p_0 \sum_{n=0}^{\infty} \varepsilon_n (-i)^n J_n(k_{1r} r)\cos n\theta e^{i(\omega t - k_{1z} z)} \tag{4.13}$$

where p_0 is the amplitude of the incident wave; n is the circumferential mode number; $\varepsilon_n = 1$ for $n = 0$ and $\varepsilon_n = 2$ otherwise; $i = \sqrt{-1}$; J_n is the Bessel function of the first kind of order n; ω is the angular frequency. The wave numbers k_{1z} and k_{1r} in Eq. (4.13) are

$$k_{1r} = k_1 \cos\alpha,\ k_{1z} = k_1 \sin\alpha,\ \text{with } k_1 = (\omega/c_i)(1 + M\sin\alpha)^{-1} \tag{4.14}$$

where the Mach number of the external mean flow is given by $M = V/c_i$.

In the porous layer, the wave number k_{II} is treated as an equivalent wave number. Therefore, the equivalent sound speed $c_2 = \omega/k_{\mathrm{II}}$, and the wave numbers can be defined respectively as

$$k_{2z} = k_{1z},\ k_{2r} = \sqrt{k_{\mathrm{II}}^2 - k_{2z}^2}. \tag{4.15}$$

Similarly on the transmitted side, the wave numbers are given by

$$k_3 = \omega/c_t,\ k_{3z} = k_{1z},\ k_{3r} = \sqrt{k_3^2 - k_{3z}^2}. \tag{4.16}$$

In order to satisfy Eq. (4.4) to (4.6), p_1^R, p_2^T, p_2^R and p_3^T, can be expressed as

$$p_1^R(r,\theta,z,t) = \sum_{n=0}^{\infty} p_{1n}^R H_n^2(k_{1r}r)\cos n\theta e^{i(\omega t - k_{1z}z)} \tag{4.17}$$

$$p_2^T(r,\theta,z,t) = \sum_{n=0}^{\infty} p_{2n}^T H_n^1(k_2 r)\cos n\theta e^{i(\omega t - k_{1z}z)} \tag{4.18}$$

$$p_2^R(r,\theta,z,t) = \sum_{n=0}^{\infty} p_{2n}^R H_n^2(k_2 r)\cos n\theta e^{i(\omega t - k_{1z}z)} \tag{4.19}$$

$$p_3^T(r,\theta,z,t) = \sum_{n=0}^{\infty} p_{3n}^T H_n^1(k_3 r)\cos n\theta e^{i(\omega t - k_{1z}z)} \tag{4.20}$$

where p_{1n}^R, p_{2n}^T, p_{2n}^R and p_{3n}^T are the complex amplitudes. H_n^1 and H_n^2 are Hankel functions of the first and second kinds of order n, respectively. Hankel functions arise due to the cylindrical geometry.

Since the trace wavelengths must match on the boundary, the displacement components of the shells u_1^0, v_1^0, w_1^0, u_2^0, v_2^0 and w_2^0 can be expressed as

$$u_1^0(\theta,z,t)=\sum_{n=0}^{\infty}u_{1n}^0\cos n\theta e^{i(\omega t-k_{1z}z)} \tag{4.21}$$

$$v_1^0(\theta,z,t)=\sum_{n=0}^{\infty}v_{1n}^0\sin n\theta e^{i(\omega t-k_{1z}z)} \tag{4.22}$$

$$w_1^0(\theta,z,t)=\sum_{n=0}^{\infty}w_{1n}^0\cos n\theta e^{i(\omega t-k_{1z}z)} \tag{4.23}$$

$$u_2^0(\theta,z,t)=\sum_{n=0}^{\infty}u_{2n}^0\cos n\theta e^{i(\omega t-k_{1z}z)} \tag{4.24}$$

$$v_2^0(\theta,z,t)=\sum_{n=0}^{\infty}v_{2n}^0\sin n\theta e^{i(\omega t-k_{1z}z)} \tag{4.25}$$

$$w_2^0(\theta,z,t)=\sum_{n=0}^{\infty}w_{2n}^0\cos n\theta e^{i(\omega t-k_{1z}z)} \tag{4.26}$$

where u_{1n}^0, v_{1n}^0, w_{1n}^0, u_{2n}^0, v_{2n}^0 and w_{2n}^0 are the unknown complex amplitudes.

Substitution of Eqs. (4.13)-(4.21) into Eqs. (4.1)-(4.12) yields a set of algebraic equations that can be arranged in the following matrix form

$$\begin{bmatrix} 0 & 0 & 0 & 0 & A & B & C & 0 & 0 & 0 \\ 0 & 0 & 0 & 0 & D & E & F & 0 & 0 & 0 \\ G & H & I & 0 & J & K & L & 0 & 0 & 0 \\ M & 0 & 0 & 0 & 0 & 0 & N & 0 & 0 & 0 \\ 0 & O & P & 0 & 0 & 0 & Q & 0 & 0 & 0 \\ 0 & 0 & 0 & 0 & 0 & 0 & 0 & R & S & T \\ 0 & 0 & 0 & 0 & 0 & 0 & 0 & U & V & W \\ 0 & X & Y & Z & 0 & 0 & 0 & A1 & B1 & C1 \\ 0 & D1 & E1 & 0 & 0 & 0 & 0 & 0 & 0 & F1 \\ 0 & 0 & 0 & G1 & 0 & 0 & 0 & 0 & 0 & H1 \end{bmatrix} \begin{Bmatrix} p_{1n}^R \\ p_{2n}^T \\ p_{2n}^R \\ p_{3n}^T \\ u_{1n}^0 \\ v_{1n}^0 \\ w_{1n}^0 \\ u_{2n}^0 \\ v_{2n}^0 \\ w_{2n}^0 \end{Bmatrix} = \begin{Bmatrix} 0 \\ 0 \\ I1 \\ J1 \\ 0 \\ 0 \\ 0 \\ 0 \\ 0 \\ 0 \end{Bmatrix} \tag{4.27}$$

where the terms within the matrix equation are given in Appendix E.

The ten unknowns in the column vector on the left side of Eq. (4.27) can be solved simultaneously. The relevant unknowns for BU and UU configurations can be obtained in a similar manner. Details of the expressions relevant for these two configurations are given in the Appendix F and Appendix G, respectively.

4.3 Transmission loss

The transmission coefficient is defined by

$$\tau = \frac{W^T}{W^I} \tag{4.28}$$

In Eq.(4.28), the transmitted sound power per unit length of the shell W^T is

$$W^T = \frac{1}{2}\mathrm{Re}\left\{\int_{S_2}\left(p_3^T \frac{\partial (w_2^0)^*}{\partial t}\right) dS\right\} \tag{4.29}$$

where $S_2 = 2\pi R_2$, $\mathrm{Re}\{\cdot\}$ and the superscript * represent real part and the complex conjugate of the argument, respectively. Substituting the expressions of p_3^T and w_2^0 into Eq. (4.29), the expression for W^T can be rewritten as

$$W^T = \sum_{n=0}^{\infty} \frac{\pi R_2}{2\varepsilon_n}\mathrm{Re}\left\{p_{3n}^T H_n^1(k_{3r}r)(i\omega w_2^0)^*\right\}. \tag{4.30}$$

Similarly, W^I, the incident power per unit length along the axis of the shell is given by

$$W^I = \frac{R_1 \cos(\alpha)}{\rho_i c_i} p_0^2. \tag{4.31}$$

Therefore, the transmission coefficient can be obtained by substituting Eq. (4.30) and (4.31) into Eq. (4.28)

$$\tau(\alpha) = \sum_{n=0}^{\infty} \frac{R_2 Re\left\{p_{3n}^T H_n^1(k_{3r}r)(i\omega w_2^0)^*\right\}\rho_i c_i}{2\varepsilon_n R_1 \cos\alpha p_0^2} \tag{4.32}$$

Finally, the transmission loss is obtained as

$$\mathrm{TL} = 10\log_{10}\tau^{-1}. \tag{4.33}$$

4.4 Results and discussions

In this section, the transmission losses for infinite cylindrical shells for the three configurations described previously are presented. The effect of Mach number of the exterior mean flow on the transmission characteristics is investigated. The parameters of the porous material used for computations are: density of the solid phase $\rho_1 = 30$ kg/m^3; Young's modulus of the solid phase $E_m = 8 \times 10^5$; loss factor $\eta = 0.265$; bulk Poisson's ratio $\nu = 0.4$; flow resistivity $\sigma = 25000$ MKS Rayls/m; tortuosity $\alpha_\infty = 7.8$; porosity $\phi = 0.9$. The aluminium shells have the following properties: Young's modulus $E_s = 7 \times 10^{10}$ Pa; loss factor $\eta_s = 0.01$; Poisson's ratio $\mu = 0.33$; material density $\rho_s = 2700$ kg/m^3. The dimensions of the double-walled shells for different configurations are listed in Table 4.1.

Table 4.1: Geometrical parameters used in sandwich constructions of the three configurations studied.

Configurations	BB	BU	UU
Dimensions	$h_1 = 2$ mm	$h_1 = 2$ mm	$h_1 = 2$ mm
	$h_2 = 2$ mm	$h_2 = 2$ mm	$h_2 = 2$ mm
	$R_1 = 1.84$ m	$R_1 = 1.84$ m	$R_1 = 1.84$ m
	$R_2 = 1.80$ m	$R_2 = 1.80$ m	$R_2 = 1.80$ m
		$R_p = 1.81$ m	$R_{p1} = 1.835$ m
		$h_p = 30$ mm	$R_{p2} = 1.805$ m
		$h_a = 10$ mm	$h_p = 30$ mm
			$h_{a1} = 5$ mm
			$h_{a2} = 5$ mm

The procedure of computing transmission loss is outlined as follows. For a prescribed value of frequency, the column of complex amplitudes of pressures and displacements were obtained by solving the set of linear algebraic equations (4.27). Then, the transmission coefficient can be calculated by using the summation that appears in Eq. (4.32) at this frequency. The truncation of the infinite series was carried out by a convergence criterion on the transmission loss TL as calculated from Eq. (4.33): the number of terms was restricted the contribution from the next term in the series was less than 0.001 dB. The frequency band of calculations is from 10 Hz to 50 kHz. In the BU configuration, as mentioned previously, the airborne wave is the strongest component within the porous material in the low-frequency range (below 2 kHz) and the frame wave is the strongest component in the high-frequency range (above 4 kHz). Therefore, the calculations can be divided into three frequency ranges for the BU configuration: (a) 10-2000 Hz, the TL is obtain by only considering the airborne wave for the porous material; (b) 2000-4000 Hz, the average value of TLs corresponding to the airborne wave and the frame wave is adopted; (c) over 4000 Hz, the TL based on the frame wave is calculated. For the other two configurations considered here, there is no need to divide the frequency band of interest because only one type of wave is dominant in the entire frequency band of interest.

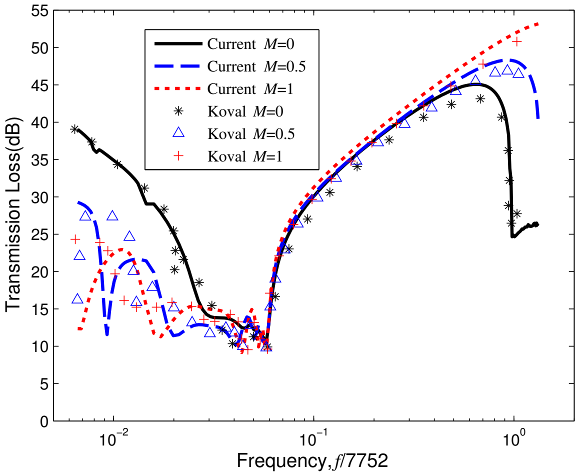

Figure 4.3: Transmission loss characteristics for a single shell structure ($\alpha = 45°$). Validation with Koval's results [35] that differ slightly in the equations of motion of the shell.

In order to validate our calculations, the numerical results are compared with those of Koval [35] who studied the special case of a single shell structure. The comparison is carried out for different Mach numbers when the incidence angle is fixed at $\alpha = 45°$ (see Figure 4.3). They match very well, especially in the frequency range between the two main dips. The locations of the dips, however, are a little different in this comparison. These can be attributed to two factors: Firstly, Love's theory is used here to describe the motion of the shell, while Koval [35] used the simplified Flügge-Lure-Byrne model. Secondly, Koval did not quote the values of the material properties of the aluminium shell and may have used slightly different values than ours. Further, we have attempted to compare the results with those of Lee et al. [41] who studied the sound transmission through a double-walled cylindrical shell without any porous lining (see Figure 4.4).

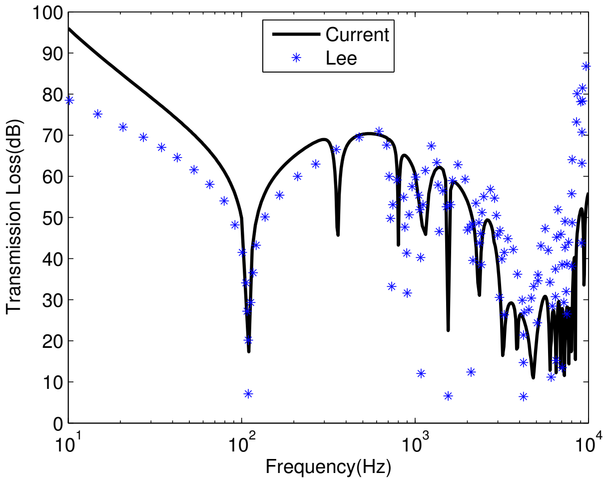

Figure 4.4: Comparison of our calculations with those of Lee et al. [41] for a double-walled cylindrical shell without porous material in the absence of flow at $\alpha = 45°$.

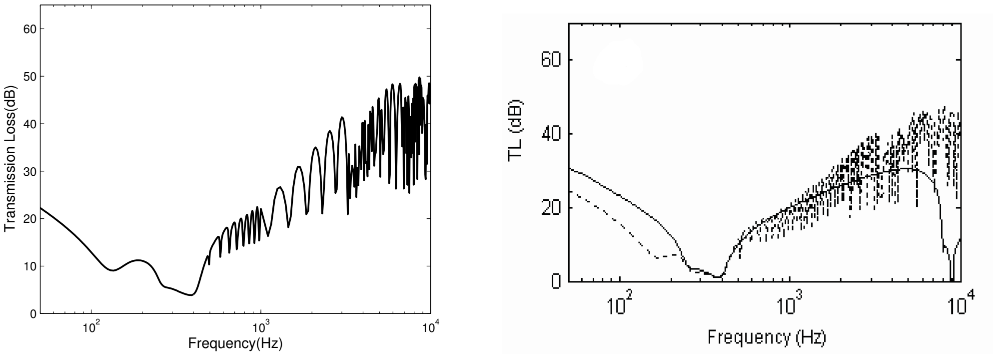

(a) Our calculations

(b) Liu et al. [44]

Figure 4.5: Validation for the oblique incidence at $\alpha = 60°$ without porous lining in the absence of flow.

Since we noted an error in their formulation of the shell differential operator L_2 and L_3 (see Eqs. (D.5) and (D.6) here), which results in some of the terms in the coefficient matrix of Eq. (4.27) becoming slightly different from those of Lee et al. [41], the result in our model is quite different from that of Lee's. The other special case available for comparison is a conference paper of Liu and Feng [44] who did not consider the external mean flow. The comparison is again very close for the oblique incidence (Figure 4.5a vs. dashed line in 4.5b). The difference can primarily be attributed to the differences in the shell mechanics adopted by Liu et al. (Donell-Mushtari) compared to this work (Love).

4.4.1 Generic transmission loss characteristics and the frequency dips

In order to understand the behaviour of the dependence of the transmission loss with frequency, we first consider the locations of the dips of the TL curve on the frequency axis. In particular there are differences with respect to the transmission characteristics for flat plates discussed in Chapter 3 that are characterized by two dips that correspond to the fundamental resonance of the plate and the coincidence frequency when a plane wave is incident on a plate at an arbitrary angle of incidence. This fundamental resonance is missing for infinite plates. When the sound wave field is diffuse, the dip corresponds to the critical frequency which is the value of the coincidence frequency at its lowest value–this value corresponds to the grazing incidence (see section 3.4 of Chapter 3).

The story, however, is significantly different for transmission through thin cylindrical shells. It has been documented before [94] that the TL characteristics exhibit three dips on the frequency axis. They are associated with (i) the ring frequency, (ii) critical frequency, and (iii) coincidence frequency. It is unfortunate that in the literature the latter two have been often used synonymously. We now take each of these three in turn.

(i) Ring frequency

The ring frequency is the frequency associated with the breathing mode resonance of the infinitely long shell [95]. At this frequency, the circumference of the shell equals the longitudinal wavelength.

$$f_r = \frac{c_L}{2\pi R}, \tag{4.34}$$

where the c_L is the longitudinal wave speed for a rod given by $c_L = \sqrt{E/\rho}$. Koval [35] used this value to validate the dips in the TL characteristics obtained by them. When the shell is not made of a single wall of elastic material but consists of several layers, Ghinet et al. [96] gave the expression of the ring frequency for an infinite sandwich composite and laminated composite cylinder as

$$f_r = \frac{1}{2\pi R}\sqrt{\left(A_{22} - \frac{B_{22}}{R}\right)\frac{1}{m_s}}, \tag{4.35}$$

where A_{22} and B_{22} are the terms from the **A** and **B** matrices familiar in the laminate theory. For the BB configuration, all the three–the exterior shell, the porous material and the inner shell would contribute to A_{22} and B_{22}.

(ii) Critical frequency

Blaise et al. [94] studied the location of the critical frequency for orthotropic cylindrical shells which corresponds to the trace wave number in the radial direction being equal to the shell circumferential wave number. The circumferential wave number equals the circumferential mode order divided by the radius of the shell. The expression of the critical frequency in the presence of mean flow can be obtained by specializing Eq. (20) of Blaise et al. [94] for $\psi = 0$, the angle between the projection of the incidence wave in the tangential plane and the z-axis.

$$f_{cr} = \frac{c_i^2(1 + M\sin\alpha)^2}{2\pi h}\sqrt{\frac{12\rho_s(1-\mu^2)}{E}}. \tag{4.36}$$

Note that the critical frequency depends on the angle of incidence in the presence of an external mean flow but it becomes independent of the incidence direction in the absence of the external flow. The latter was also observed experimentally by White [97] who used the term ‘coincidence frequency’ to describe this. In this paper, we use the word coincidence frequency for a third dip in the TL characteristics of a cylindrical shell which is consistent with the terminology used by Blaise et al. [94]. This dip is missing from the TL characteristics of flat plates, although the term critical frequency for transmission through plates is used to mean something else, i.e. the least value of coincidence corresponding to grazing incidence. Blaise et al. [94] termed this singularity as the critical pseudo-coincidence frequency. Most contemporary authors [2-5,7-10] designate this dip as one associated with the ‘critical frequency’; hence we will continue to use this term. Note that the dependence of the location of this dip on the angle of incidence disappears in the absence of flow (this can be concluded by setting $M = 0$). This will be discussed further while presenting the computed TL characteristics.

(iii) Coincidence frequency

The third dip in the TL characteristics features at a further higher frequency corresponding to the trace wave number in the tangential direction becoming equal to the circumferential wave number [94]. The expression in Eq. (18) of [94] when specialized to isotropic cylindrical shells becomes

$$f_{coin} = \frac{c_i^2(1 + M\sin\alpha)^2}{2\pi h \sin^2\alpha}\sqrt{\frac{12\rho_s(1-\mu^2)}{E}}. \tag{4.37}$$

Clearly, the coincidence frequency always depends on the incidence angle irrespective of the presence of the external flow.

The effect of Mach number on the critical and the coincidence frequencies can be seen in Table 4.2 where the angle of incidence is fixed to 45°. These theoretically calculated values will be compared with the dips observed in the transmission characteristics later. Likewise, the dependence of these two characteristic frequencies on the angle of incidence is presented in Table 4.3 and will be discussed in the light of calculated TL vs. frequency characteristics.

4.4.2 The effect of incidence angle in the absence of external flow

The variation of the transmission loss with frequency for different incidence angles in the BB configuration is presented in Figure 4.6. In the first instance, the Mach number here is set to zero and no pressure difference between the inside and the outside is assumed. The value of the ring frequency f_r for an isotropic shell can be estimated by using the following formula

$$f_r = \frac{1}{2\pi R}\sqrt{\frac{E}{\rho_s}}. \tag{4.38}$$

This value is calculated to be $f_r = 440.42$ Hz. For the BU and UU configurations, there is no direct material link between the outer shell and the inner shell due to the air gap. The ring frequency then is determined by the outer shell geometry and properties only. Therefore, Eq. (4.38) can be used to approximately estimate the ring frequency for these two configurations, after ignoring the effect of the porous material which is justified because of its low Young's modulus of the porous material. Using the laminate Eq. (4.35), the ring frequency is calculated as 509.32 Hz. The observed dip around 500 Hz in the TL characteristics calculated for BB configuration is very close to the estimated location marked by an arrow (see Figure 4.6). The region below f_r is a stiffness controlled region. The dips in the TL will appear due to the cylinder resonances when the trace wavelength and frequency match with that of a mode having the appropriate value of n, the circumferential mode number.

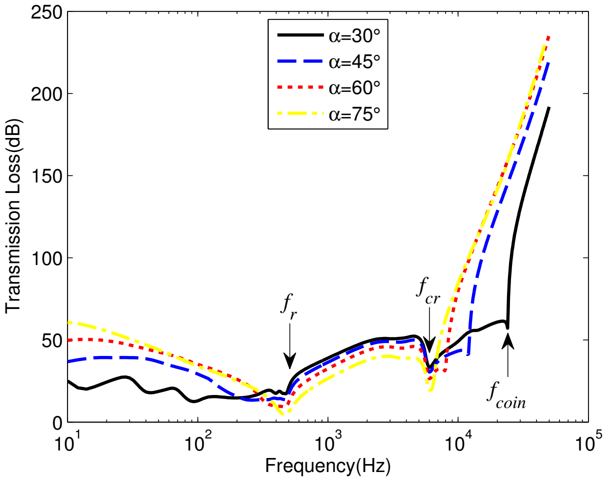

Figure 4.6: The variation of TL with frequency for different incident angles α (BB configuration), $M = 0$. The three dips are predicted as $f_r = 509.32$ Hz, $f_{cr} = 6013$ Hz and $f_{coin} = 24051$ Hz as calculated using Eqs. (4.35), (4.40) and (4.41) for 30°, respectively. Note the dependence of f_{coin} on the angle of incidence as seen here and consistent with Eq. (4.41) but not shown using arrows at all the frequencies for clarity of the figure.

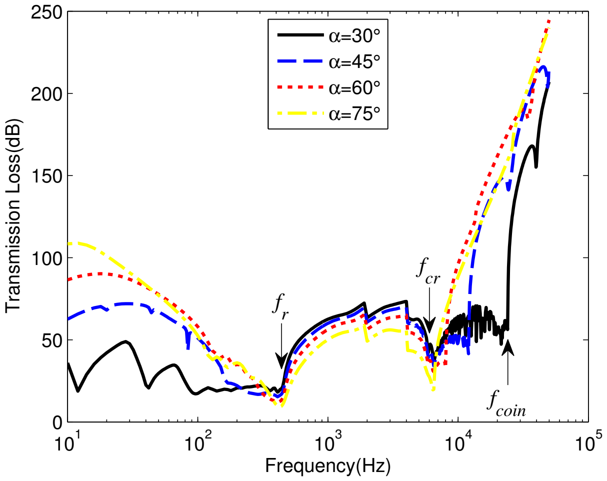

Figure 4.7: The variation of TL with frequency for different incident angles α (BU configuration), $M = 0$. The three characteristic dips are obtained as $f_r = 440.42$ Hz, $f_{cr} = 6013$ Hz and $f_{coin} = 24051$ Hz and they have been calculated using Eqs. (4.38), (4.40) and (4.41) for 30°, respectively. Note the independence of f_{cr} with respect to the angle of incidence for $M = 0$.

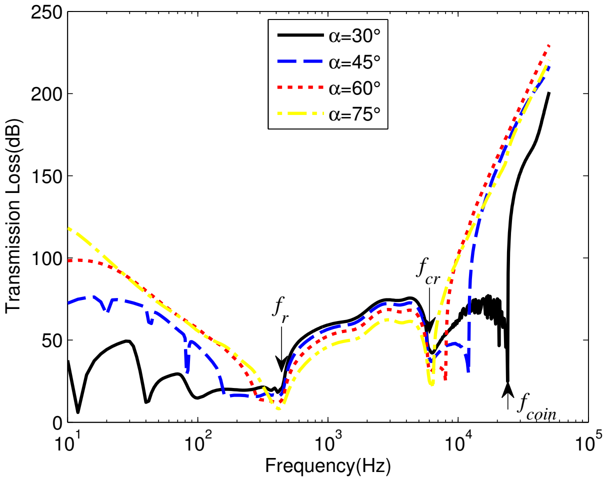

Figure 4.8: The variation of TL with frequency for different incident angles α (UU configuration), $M = 0$. The three characteristic frequencies are calculated as $f_r = 440.42$ Hz, $f_{cr} = 6013$ Hz and $f_{coin} = 24051$ Hz using Eqs. (4.38), (4.40) and (4.41) for 30°, respectively. Note the dependence of f_{coin} on the angle of incidence.

The TL characteristics are frequently partitioned into four regions of the frequency axis [58]: (i) the falling TL curve at the very low frequency end known as the stiffness-controlled region, (ii) a frequency band with several dips, each corresponding to a structural resonance–known as the resonance controlled region, (iii) a 5-6 dB/Octave rising curve known as the mass-controlled region, and finally (iv) the coincidence region characterized by the matching of the acoustic wavelengths with the structural wavelength. Figure 4.6 shows all these features. Although, the interest in the low frequency end of calculations is relatively less from the acoustic transmission perspective, in addition to the ring frequency described above, the resonances associated with the through thickness dilatation given by

$$f_{dilatation} = \frac{1}{2\pi}\sqrt{\frac{2E_m}{h_p(\rho_s h_s + \rho_1 h_p/6)}} \tag{4.39}$$

for flat panels are worth mentioning. This frequency is calculated as 425.5 Hz for BB configuration and is physically associated with the mass-spring-mass motion with the face plates providing inertia and the core providing stiffness. There are other possible resonances, e.g. horizontal shear of the sandwich. They correspond to the cut-off frequencies of the structural dispersion relationships. Some of these resonances are visible in Figure 4.6 and are clustered around the ring frequency. Note, however, that the resonances in a shell are expected to be significantly different because of the curvature effect and will be associated with anti-phase breathing motion of the two walls. Since our primary interest is in noise transmission, here we will not consider these further.

The next dip in the TL curve features at the critical frequency of the cylinder-air system. The expression of the critical frequency in the absence of external mean flow is now obtained by specializing Eq. (4.36) for $M = 0$ and is given by

$$f_{cr} = \frac{c_i^2}{2\pi h}\sqrt{\frac{12\rho_s(1-\mu^2)}{E}}. \tag{4.40}$$

The value of the critical frequency f_{cr} is calculated as 6013 Hz and is accordingly shown by an arrow marker in Figure 4.6. The transmission loss decreases as the incident angle increases below the ring frequency but increases between the ring frequency and the critical frequency. Between f_r and f_{cr}, the transmission loss follows a mass law which is of the order of 5-6 dB/Octave. Similar trends of TL variation can be found in the other two configurations. Transmission loss characteristics for the BU configuration and the UU configuration are presented in Figures 4.7 and 4.8. It is clear that the BU and UU configuration offers a better performance of sound insulation than the BB configuration does when we compare Figures 4.6, 4.7 and 4.8. The porous material connects the two shells in the BB configuration. The sound waves can propagate into the cavity more easily. Therefore, in practice, the two shells should to be separated by an air gap for superior acoustic performance. From the Figures 4.6 to 4.8, an interesting observation can be made that the critical frequency is independent of the incidence angle when the incident wave vector has no azimuthal component. White [97] also observed this phenomenon in the experimental study without any flow. However f_{cr} is indeed dependent on the angle of incidence in the presence of the external mean flow. This will be discussed later.

Unlike the critical frequency, the coincidence frequency f_{coin} always depends on the incidence angle. The α-dependence of the coincidence frequency can be noted from the Eq. (4.37), when specialized for $M = 0$,

$$f_{coin} = \frac{c_i^2}{2\pi h \sin^2\alpha}\sqrt{\frac{12\rho_s(1-\mu^2)}{E}}. \tag{4.41}$$

The coincidence frequency f_{coin} is approaches the critical frequency f_{cr} as the incidence angle approaches 90° which corresponding to the grazing incidence.

Going back to Figure 4.6, there are three clearly identifiable dips in the TL curve. However, the second and the third increasingly start to coalesce to the value of the critical frequency when α is increased. Therefore, only one recognizable dip can be seen visually when the incidence angle $\alpha = 75°$ since the two dips are too close to each other. This feature continues to be observed for the other two configurations in Figures 4.7 and 4.8 for BU and UU configurations respectively. TLs can be averaged for the incident angle in a diffuse field, but this makes the effect of other factors less transparent. Therefore, in the following analysis, while studying the influence of the external mean flow on transmission characteristics, an incident angle $\alpha = 45°$ is chosen to be fixed.

4.4.3 The effect of the external mean flow

In order to bring out the effect of the external mean flow, fixed properties corresponding to the ground condition are considered here and the Mach number is taken as the control parameter. The variation of the transmission loss corresponding to the three configurations with frequency at different Mach numbers is shown in Figures 4.9 to 4.11. The Mach number of the external flow is varied from $M = 0$ to $M = 1.5$. The TL decreases with some fluctuations below the ring frequency, but increases above the ring frequency following the increase of Mach number. This is consistent with the observations of Sgard et al. [98] that the mean flow can add the negative stiffness and the radiation damping into the system. Therefore, in the stiffness controlled region (i.e. below the ring frequency), the external flow decreases the sound transmission loss. However, the external flow provides a modest increase in transmission loss (about 1-5 dB) in the mass law region between f_r and f_{cr}. The external flow also shifts the critical frequency and the coincidence frequency up, but has no effect on the ring frequency because it depends on the structural parameters alone. The values of the critical frequency and the coincidence frequency calculated by the Eqs. (4.36) and (4.37) are listed in Table 4.2. The location of the dips in the TL characteristics matches closely with these tabulated values and has not been labeled in Figures 4.9 to 4.11 for visual clarity. Figures 4.9 to 4.11 also bring out that airflow gives a huge increase for transmission loss near the critical frequency f_{cr} (near the second dip in each curve) and above. These figures also indicate that the BU and UU configurations again show a better sound insulation than the BB configuration does in the presence of external mean flow.

Table 4.2: The variation of critical frequency and the coincidence frequency vary with the Mach number. The angle of incidence is fixed at 45°

Mach number	f_{cr} (Hz)	f_{coin} (Hz)
0	6013	12025
0.5	11016	22032
1	17522	35044
1.5	25532	51063

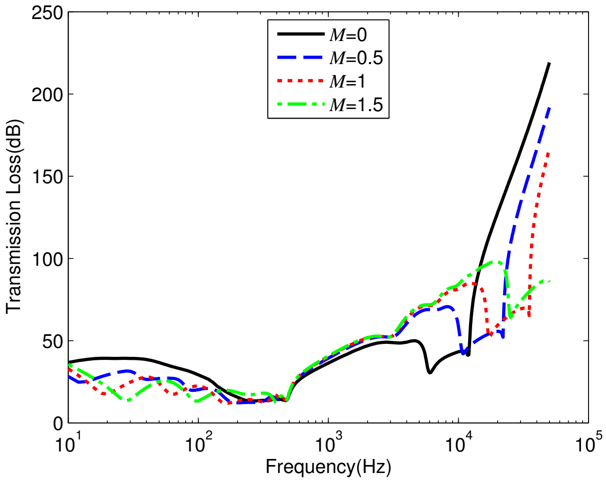

Figure 4.9: The variation of TL with frequency for different Mach numbers (BB). The locations of the dips for f_{cr} and f_{coin} are consistent with the predicted values presented in Table 4.2.

Eq. (4.36) indicates that the flow tends to increase the critical frequency. Consider the BB configuration, for example. Figure 4.12 shows that the variation of the transmission loss with frequency computed for different incidence angles in the BB configuration at $M = 0.5$. The external mean flow shifts the critical frequency up. It should be noted that, in the presence of flow, the critical frequency is dependent on the incidence angle, which is not the case in the absence of flow because the term $M \sin \alpha$ combines the flow parameter with the direction of incidence (see Table 4.3).

4.4.4 The effect of porous material

In order to understand the effect of porous material on the sound transmission in the presence of the external mean flow, only one shell and two shells without the porous material are considered first. The effect of the external flow is also taken out initially.

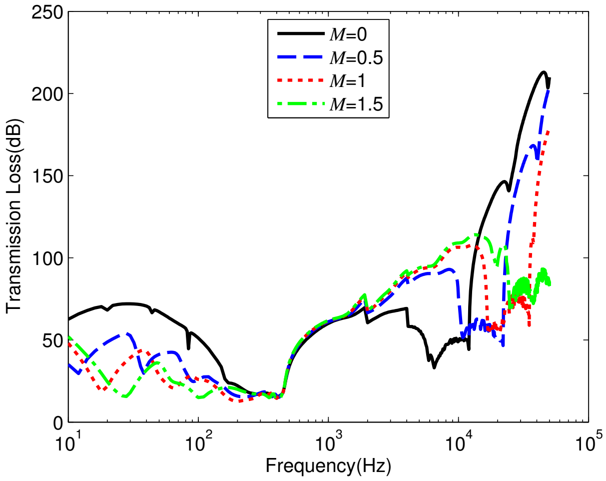

Figure 4.10: The variation of TL with frequency for different Mach numbers (BU). The locations of the dips for f_{cr} and f_{coin} are consistent with the predicted values presented in Table 4.2.

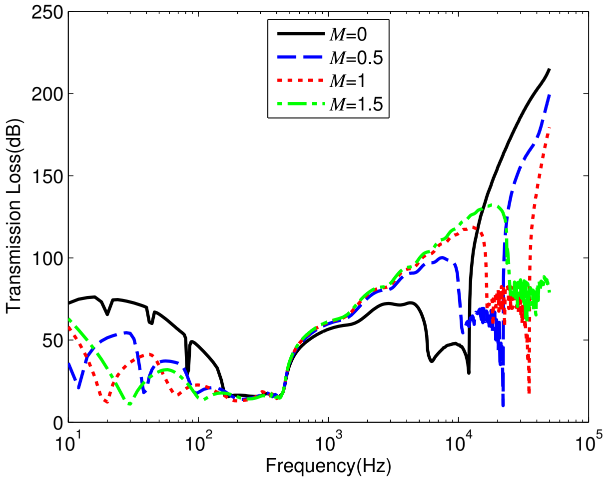

Figure 4.11: The variation of TL with frequency for different Mach numbers (UU). The locations of the dips for f_{cr} and f_{coin} are consistent with the predicted values presented in Table 4.2.

Figure 4.13 shows the TLs of various configurations under no-flow condition with the incidence angle fixed at $\alpha = 45°$. Although the configurations are different, the two main dips appear around the ring frequency f_r and the critical frequency f_{cr}. It is obvious that the BU and the UU configurations provide a better performance of transmission loss than any other configuration does. The transmission loss for the BU and the UU constructions is 20-40 dB higher than other configurations in the low frequency end of the plot. Between the ring frequency f_r and the critical frequency f_{cr}, this is again generally true but the difference in the acoustic performance can be seen to strongly

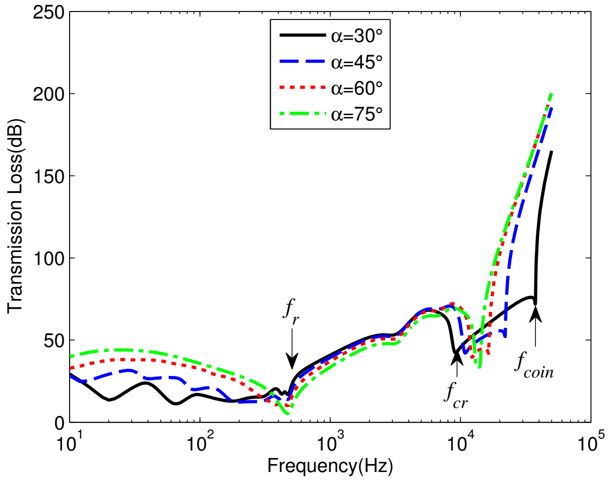

Figure 4.12: The variation of TL with frequency for different incident angles α (BB configuration), $M = 0.5$. $f_r = 509.32$ Hz, $f_{cr} = 9395$ Hz and $f_{coin} = 37579$ Hz have been calculated using Eqs. (4.38), (4.40) and (4.41) for 30°, respectively.

Table 4.3: The variation of the critical frequency and the coincidence frequency vary the Mach number.

Incidence angle	f_{cr} with $M = 0$	f_{cr} with $M = 0.5$	f_{coin} with $M = 0$	f_{coin} with $M = 0.5$
30°	6013 Hz	9395 Hz	24051 Hz	37579 Hz
45°	6013 Hz	11016 Hz	12025 Hz	22032 Hz
60°	6013 Hz	12347 Hz	8017 Hz	16463 Hz
75°	6013 Hz	13223 Hz	6444 Hz	14172 Hz

depend upon the frequency. For the configuration of the double shells without the porous material, the resonances are significant in the mass controlled region (between f_r and f_{cr}). This phenomenon is absent in any other configuration. Similar behaviour has been previously observed for double shells in the absence of porous lining and external flow (Lee et al. [41]). The dips can be reduced by the absorption effect of the porous material, such as the BB, BU and UU configurations. The BB configuration only gives an overall modest performance of transmission loss without multiple dips unlike that of the two shells configuration between f_r and f_{cr}. This is due to the stiffening effect of the directly attached foam lining in the BB configuration.

When the effect of external flow is included in the calculations, the results are presented in Figure 4.14. Below the ring frequency, the BU and the UU configuration still provide an overall superior performance of sound insulation. However, their contribution is not so significant as compared to that of no-flow condition. Above the ring frequency, the

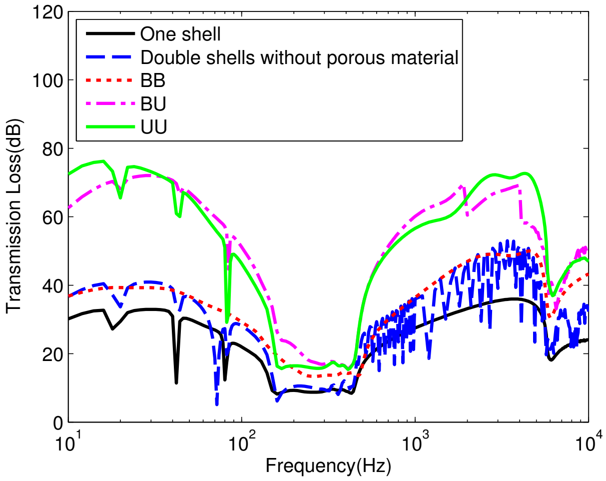

Figure 4.13: The variation of TL with frequency for different configurations at $M = 0$ and $\alpha = 45°$.

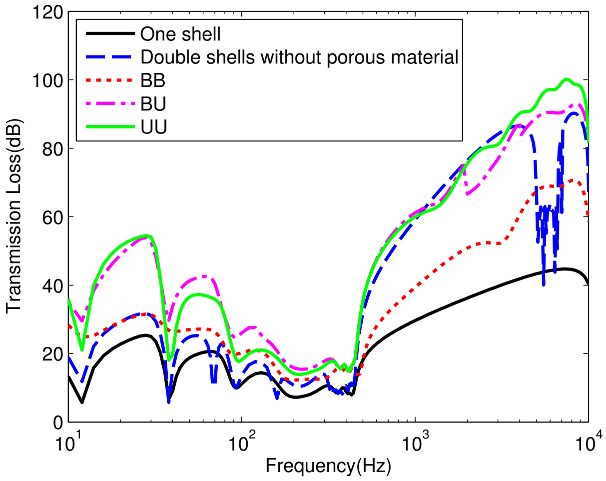

Figure 4.14: The variation of TL with frequency for different configurations at $M = 0.5$ and $\alpha = 45°$.

TL of the two shells configuration without the porous material is similar to that of the BU and the UU configurations. It is noted that there are not many dips occurring above f_r for the case of $M = 0.5$. This can be attributed to the effect of radiation damping provided by the external mean flow [98]. The damping provided by the external mean flow is more dominant than that by the porous material in the mass controlled region.

4.5 Conclusions

In this chapter, an analytical model is developed to calculate the sound transmission through a double shell lined with poroelastic material including the effect of external mean flow. The equivalent fluid method based on Biot's model is used to describe the porous material. The transmission loss for three types of configurations (BB, BU and UU) is calculated as a function of frequency. The effect of the mean flow is brought out. Unlike the flat panel, there exist three main dips in the transmission loss of the cylindrical shell. The transmission loss decreases as the incident angle increases below the ring frequency, but increases between the ring frequency and the critical frequency in all three types of configurations. The critical frequency is independent of the angle of incidence when the incident wave vector has no azimuthal component. The external mean flow causes the TL to decrease with some fluctuations below the ring frequency, but increases above the ring frequency due to the negative stiffness and the damping effect added by the external flow. The flow also shifts the critical frequency and the coincidence frequency to higher values, but has no effect on the ring frequency because the latter is a structural property. The effect of the porous material is significant in absence of external flow, especially for the BU and the UU configurations. However, this effect is not remarkable when there is an external flow. The shells without any porous material can approximately provide the same transmission loss as that of the BU and the UU configuration above the ring frequency. These results suggest that for superior noise insulation, the two shells should be separated by an air gap.

Chapter 5

Double-walled cylindrical shells with turbulent boundary layer excitation

In Chapter 3 and Chapter 4 , sound transmission through a double-walled flat panel and a double-walled cylindrical shell respectively, in the presence of external mean flow, was studied. Mean flow is an idealised case. In real cruise flight conditions, the boundary layer noise is the dominant source of the aircraft cabin noise [46]. Most researchers have focused so far on sound transmission through flat panels [47, 48, 51–56]. These analytical studies based on the plate model neglect the curvature of fuselage or the effect of neighbouring panel or sometimes both. In practice, the aircraft fuselage is not a single wall structure. It is a double wall system which consists of a skin panel and a trim panel with an annular space between them. This is the motivation to study sound transmission through the cylindrical shell structure lined with porous material under the turbulent boundary layer excitation. In addition to the more realistic model for flow involving a turbulent boundary layer, in this chapter, we consider more a realistic structure for many practical application by allowing the length of the double-walled cylindrical shell to be finite.

5.1 Description of the system

A schematic diagram of the configuration of the system under study is shown in Figure 5.1. Consider two concentric finite cylindrical shells with hard end caps of length L and radii R_1 and R_2 for outer and inner shell, respectively. The outer shell is assumed to be excited by a fully developed turbulent boundary layer flow. The fluid medium in the exterior and the interior cavity has the density and the speed of sound as (ρ_e, c_e) and (ρ_i, c_i), respectively. The porous material is lined within the annular space to reduce the interior noise. As in the previous chapters, three configurations of the sandwich construction are considered here. A bonded-bonded (BB) configuration, as shown in Figure 5.1a, is one having both sides of porous material bonded directly to the two shells. A bonded-unbonded (BU) configuration has one side of porous material bonded directly to the outer shell and the second side is separated from the inner shell by an air gap (see Figure 5.1b). An unbonded-unbonded (UU) configuration has both sides of porous material exposed to the air gap and it is not attached to the two shells (Figure 5.1c).

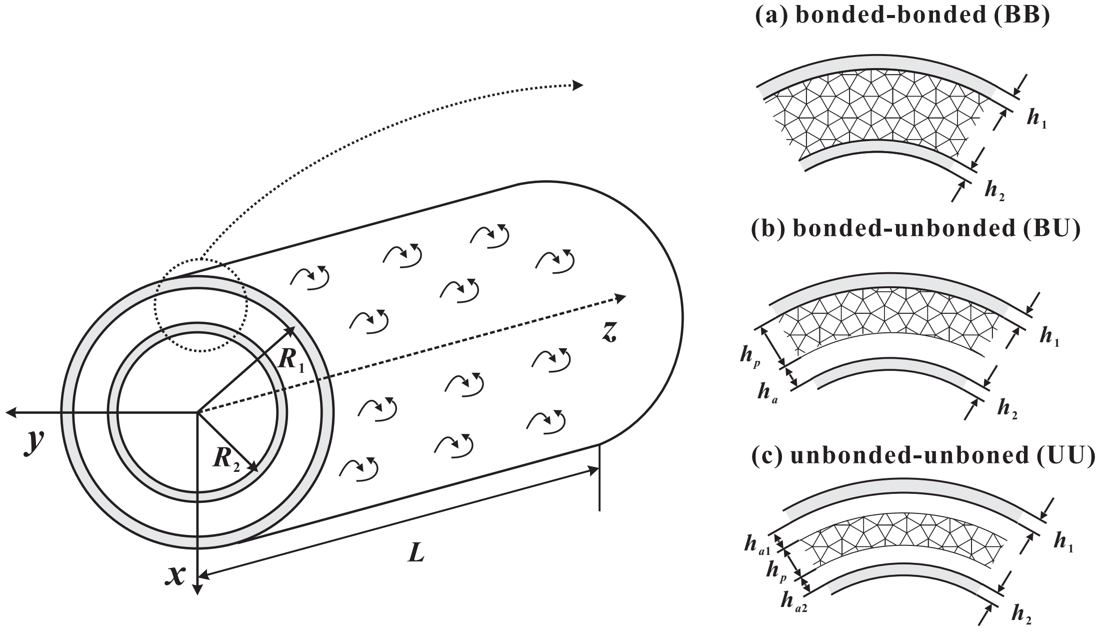

Figure 5.1: A sketch showing the sound wave transmission problem through the double shells system. Different configurations: (a) bonded-bonded (BB); (b) bonded-unbonded (BU); (c) unbonded-unbonded (UU).

The porous material can be modelled as an equivalent fluid by using the wave number of the strongest wave and its corresponding equivalent density based on Biot's model [29] proposed by Lee et al. [81]. This method was introduced in Chapter 3 and Chapter 4. We still continue to use this simplification in the present chapter. The strongest wave in each configuration has been presented in Table 3.5 of Chapter 3. For brevity, the details of this method will not be repeated here.

5.2 Governing equations

Let $\{u_j^0, v_j^0, w_j^0\}$ be the displacement components at the neutral surface of a shell in the axial, circumferential and the radial directions, where the subscript j denotes the variables associated with the outer shell ($j = 1$) and the inner shell ($j = 2$). Love's thin shell theory [93] is used here to describe the motion of the two shells. Taking temporal Fourier transform, the equations of shells motion can be expressed as

$$
\begin{aligned}
L_1\{u_j^0, v_j^0, w_j^0\} + \omega^2 \rho_{sj} h_j u_j &= 0 && (5.1)\\
L_2\{u_j^0, v_j^0, w_j^0\} + \omega^2 \rho_{sj} h_j v_j &= 0 \qquad (j = 1, 2) && (5.2)\\
L_3\{u_j^0, v_j^0, w_j^0\} + \omega^2 \rho_{sj} h_j w_j &= \Delta p_j && (5.3)
\end{aligned}
$$

where ρ_{sj} are h_j are the density and the thickness of the shell, respectively, ω is angular frequency, Δp_j is the pressure difference between the two sides of the shell. L_1, L_2 and L_3 are linear differential operators for the circular cylindrical shell which are presented in the Appendix D.

Figure 5.1a (on the right side of the figure) shows a double shell arrangement lined with porous material in the BB configuration. The space can be divided into three regions: the exterior region where the turbulent boundary layer is present, the annular space fully filled by the porous material and the interior cavity with static air. If we neglect the radiation pressure, the total fluctuating pressure in the external fluid p_1 is only the random fluctuating pressure induced by the TBL. The Fourier transform of the wave equations of the annular space and the cavity leads to the Helmholz equation for both pressure variables

$$\nabla^2 p_2 + k_2^2 p_2 = 0,\ \nabla^2 p_3 + k_3^2 p_3 = 0 \qquad (5.4)$$

where p_2 and p_3 are the pressure in the annular space and the interior cavity, respectively. The complex wavenumber $k_2 = k_{\mathrm{II}}$ presents the wavenumber of the frame wave propagating in the porous material (see Table 3.5). The wavenumber k_3 in the cavity equals ω/c_i.

The pressure term in Eq. (5.3) for outer shell is given by

$$\Delta p_1 = p_2 - p_1, \tag{5.5}$$

and that for the inner shell is given by

$$\Delta p_2 = p_3 - p_2. \tag{5.6}$$

At the interfaces between the elastic shells and the fluids, the following boundary conditions must be satisfied

$$\left.\frac{\partial p_2}{\partial r}\right|_{r=R_1} = \rho_2 \omega^2 w_1 \tag{5.7}$$

$$\left.\frac{\partial p_2}{\partial r}\right|_{r=R_2} = \rho_2 \omega^2 w_2 \tag{5.8}$$

$$\left.\frac{\partial p_2}{\partial r}\right|_{r=R_2} = \rho_i \omega^2 w_2 \tag{5.9}$$

where $\rho_2 = \rho_{11}^*$ is the density of equivalent fluid for the porous material in the BB configuration (see Table 3.5).

The boundary conditions at both ends were assumed to be simply supported which is in line with other researchers [49–51, 56]. Therefore, the boundary conditions for the simply supported shells, at both ends, must be satisfied

$$w_j = \frac{\partial^2 w_j}{\partial z^2} = 0\bigg|_{z=0,L} \qquad (j = 1, 2) \tag{5.10}$$

The gradients of the pressure p_2 and p_3 are zero at both ends (rigid walls)

$$\frac{\partial p_j}{\partial z} = 0\bigg|_{z=0,L} \qquad (j = 2, 3). \tag{5.11}$$

Considering the equations of motion (5.1)-(5.3) and boundary conditions Eq. (5.10), the solutions for the displacement field can be expressed as

$$\begin{aligned} u_j(z,\theta,\omega) &= \sum_{m=1,n=0}^{\infty} u_{jmn}(\omega)\cos\frac{m\pi z}{L}\cos(n\theta) && (5.12)\\ v_j(z,\theta,\omega) &= \sum_{m=1,n=0}^{\infty} v_{jmn}(\omega)\sin\frac{m\pi z}{L}\sin(n\theta) \qquad (j=1,2) && (5.13)\\ w_j(z,\theta,\omega) &= \sum_{m=1,n=0}^{\infty} w_{jmn}(\omega)\sin\frac{m\pi z}{L}\cos(n\theta) && (5.14) \end{aligned}$$

where the modal coefficients u_{jmn}, v_{jmn} and w_{jmn} are unknown.

Similarly, the p_1 can be expanded as

$$p_1 = \sum_{m=1,n=0}^{\infty} p_{1mn}\Psi(z,\theta), \qquad p_{1mn} = \frac{\varepsilon_n}{\pi L}\left[\int_0^L\int_0^{2\pi} p(z,\theta,\omega)\Psi_{mn}(z,\theta)dzd\theta\right] \tag{5.15}$$

where ε_n are Neumann factors, $\varepsilon_n = 1$ for $n = 0$ and $\varepsilon_n = 2$ otherwise. The orthogonal basis functions $\Psi_{mn}(z,\theta) = \sin\frac{m\pi z}{L}\cos(n\theta)$.

The pressures p_2 and p_3 are also expanded in terms of the orthogonal basis as

$$\begin{aligned} p_2 &= \sum_{m=1,n=0}^{\infty}\left[p_{21mn}J_n(k_{2rm}r) + p_{22mn}Y_n(k_{2rm}r)\right]\Psi_{mn}(z,\theta) && (5.16)\\ p_3 &= \sum_{m=1,n=0}^{\infty} p_{3mn}J_n(k_{3rm}r)\Psi_{mn}(z,\theta) && (5.17) \end{aligned}$$

where J_n and Y_n are the first and second kinds of Bessel functions of order n, respectively. $k_{2rm}^2 = k_2^2 - (m\pi/L)^2$ and $k_{3rm}^2 = k_3^2 - (m\pi/L)^2$, p_{21mn}, p_{22mn} and p_{3mn} are unknown model coefficients.

Substituting the Eqs. (5.12)-(5.17) into the field equations (5.1)-(5.3) and the boundary conditions (5.7)-(5.9), we can obtain the unknown modal coefficients vector $\mathbf{x} = \{p_{21mn}, p_{22mn}, p_{3mn}, u_{1mn}, v_{1mn}, w_{1mn}, u_{2mn}, v_{2mn}, w_{2mn}\}$ as

$$\mathbf{x} = \mathbf{H} p_{1mn} \tag{5.18}$$

where $\mathbf{H} = \{H_{p21mn}, H_{p22mn}, H_{p3mn}, H_{u1mn}, H_{v1mn}, H_{w1mn}, H_{u2mn}, H_{v2mn}, H_{w2mn}\}$ is a vector of frequency response functions due to the modal excitation p_{1mn} of the turbulent boundary layer.

Note the modal basis functions for the pressure p_2 and p_3, Eqs. (5.16) and (5.17), do not satisfy the boundary conditions Eq. (5.11). Therefore, the orthogonal functions $\Psi_{mn}(z, \theta)$ in Eqs. (5.16) and (5.17) should be expanded as [49, 50]

$$\Psi_{mn}(z, \theta) = \sum_{j=0, j \neq m}^{\infty} \frac{\varepsilon_j}{\pi} \frac{m[1 - (-1)^{m-j}]}{m^2 - j^2} \varphi_{mn}(z, \theta) \tag{5.19}$$

where the orthogonal functions $\varphi_{mn}(z, \theta) = \cos(j\pi z/L)\cos(n\theta)$ of p_2 and p_3 now satisfy the boundary conditions Eq. (5.11). The relevant unknown model coefficients of the BU and UU configurations can be obtained in a similar manner. Details of the expressions relevant for these two configurations are given in the Appendix H and Appendix I, respectively.

The analysis of the sound radiation to the interior often directly depends on the flexural response of the inner shell. The total flexural kinetic energy gives an indicator of the spatially averaged vibration and also of the near field sound radiation [57]. The power spectral density of the total kinetic energy can be written as

$$S_{EK} = \frac{1}{2} \int_0^L \int_0^{2\pi} \rho_{s2} h_2 R_2 \lim_{T \to \infty} E\left[\frac{1}{T} \dot{w}_2^*(z, \theta, \omega) \dot{w}_2(z, \theta, \omega)\right] dz d\theta \tag{5.20}$$

where $\dot{w}_2 = i\omega w_2$ is the velocity of the inner shell. The superscript * indicates the complex conjugate; T is a suitable period of time; E denotes the expectation operator. Substituting the modal expression for the flexural displacement of Eq. (5.14) and Eq. (5.18) into Eq. (5.20) and considering the orthogonality conditions, Eq. (5.20) can be rewritten as

$$S_{EK} = \frac{M}{2} \sum_{m=1,n=0}^{\infty} |H_{w2mn}|^2 S_{pmn} \tag{5.21}$$

where $M = \int_0^L \int_0^2 \rho_{s2} h_2 \Psi_{mn}^2(z,\theta) dz d\theta$ is the modal mass of the inner shell. The modal power spectral density S_{pmn} of TBL is defined as

$$\begin{aligned} S_{pmn} &= \Phi_p(\omega) \left(\frac{\varepsilon_n}{\pi L}\right)^2 \int_0^L dz_1 \int_0^L dz_2 \int_0^{2\pi} d\theta_1 \int_0^{2\pi} d\theta_2 S_p(\xi,\eta,\omega) \\ & \sin\frac{m\pi z_1}{L} \sin\frac{m\pi z_2}{L} \cos(n\theta_1)\cos(n\theta_2) \end{aligned} \tag{5.22}$$

where S_p represents the cross spectral density of the pressure fluctuations due to the TBL, which will be presented later.

5.3 The model of pressure fluctuation due to TBL

If the boundary layer is fully turbulent and the pressure field over the outer surface is characterized as temporally stationary with spatially homogeneous statistics, the pressure field can be expressed by a cross correlation function that decays with spatial and time separation [99, 100]. The cross spectral density induced by a TBL can be expressed as

$$S_p(\xi,\eta,\omega) = \Phi_p(\omega) \exp(-\alpha|\xi|) \exp(-\beta|\eta|) \exp(i\omega\xi/U_c), \tag{5.23}$$

where the separation $\xi = z_1 - z_2$ and $\eta = R(\theta_1 - \theta_2)$. U_c denotes the convection velocity. The quantities α and β will be defined based on Corcos [99] and Efimtsov [100] model which are frequently used in the literature. $\Phi_p(\omega)$ is the autospectrum of the wall pressure, which is given by [56]

$$\frac{\Phi_p(\omega)U_\infty}{q^2\delta^*} = \begin{cases} 2.14 \times 10^{-5}, & \omega\delta^*/U_\infty \le 0.25 \\ 7.56 \times 10^{-6} \times (\omega\delta^*/U_\infty)^{-3/4}, & 0.25 < \omega\delta^*/U_\infty \le 0.35 \\ 1.27 \times 10^{-4} \times (\omega\delta^*/U_\infty)^{-3}, & 3.5 < \omega\delta^*/U_\infty \end{cases} \tag{5.24}$$

where the boundary layer displacement thickness $\delta^* = \delta/8$ (δ is the boundary layer thickness). The dynamic pressure is given by $q = \rho_0 U_\infty^2/2$ with ρ_0 the density of the fluid and U_∞ the free stream velocity.

In the Corcos model [99], the coefficients α and β are

$$\alpha = \alpha_c \omega/U_c, \qquad \beta = \beta_c \omega/U_c \tag{5.25}$$

where α_c and β_c are constant parameters determined by the experimental results. In general, the range of the values is $\alpha_c = 0.11$ to 0.12 and $\beta_c = 0.7$ to 1.2 for a smooth rigid wall. However, the Corcos model neglects the boundary layer thickness. This drawback in the Corcos model was addressed by the Efimtsov model [100], in which the coefficients α and β are

$$\alpha = 1/\alpha_e, \qquad \beta = 1/\beta_e. \tag{5.26}$$

In Eq. (5.26), α_e and β_e are given by

$$\alpha_e = \delta \left[\left(\frac{0.1\mathrm{Sh}}{U_c/U_\tau} \right)^2 + \frac{5300}{\mathrm{Sh}^2 + 2235} \right]^{-(1/2)} \tag{5.27a}$$

$$\beta_e = \delta \left[\left(\frac{0.77\mathrm{Sh}}{U_c/U_\tau} \right)^2 + \frac{300304}{\mathrm{Sh}^2 + 1648} \right]^{-(1/2)} \tag{5.27b}$$

where the Strouhal number $\mathrm{Sh} = \omega \delta U_\tau$. $U_\tau = 0.03 U_\infty$ is the friction velocity. The effect of the boundary layer thickness is considered in the Efimtsov model. It is suitable for a wide range of Mach number in the range 0.41 to 2.1 [56].

Besides the two models mentioned above, several other models have been proposed (as reviewed by Miller [101], Graham [102] and Hwang [103]). The purpose of this study is not to select the best model of the turbulent boundary layer, but to establish a better understanding of the sound transmission through the sandwich shells in the presence of the turbulent boundary layer excitation. As the choice of the turbulent boundary layer model cannot affect the analysis process of the sound transmission problem, the two popular models, (Corcos model and Efimtsov model which have been used by many other researchers for predicting the sound transmission through panel under TBL excitation [47–56]) will be used in our analysis.

5.4 Results and discussions

The two shells are made of aluminum. All the geometry and material properties used in our calculation are listed in Table 5.1. The dimension of shell chosen here is the same as that used by Tang et al. [50], which is close to the fuselage dimension of the AIRBUS A320 family [104]. The properties of the polyimide foams are obtained from the work of Silcox et al. [18], which is listed in Table 5.2. The parameters of the structure and the porous material are chosen from Table 5.1 and the Foam 1 in Table 5.2 unless stated otherwise, respectively. The structural loss factor is modeled as a small imaginary part of both Young's modulus $E_s(1+i\eta_s)$ in the calculation. The aircraft is assumed to cruise at an altitude of 35,000 ft ($\rho_e = 0.3795$ kg/m^3, $c_e = 296.556$ m/s) and is pressured at 10,000 ft ($\rho_i = 0.9041$ kg/m^3, $c_i = 328.558$ m/s). In the numerical calculations, the convection velocity U_c equals $0.7U_\infty$ with the freestream velocity $U_\infty = 225$ m/s. The U_τ is assumed as $0.03U_\infty$. The boundary layer thickness δ is taken as 0.06 m. In Corcos model, we choose the parameters α_c and β_c as 0.1 and 0.77, respectively.

Table 5.1: Parameters of the physical system.

Shell properties	Description	Value
E_s	Young's modulus	70 GPa
ρ_s	Density	2700 kg/m^3
ν_s	Poisson's ratio	0.33
η_s	Loss factor	0.01
h_1	Thickness	2 mm
h_2	Thickness	2 mm
R_1	Radius	1.88 m
R_2	Radius	1.84 m
L	Length	30 m
Configuration	BU	UU
Dimension in the annular space	$h_p = 30$ mm $h_a = 10$ mm	$h_p = 30$ mm $h_{a1} = 5$ mm $h_{a2} = 5$ mm

The solutions of the displacement of the shells and the pressures are presented in the form of a double series. Therefore, a sufficiently large number of terms must be considered

Table 5.2: Biot parameters for polyimide foams [18].

	Foam 1 9.6 kg/m^3 compressed to 10% of original thickness	Foam 2 5.4 kg/m^3 compressed to 50% of original thickness	Foam 3 5.4 kg/m^3 compressed to 20% of original thickness
Density (kg/m^3)	9.6	5.4	5.4
Flow resistivity (MKS Rayls/m)	29000	40000	10000
Porosity	0.99	0.99	0.99
Tortuosity	3.11	2.11	1.02
Viscous characteristic length (10^{-6} m)	66.9	44.0	38.2
Thermal characteristic length (10^{-6} m)	268	51.1	59.1
Young's modulus (kPa)	135	76	27
Loss factor	0.42	0.21	0.0034
Poisson's ratio	0.21	0.012	0.46

to ensure the convergence of the solutions. If the solution is convergent at the highest frequency of interest, it is also convergent for all frequencies lower than that. The highest frequency for our interest is selected as 10000 Hz. Figure 5.2 shows the convergence trend of inner shell kinetic energy for different configurations of the sandwich with the increase of mode number m. Note that the truncation of modes in the summations in section 5.2 requires both m and n to be finite. To simplify the convergence study, we have taken $m = n$ so that a trend such as that in Figure 5.2 is with respect to a single parameter describing the number of terms included. The trend indicates that more than 300 modes should be adequate for convergence at 10000 Hz. Therefore, 300 modes are used in the rest of this chapter.

5.4.1 Comparison between Corcos model and Efimtsov model

By using the Corcos model, Figure 5.3 shows the power spectral density (PSD) for the inner shell kinetic energy of different configurations. The curves have a plateau before they decay with 16 dB/Octave. All the curves have a turning point at the same frequency about 440 Hz. This frequency is attributed to the inner shell resonance. The natural frequencies of the shell can be predicted by [57] and given by

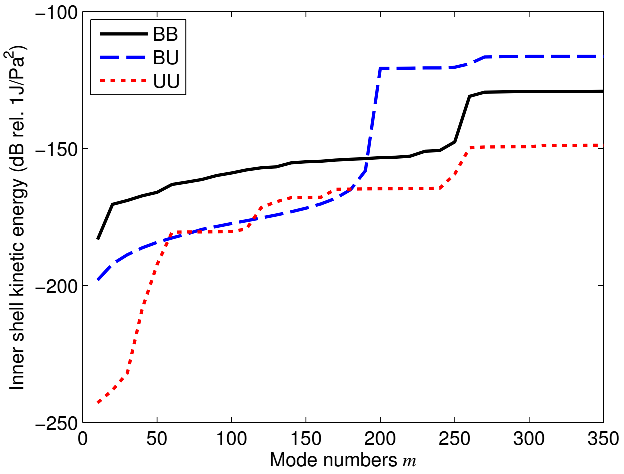

Figure 5.2: Mode convergence diagram for different configurations at 10000 Hz.

$$f_{sh} = \frac{1}{2\pi}\sqrt{\frac{E_s}{\rho_s R_2^2}}\sqrt{\frac{(m\pi R_2/L)^4}{[(m\pi R_2/L)^2+n^2]^2}+\frac{(h_2/R_2)^2}{12(1-\nu_s^2)}\left[\left(\frac{m\pi R_2}{L}\right)^2+n^2\right]}. \tag{5.28}$$

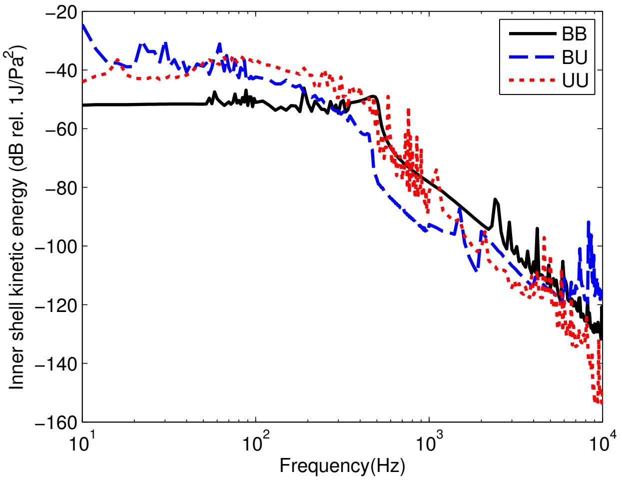

Figure 5.3: PSD prediction of inner shell kinetic energy of different configurations by Corcos model.

As $h_2 << R_2$ or L, and we select the range of m or n, Eq. (5.28) can be simplified by ignoring the second term above as

$$f_{sh} = \frac{1}{2\pi}\sqrt{\frac{E_s}{\rho_s R_2^2}}\sqrt{\frac{(m\pi R_2/L)^4}{[(m\pi R_2/L)^2+n^2]^2}}. \tag{5.29}$$

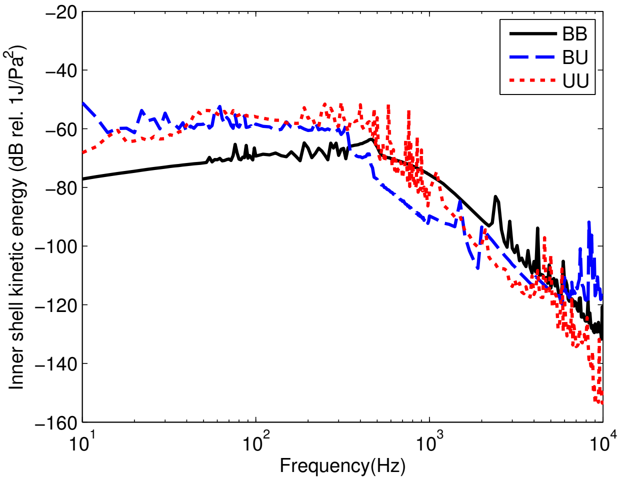

Figure 5.4: PSD prediction of inner shell kinetic energy of different configurations by Efimtsov model.

The maximum value of f_{sh} is $(1/2\pi R_2)\sqrt{E_s/\rho_s} = 440.42$ Hz, when $n = 0$. This value is same as the ring frequency $(1/2\pi R_2)\sqrt{E_s/\rho_s}$. Therefore, the frequency of the turning point is the ring frequency. Since the ring frequency is the maximum value of the shell natural frequency based on the chosen mode number m, the peaks due to the inner shell resonance only occur below the ring frequency. Some of the other peaks are due to the hydrodynamic coincidence at the frequencies given by [50]

$$f_{hy} = \frac{1}{2\pi}\frac{U_c m\pi}{L}. \tag{5.30}$$

At the hydrodynamic coincidence frequencies, the bending wave speed of the inner shell equals the convection velocity of the flow. The maximum value of the hydrodynamic coincidence frequencies is calculated as 787.5 Hz for the parameters used here. Therefore, hydrodynamic coincidence only controls the frequency range which is below 787.5 Hz. The acoustic coincidence resonances at which the bending wave speed of the inner shell associated with an infinite plate with the same material and thickness equals the acoustic wave speed of the fluid results in the remaining peaks [50]. Since the maximum value of the resonance frequencies of the inner shell and the hydrodynamic coincidence frequencies is below 800 Hz, the peaks in high frequency range are only because of the acoustic coincidence.

By comparing the three curves in Figure 5.3, we note that the BU and UU configurations provide less inner shell kinetic energy than the BB configuration does above the ring frequency. People have different hearing sensitivity to different frequencies of sound. The ear is most sensitive for the frequency range from 500-5000 Hz [89]. Therefore, the BU configuration appears to be most suitable for this frequency range control when the main concern is noise annoyance. For controlling the vibration of the inner shell over 5000 Hz, the UU configuration seems to be the right choice. However, below the ring frequency, the PSD of the kinetic energy in the BB configuration is smaller, about 10 dB less than that of the BU and UU configurations. This is because below the ring frequency, the dynamics of the shell are dominated by the membrane stiffness of the shell. It is obvious that the BB configuration is stiffer than the other two configurations.

Figure 5.4 shows the kinetic energy of the inner shell while using the Efimtsov model. In comparison with the results based on the Corcos model (see Figure 5.3), Efimtsov model predicts the kinetic energy 10-20 dB lower in the frequency range below the ring frequency. A similar phenomenon is also observed in the references [50, 56]. When the frequency is over 2000 Hz, the values predicted by the Efimtsov model are same as those predicted by the Corcos model. The reason is that the exponential coefficients α and β of the Efimtsov model is consistent with those of the Corcos model at higher frequencies. It can be shown by substituting the parameters in Eq. (5.26) that over 2000 Hz, the exponential coefficients α and β of the Efimtsov model correspond to those of the Corcos model. Since the key features presented by these two models are the same, the following analysis will only be based on the Corcos model.

5.4.2 The effect of the airgap

Due to the air gap in the BU and UU configurations, only these two configurations are considered in this subsection. Figure 5.5 shows the variation of the inner shell kinetic energy of BU configuration with different air gap thickness h_a. Following the decrease of the air gap thickness h_a, the inner shell kinetic energy will decrease in most of the frequency range, especially for higher frequencies. Over 2000 Hz, there are two main peaks in the curves for $h_a = 80\%(R_1 - R_2)$, $60\%(R_1 - R_2)$ and $40\%(R_1 - R_2)$. As explained earlier, these peaks are caused by the acoustic coincidence. However, the first peak disappears in the curves of $h_a = 20\%(R_1 - R_2)$ and $10\%(R_1 - R_2)$. Therefore, the first peak is produced by the acoustic coincidence between the inner shell and the annular space, while the second peak is generated by the acoustic coincidence between the inner shell and the inner cavity. The large volume of the porous material can diminish the first peak. When the thickness of the air gap approaches zero, the curve will be same as that of the BB configuration (see Figure 5.3). Comparing between Figure 5.3 and Figure 5.5, we note that the air gap is very important for reducing the noise in the higher frequency range. This phenomenon is also observed when a plane wave transmits through the sandwich structures, as shown in Chapter 3 and Chapter 4.

Maury et al. [51] neglected the frame wave transmission within the fiberglass material. The result of the BU configuration in their study with a thin air gap (15% of the cavity depth which was the region between two face plates) was the same as that of the BB configuration. Their result is not reasonable for the BB configuration. Allard and Atalla [62] have pointed out that the limp model of the porous material is valid when the thin light foam is decoupled with an air gap from a vibrating system. The current model has overcome the drawback of the work of Maury et al. [51].

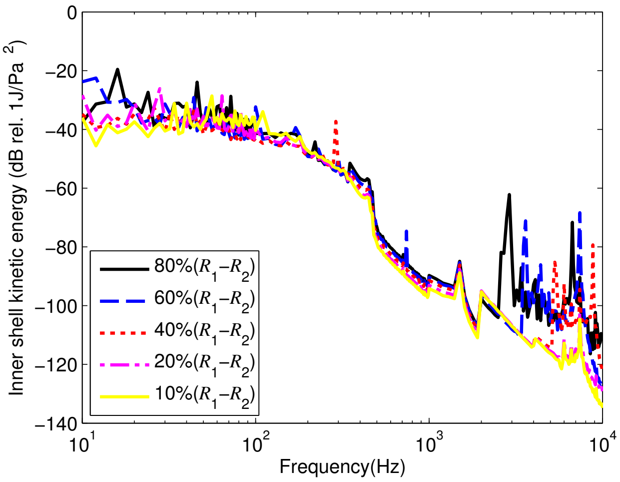

Figure 5.5: PSD of inner shell kinetic energy of BU configuration with different air gap depths.

When the thickness of the porous material h_p, labeled in Figure 5.1, in the UU configuration is fixed at 20 cm, the variation of the inner shell kinetic energy with the two air gaps is shown in Figure 5.6. In Figure 5.7, the change of the inner shell kinetic energy for the different thickness of the two air gaps with $h_p = 30$ cm is shown. From Figure 5.6 and Figure 5.7, it is clear that the unsymmetric structure ($h_{a1} = 5$ mm, $h_{a2} = 15$ mm and $h_{a1} = 15$ mm, $h_{a2} = 5$ mm in Figure 5.6; $h_{a1} = 2.5$ mm, $h_{a2} = 7.5$ mm and

$h_{a1} = 7.5$ mm, $h_{a2} = 2.5$ mm in Figure 5.7) provides a better insulation than the symmetric structure ($h_{a1} = 10$ mm and $h_{a2} = 10$ mm in Figure 5.6; $h_{a1} = 5$ mm and $h_{a2} = 5$ mm in Figure 5.7) does below the ring frequency in both cases, $h_p = 20$ cm and 30 cm. The peaks around 5000 Hz are also suppressed severely by the unsymmetric structure. However, this phenomenon is more obvious in the case of $h_p = 20$ cm than that of the case of $h_p = 30$ cm. Thicker porous material $h_p = 30$ cm could provide better insulation than the thinner one $h_p = 20$ cm does in the UU configuration as shown in Figure 5.6 and Figure 5.7. For the thicker porous material case (Figure 5.7), the symmetric structure shows performance similar to that of the unsymmetric structure in the frequency range above the ring frequency. The reason is that in the higher frequency range, the cavity resonance results the peaks as mentioned above. When $h_p = 30$ cm, the dimension of the air gap is too small compared with the thickness of the porous material. Therefore, the peaks vary little with the change of the two air gaps depths.

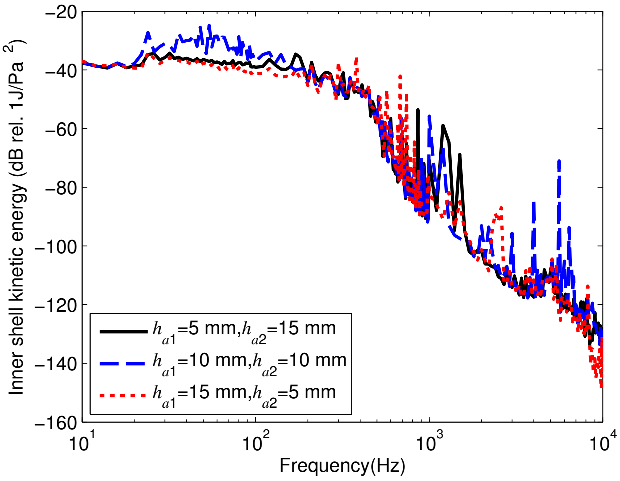

Figure 5.6: PSD of inner shell kinetic energy of UU configuration with different air gap depths, when $h_p = 20$ cm.

5.4.3 The effect of the parameters of the porous material

In this subsection, the effect of the parameters of the porous material is discussed. Silcox et al. [18] compressed a number of polyimide foams in the rise direction to a specified % of their original thickness, and then allowed them to recover. The relation between the parameters of the foams and the compression were obtained by experiment. However, the Biot's parameters for only three polyimide foams (compressed to 10%, 50% and 20% of their original thickness for Foam 1, Foam 2 and Foam 3, respectively) were given by

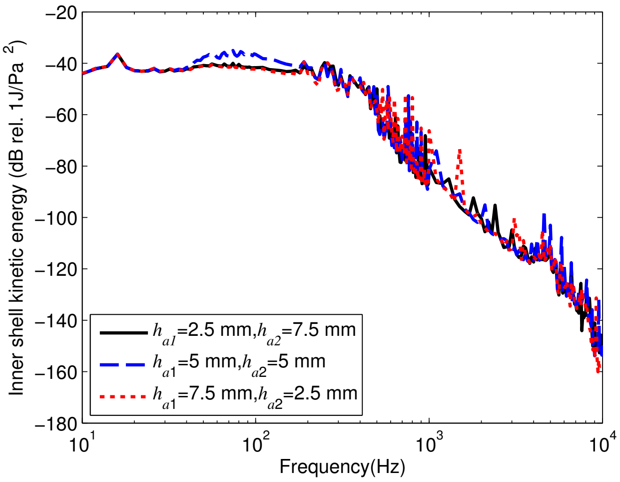

Figure 5.7: PSD of inner shell kinetic energy of UU configuration with different air gap depths, when $h_p = 30$ cm.

Silcox et al. [18], which are shown in Table 5.2. Therefore, the parameters of these three foams are used in the following analysis. Figures 5.8 to 5.10 show the PSD of inner shell kinetic energy for these three foams in different configurations, respectively.

Foam 3 outperforms the other two foams by 6 to 8 dB on PSD of the inner shell kinetic energy at frequencies less than the ring frequency in the BB configuration. However, it only shows such higher values above the ring frequency in the BU and UU configurations. Below the ring frequency, the stiffness effects of the cylindrical shell are large. Foam 1 and Foam 2 are stiffer than Foam 3 due to their relatively higher Young's modulus (see Table 5.2) which is related to the solid phase of the foam. Since in the BB configuration, the frame wave is the dominant wave in the porous material [81], it is obvious, seeing the Figure 5.8, that Foam 1 and Foam 2 provide a better insulation than Foam 3 does below the ring frequency. However, in the frequency range below the ring frequency, the most important wave in the porous material is the airborne wave in the BU and UU configurations. Therefore, this phenomenon is not remarkable in the BU and UU configurations at the frequencies less than the ring frequency, shown as Figure 5.9 and Figure 5.10.

As discussing in previous, above the ring frequency, the peaks are mainly contributed by the acoustic coincidence. The PSD of the inner shell kinetic energy is more sensitive to changes of parameters related to the fluid in the annular space. However, the dominant wave in the porous material for the BB configuration is the frame wave. The variation of flow resistance, the parameter related to the fluid phase in the porous material, will not obviously change the value of the PSD of the inner shell kinetic energy above the ring frequency, as Figure 5.8 shown. In the BU configuration, the airborne wave in the porous material controls the frequency range below 2000 Hz. Therefore, it can be clearly seen in Figure 5.9 that Foam 2 with the highest flow resistance among these three foams provides a superior sound insulation in the frequency range from the ring frequency to 2000 Hz. Above 4000 Hz, this phenomenon is not obvious for the BU configuration, since the frame wave is the dominant wave. The airborne wave is the dominant wave in the UU configuration. This results that Foam 3 outperforms the other two foams on PSD of the inner shell kinetic energy at frequencies higher than the the ring frequency in the UU configuration (see Figure 5.10). By comparing Figures 5.8 to 5.10, Foam 2 with small density provides a superior sound insulation due to its high flow resistance. The study of Silcox et al. [18] showed that the more the material was compressed, the lower the modulus and the flow resistance. Therefore, one may not want to compress the foam for obtaining a better sound insulation. However, Silcox et al. [18] pointed out that the original polyimide foam was found to have a flow resistivity that was too high for conventional acoustic applications. Since the Biot's parameters of only three foams were given by Silcox et al. [18], the more cases need to be verified.

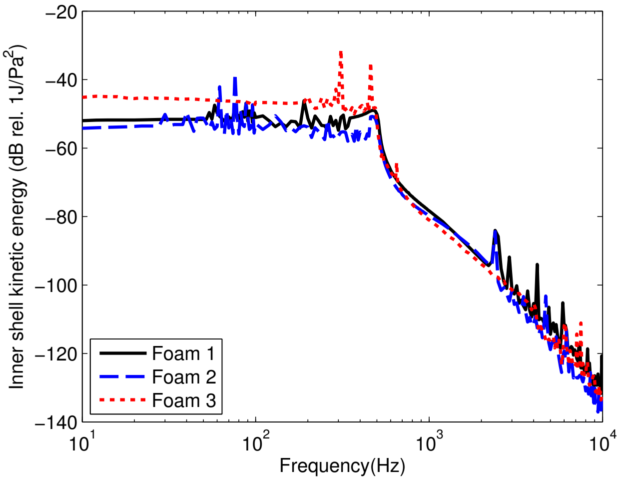

Figure 5.8: PSD of inner shell kinetic energy of BB configuration with different porous material. The Biot's parameters of these three foams are obtain from the work of Silcox et al. [18] and listed in Table 5.2

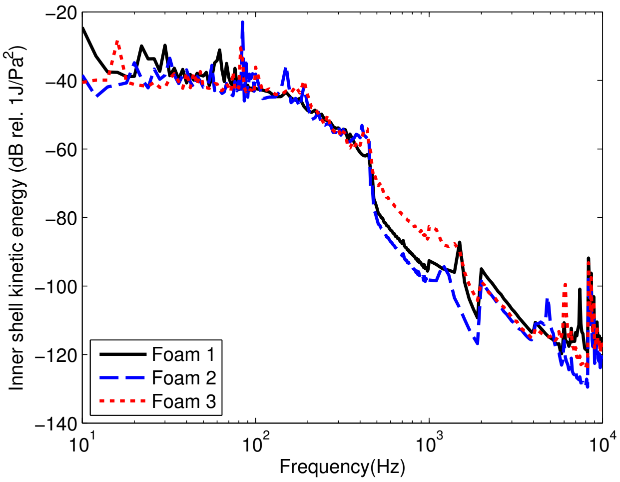

Figure 5.9: PSD of inner shell kinetic energy of BU configuration with different porous material. The Biot's parameters of these three foams are obtain from the work of Silcox et al. [18] and listed in Table 5.2

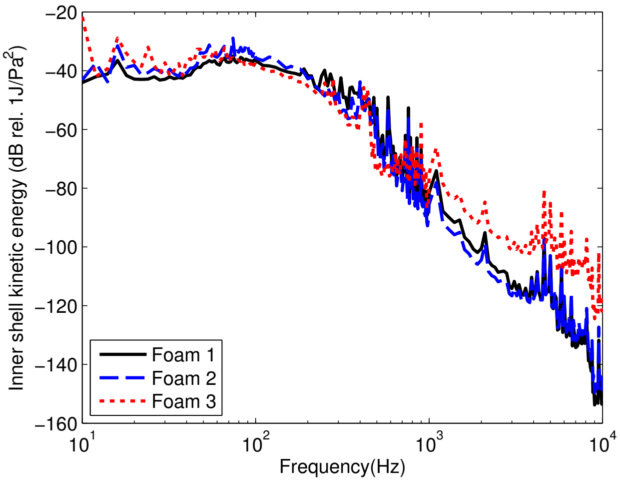

Figure 5.10: PSD of inner shell kinetic energy of UU configuration with different porous material. The Biot's parameters of these three foams are obtain from the work of Silcox et al. [18] and listed in Table 5.2

5.5 Conclusions

In this study, an analytical model is developed to calculate the sound transmission through a double shell lined with poroelastic material under the exterior turbulent boundary layer excitation. The axial length of the shell is kept finite. The equivalent fluid method based on Biot's model is used to describe the porous material. The power spectrum of the inner shell kinetic energy, an indicator of the spatially averaged vibration and also of the near field sound radiation, is calculated for the three types of configurations (BB, BU and UU) as a function of frequency. The modal expansion method is used to express the displacements of the shells and the sound pressures in each region. The effects of the air gap and the parameters of the porous material are brought out. The following general conclusions can be drawn:

i. All the PSD curves have a turning point at the ring frequency, because the thickness of the shell is far smaller than the radius of the shell. The peaks due to the contributions of the modes of the shell only occur below the ring frequency. Other peaks in the curves are caused by the hydrodynamic coincidence and the acoustic coincidence.

ii. The values of PSD predicted by the Efimtsov are the same as that predicted by the Corcos model at high frequency (here over 2000 Hz). This is because the exponential coefficients α and β of the Efimtsov model is consistent with those of the Corcos model at higher frequencies.

iii. Reducing the thickness of the air gap can decrease the PSD of inner shell kinetic energy in most of the frequency range for the BU and UU configurations. The air gap is very important for reduce the noise in higher frequency range, even if it is very thin. In the UU configuration, the unsymmetric structure can improve the sound insulation in comparison with the symmetric structure.

iv. The small density foam with high flow resistance, compared to the large density foam with relatively small flow resistance, can still provide a satisfactory and even superior sound insulation. Since only three foams given by Silcox et al. [18] are considered here, the more porous material needs to be considered. This phenomenon should be further validated by experiment.

Chapter 6

Conclusions and future work

Conclusions

A theoretical model for predicting sound transmission through plates or shells lined with porous material in the presence of external flow is studied. This study incorporates the effect of flow on one side of the panels when sound is transmitted through them. In the simplest case the convected effects of the flow are incorporated using a mean flow model. Varous idealised geometries of the panel and the internal structure of the sandwich are considered. Finally, a relatively more realistic model of a finite cylinder excited by a turbulent boundary layer is studied.

Biot's model is used to describe the sound propagation in the porous material. Three types of constructions, bonded-bonded, bonded-unbonded and unbonded-unbonded, are considered. The acoustic performance of the sandwich panel for different configurations is presented. The effect of external flow on sound transmission is brought out.

In the flat panel model, the transmission loss of three types of configurations is calculated as a function of frequency in a diffuse sound field. The external mean flow increases the sound transmission loss with increase in flow velocity, because the external mean flow results the increase of the impedance of the panel. The critical frequency in the curve of transmission loss only depends on the properties of the plates. However, the fundamental resonance frequency is directly related to other geometric and material parameters. Due to the stiffening effect of the directly attached foam lining in the BB configuration, the fundamental resonance frequency is higher than that without the porous material. When considering the pressure effect, transmission loss increases gradually when the pressure difference between air gap and that in the exterior decreases. This effect is mainly attributed to the mismatch in the characteristic impedances of the exterior and the interior. Since the BB configuration provides more stiffness in the air gap between two face plates due to the mechanical bonding of the layers, the BU and UU configuration offers a relatively superior performance of sound insulation in most of the frequency range. The air gap plays a very important role in sound insulation.

In practice, considering the severe weight and space constraints imposed on airplane soundproofing treatments, the emphasis in many cases has been on minimizing the weight and depth of the treatment while maintaining adequate sound attenuation characteristics. A bi-optimization is carried out with the objectives of simultaneously minimizing the sound transmission and the structural weight of the flat double-walled panel. Below the critical point identified on the Pareto-front, the acoustic performance cannot be improved further and the transmission loss increases at the expense of increasing the weight. If over the limiting value, the transmission loss will decrease.

The effect of laminated composite face plates is also studied. Like the trend in the isotropic plates, the external mean flow yields 3-6 dB comparing with no flow condition in composite sandwich structure. This phenomenon is more obvious in the case of symmetric cross-ply. The stacking of many ply groups reduces the orthotropy and the laminate becomes quasi-homogeneous, which results in the value of the dip at the critical frequency going down. If the thickness of the laminated composite face plate is fixed, the stacking sequence cannot change the transmission loss in the mass-controlled region, the transmission loss in the coincidence controlled region can be altered. This effect is more sensitive for the case of symmetric cross-ply laminates.

Sound transmission through double cylindrical shells lined with porous material in the presence of external mean flow is studied next. The transmission characteristics of the sandwich construction are presented for different incidence angles and Mach numbers over a wide frequency range. The in-plane vibration is coupled with the transverse vibration for cylindrical shells structures. This results in the transmission loss exhibiting three dips on the frequency axis, at the ring frequency, the critical frequency and the coincidence frequency. In contrast, there are only two such frequencies for flat panels. In the stiffness controlled region (i.e. below the ring frequency), the external flow decreases the sound transmission loss. However, the external flow provides a modest increase in transmission loss in the mass law region between the ring frequency and the critical frequency. The external flow also shifts the critical frequency and the coincidence frequency up, but has no effect on the ring frequency because it depends on the structural parameters alone. The effect of the porous material is significant in the absence of external flow, especially for the BU and the UU configurations. However, this effect is not remarkable when there is an external flow. Like plat panels, the results suggest that the two shells should be separated by an air gap for superior noise insulation.

The turbulent boundary layer becomes the most important noise source for the interior cabin noise at high Mach numbers. Therefore, the model of sound transmission through double-walled cylindrical shell lined with poroelastic material in the core excited by the exterior pressure fluctuation due to the turbulent boundary layer is finally developed. The power spectral density of the inner shell kinetic energy, an indicator of the spatially averaged vibration and also of the near field sound radiation is calculated as a function of frequency for three types of configurations (BB, BU and UU). The peaks of the power spectral density curve are due to the resonance frequencies of the coupled system, the hydrodynamic coincidence and the acoustic coincidence. Peaks due to the modes of the shell occur below the ring frequency. The air gap is found to be very important for reducing the noise in higher frequency range, even if it is very thin. Reducing the thickness of the air gap can cause the decrease of the power spectrum density of inner shell kinetic energy in the most frequency range in the BU and UU configurations.

In the preliminary design of aircraft, there are numerous factors that need to be considered. Interior noise is one such factor. This current research gives several clues into how interior noise can be reduced. The external mean flow can increase the sound transmission loss of the fuselage, even in the condition where there is no porous material lining between the fuselage skin and trim panel (see Figure 4.14). However, in the flight condition, this possible choice to neglect the porous material is only based on the acoustic characteristic of the sound transmission through the fuselage. From another aircraft design point of view, for example thermal insulation, the porous material should be included. If the ground test state is considered, the results obtained from static air on the incidence side of the panel has been shown to provide a conservative estimate of sound insulation of sandwich panels. If the flight condition is considered, some characteristic frequencies are dependent on the flow. This should be kept in mind for preliminary designs. Since the human ear is most sensitive in the frequency range 500-5000 Hz. There should be an air gap between the two face walls for superior sound insulation, e.g. BU or UU configuration. However, the BU configuration is easier than the UU configuration to implement in practice. This is the reason why this configuration is widely used in the aircraft industry. The choice of the model of sound propagation in the porous material is crucial for analysing the sound transmission through a sandwich structure. For example, the equivalent fluid model based on Biot's model used here overcomes the limitation of the study of Maury et al. [51] who used the empirical model for investigating the sound transmission through sandwich panels. It should be noted that the conclusions here are obtained from a detailed study into the acoustic characteristics. However, aircraft fuselage design is a very complex process. The acoustic characteristic of the fuselage is only one of many design factors. In order to satisfy the design criteria of an aircraft, all the design factors should be considered. The conclusions from the analysis of one performance parameter, e.g. acoustic characteristics, may not be still valid in other performance analyses. Therefore, a multi-disciplinary design approach is required.

Future work

The fuselage, in practice, is a stiffened structure. In order to improve the double-wall structure sound transmission predictions, the modelling of stiffened panels is essential. Koval [105, 106] developed a theoretical model to analyse the influence of ring frames and stringers on sound transmission through cylindrical shells. By treating the stiffeners as discrete elements, Koval improved the smeared-stiffener theory formulated by Rosen and Singer, because smeared-stiffener the one was only valid at low frequencies. Lee et al. [107] studied sound transmission through circular cylindrical shell stiffened by periodically deployed stiffeners by using the space harmonic expansion method developed by Mead et al. [108]. In this respect, the application of periodic structures theory could provide novel insight. Later, Efimtsov et al. [109] also used the space harmonic expansion method to investigate the sound pressure in cylindrical shells with stiffeners excited by the random field of wall pressure fluctuations of the turbulent boundary layer. Liu et al. [110] used the receptance method and modal expansion technique to evaluate the airborne sound insulation of curved panels with a stringer and frame attachments. However, the problem of sound transmission through the stiffened structures lined with porous material under different excitation fields seems to have not been addressed. This certainty is an area that needs attention in the future.

The inner shell, trim panel of the fuselage, is not of a simple regular cylindrical shape, but includes an internal floor partition. The internal floor will change the response of the inner shell and the interior sound pressure. Fuller [111] suggested a simplified model to study the effect of the floor on the sound transmission inside an infinite thin cylindrical shell coupled to a cylindrical shaped cavity. The floor was modelled by a series of periodic forces evaluated by a zero radial shell displacement condition. Missaoui et al. [112] studied the vibroacoustic character of a shell-floor-cavity system by using the artificial springer technique and the integro-modal approach which are the two methods they previously established. One of these two methods respectively proposed by Fuller and Missaoui can be involved in current models to give a more accurate interior noise prediction for a real aircraft.

The model of porous material as an equivalent continuum also presents new opportunities for research. Invariably, these apparent properties need to be measured in the laboratory. Recent advances in the area of modelling of foams and porous material for elastic response could be extended for the vibroacoustics of such medium.

Appendix A

Matrix formulation of the flat panel system in the BB configuration

In order to satisfy the boundary conditions on the panel, the trace wavelengths must match on the panel, giving

$$k_{1x} = k_{1p}\cos\theta = k_x = k_{2p}\cos\theta = k_{tx} \tag{A.1}$$

$$k_{1y} = k_{1p}\sin\theta = k_y = k_{2p}\cos\theta = k_{tx} \tag{A.2}$$

$$\tag{A.3}$$

So the following expressions can be obtained

$$w_1 = W_1 e^{i\omega t - i(k_{1x}x + k_{1y}y)} \tag{A.4}$$

$$w_2 = W_2 e^{i\omega t - i(k_{1x}x + k_{1y}y)} \tag{A.5}$$

$$u_{1s} = U_{1s} e^{i\omega t - i(k_{1x}x + k_{1y}y)} \tag{A.6}$$

$$v_{1s} = V_{1s} e^{i\omega t - i(k_{1x}x + k_{1y}y)} \tag{A.7}$$

$$u_{2s} = U_{2s} e^{i\omega t - i(k_{1x}x + k_{1y}y)} \tag{A.8}$$

$$v_{2s} = V_{2s} e^{i\omega t - i(k_{1x}x + k_{1y}y)} \tag{A.9}$$

$$p_t = P_t e^{i\omega t - i(k_{1x}x + k_{1y}y + k_{tz}z)} \tag{A.10}$$

The following boundary conditions must be satisfied in the BB configuration.

At $z = 0$:

(1). $\frac{D^2 w_1}{Dt^2} = \left(\frac{\partial}{\partial t} + V \cdot \frac{\partial}{\partial x}\right)^2 = -\frac{1}{\rho_i}\frac{\partial p_1}{\partial z}$

(2). $u_z = w_1$

(3). $U_z = w_1$

(4). $u_x = u_{1s} - \frac{h_1}{2}\frac{\partial w_1}{\partial x}$

(5). $u_y = v_{1s} - \frac{h_1}{2}\frac{\partial w_1}{\partial y}$

(6). $\left[D_{1s}\left(k_{1x}^2 + \frac{1-\nu_1}{2}k_{1y}^2\right) - \omega^2 m_{1s}\right] u_{1s} + D_{1s}\frac{1+\nu_1}{2}k_{1x}k_{1y}v_{1s} = \tau_{xz}$

(7). $[D_1(k_{1x}^2 + k_{1y}^2)^2 - \omega^2 m_{1s}]w_1 = p_1 + \sigma_z + \sigma_f - i\left(k_x\frac{h}{2}\tau_{xz} + k_y\frac{h}{2}\tau_{yz}\right)$

At $z = H$:

(8). $\frac{D^2 w_2}{Dt^2} = \frac{\partial^2 w_2}{\partial t^2} = -\frac{1}{\rho_2}\frac{\partial p_t}{\partial z}$

(9). $u_z = w_2$

(10). $U_z = w_2$

(11). $u_x = u_{2s} - \frac{h_2}{2}\frac{\partial w_2}{\partial x}$

(12). $u_y = v_{2s} - \frac{h_2}{2}\frac{\partial w_2}{\partial y}$

(13). $\left[D_{2s}\left(k_{1x}^2 + \frac{1-\nu_2}{2}k_{1y}^2\right) - \omega^2 m_{2s}\right] u_{2s} + D_{2s}\frac{1+\nu_2}{2}k_{1x}k_{1y}v_{2s} = \tau_{xz}$

(14). $[D_2(k_{1x}^2 + k_{1y}^2)^2 - \omega^2 m_{2s}]w_2 = -p_t - \sigma_z - \sigma_f - i\left(k_{1x}\frac{h_2}{2}\tau_{xz} + k_{1y}\frac{h_2}{2}\tau_{yz}\right)$

Then substituting the appropriate expressions into these boundary conditions and rearranging the resulting equations into matrix form, the following linear equations can be obtained

$$[\mathrm{A}]\{\mathrm{C}\} = \{\mathrm{B}\} \tag{A.11}$$

where [A] is a 14 × 14 coefficient matrix, {C} is a 14 × 1 vector of unknown amplitudes, $\{\mathrm{C}\}^{\mathrm{T}} = \{C_1\ C_2\ C_3\ C_4\ C_5\ C_6\ W_1\ W_2\ U_{1s}\ V_{1s}\ U_{2s}\ V_{2s}\ P_r\ P_t\}$. {B} is the 14 × 1 forcing vector.

Appendix B

Matrix formulation of the flat panel system in the BU configuration

Similar as the BB configuration, the trace wavelengths should match on the panel, giving

$$k_{1x} = k_{1p}\cos\theta = k_x = k_{2x} = k_{2p}\cos\theta = k_{tx} \tag{B.1}$$

$$k_{1y} = k_{1p}\sin\theta = k_y = k_{2y} = k_{2p}\cos\theta = k_{tx} \tag{B.2}$$

$$\tag{B.3}$$

So the following expressions can be written as

$$w_1 = W_1 e^{i\omega t - i(k_{1x}x + k_{1y}y)} \tag{B.4}$$

$$w_2 = W_2 e^{i\omega t - i(k_{1x}x + k_{1y}y)} \tag{B.5}$$

$$u_{1s} = U_{1s} e^{i\omega t - i(k_{1x}x + k_{1y}y)} \tag{B.6}$$

$$v_{1s} = V_{1s} e^{i\omega t - i(k_{1x}x + k_{1y}y)} \tag{B.7}$$

$$p_{2i} = P_{2i} e^{i\omega t - i(k_{1x}x + k_{1y}y + k_{2z}z)} \tag{B.8}$$

$$p_{2r} = P_{2r} e^{i\omega t - i(k_{1x}x + k_{1y}y - k_{2z}z)} \tag{B.9}$$

$$p_t = P_t e^{i\omega t - i(k_{1x}x + k_{1y}y + k_{tz}z)} \tag{B.10}$$

The following boundary conditions must be satisfied in the BU configuration.

At $z = 0$:

(1). $\frac{D^2 w_1}{Dt^2} = \left(\frac{\partial}{\partial t} + V \cdot \frac{\partial}{\partial x}\right)^2 = -\frac{1}{\rho_i}\frac{\partial p_1}{\partial z}$

(2). $u_z = w_1$

(3). $U_z = w_1$

(4). $u_x = u_{1s} - \frac{h_1}{2}\frac{\partial w_1}{\partial x}$

(5). $u_y = v_{1s} - \frac{h_1}{2}\frac{\partial w_1}{\partial y}$

(6). $\left[D_{1s}\left(k_{1x}^2 + \frac{1-\nu_1}{2}k_{1y}^2\right) - \omega^2 m_{1s}\right] u_{1s} + D_{1s}\frac{1+\nu_1}{2}k_{1x}k_{1y}v_{1s} = \tau_{xz}$

(7). $[D_1(k_{1x}^2 + k_{1y}^2)^2 - \omega^2 m_{1s}]w_1 = p_1 + \sigma_z + \sigma_f - i\left(k_x\frac{h}{2}\tau_{xz} + k_y\frac{h}{2}\tau_{yz}\right)$

At $z = H$:

(8). $-\beta p_2 = \sigma_f$

(9). $-(1-\beta)p_2 = \sigma_z$

(10). $(1-\beta)\frac{D^2 u_Z}{Dt^2} + \beta\frac{D^2 U_z}{Dt^2} = -\frac{1}{\rho_2}\frac{\partial p_2}{\partial z}$

(11). $\tau_{xz} = 0$

At $z = H + l$:

(12). $\frac{D^2 w_2}{Dt^2} = \frac{\partial^2 w_2}{\partial t^2} = -\frac{1}{\rho_2}\frac{\partial p_2}{\partial z}$

(13). $\frac{D^2 w_2}{Dt^2} = \frac{\partial^2 w_2}{\partial t^2} = -\frac{1}{\rho_3}\frac{\partial p_t}{\partial z}$

(14). $[D_2(k_{1x}^2 + k_{1y}^2)^2 - \omega^2 m_{2s}]w_2 = p_2 - p_t$

Then substituting the appropriate expressions into these boundary conditions and rearranging the resulting equations into matrix form, the following linear equations can be obtained

$$[\mathrm{A}]\{\mathrm{C}\} = \{\mathrm{B}\} \tag{B.11}$$

where [A] is a 14×14 coefficient matrix, {C} is a 14×1 vector of unknown amplitudes, $\{\mathrm{C}\}^{\mathrm{T}} = \{C_1\ C_2\ C_3\ C_4\ C_5\ C_6\ W_1\ W_2\ U_{1s}\ V_{1s}\ P_r\ P_{2i}\ P_{2r} P_t\}$. {B} is the 14×1 forcing vector.

Appendix C

Matrix formulation of the flat panel system in the UU configuration

Similar as the previous configurations, the trace wavelengths should match on the panel, giving

$$k_{1x} = k_{1p}\cos\theta = k_x = k_{2x} = k_{3x} = k_{2p}\cos\theta = k_{tx} \tag{C.1}$$

$$k_{1y} = k_{1p}\sin\theta = k_y = k_{2y} = k_{3y} = k_{2p}\cos\theta = k_{tx} \tag{C.2}$$

$$\tag{C.3}$$

So the following expressions can be written as

$$w_1 = W_1 e^{i\omega t - i(k_{1x}x + k_{1y}y)} \tag{C.4}$$

$$w_2 = W_2 e^{i\omega t - i(k_{1x}x + k_{1y}y)} \tag{C.5}$$

$$p_{2i} = P_{2i} e^{i\omega t - i(k_{1x}x + k_{1y}y + k_{2z}z)} \tag{C.6}$$

$$p_{2r} = P_{2r} e^{i\omega t - i(k_{1x}x + k_{1y}y - k_{2z}z)} \tag{C.7}$$

$$p_{3i} = P_{3i} e^{i\omega t - i(k_{1x}x + k_{1y}y + k_{3z}z)} \tag{C.8}$$

$$p_{3r} = P_{3r} e^{i\omega t - i(k_{1x}x + k_{1y}y - k_{3z}z)} \tag{C.9}$$

$$p_t = P_t e^{i\omega t - i(k_{1x}x + k_{1y}y + k_{tz}z)} \tag{C.10}$$

The following boundary conditions must be satisfied in the UU configuration.

At $z = 0$:

(1). $\frac{D^2 w_1}{Dt^2} = \left(\frac{\partial}{\partial t} + V \cdot \frac{\partial}{\partial x}\right)^2 = -\frac{1}{\rho_i}\frac{\partial p_1}{\partial z}$

(2). $\frac{D^2 w_1}{Dt^2} = \frac{\partial^2 w_1}{\partial t^2} = -\frac{1}{\rho_2}\frac{\partial p_2}{\partial z}$

(3). $[D_1(k_{1x}^2 + k_{1y}^2)^2 - \omega^2 m_{1s}]w_1 = p_1 - p_2$

At $z = l_1$:

(4). $-\beta p_2 = \sigma_f$

(5). $-(1-\beta)p_2 = \sigma_z$

(6). $(1-\beta)\frac{D^2 u_Z}{Dt^2} + \beta\frac{D^2 U_z}{Dt^2} = -\frac{1}{\rho_2}\frac{\partial p_2}{\partial z}$

(7). $\tau_{xz} = 0$

At $z = l_1 + H$:

(8). $-\beta p_3 = \sigma_f$

(9). $-(1-\beta)p_3 = \sigma_z$

(10). $(1-\beta)\frac{D^2 u_Z}{Dt^2} + \beta\frac{D^2 U_z}{Dt^2} = -\frac{1}{\rho_3}\frac{\partial p_3}{\partial z}$

(11). $\tau_{xz} = 0$

At $z = l_1 + H + l_2$:

(12). $\frac{D^2 w_2}{Dt^2} = \frac{\partial^2 w_2}{\partial t^2} = -\frac{1}{\rho_3}\frac{\partial p_2}{\partial z}$

(13). $\frac{D^2 w_2}{Dt^2} = \frac{\partial^2 w_2}{\partial t^2} = -\frac{1}{\rho_4}\frac{\partial p_t}{\partial z}$

(14). $[D_2(k_{1x}^2 + k_{1y}^2)^2 - \omega^2 m_{2s}]w_2 = p_3 - p_t$

Then substituting the appropriate expressions into these boundary conditions and rearranging the resulting equations into matrix form, the following linear equations can be obtained

$$[\mathrm{A}]\{\mathrm{C}\} = \{\mathrm{B}\} \tag{C.11}$$

where [A] is a 14 × 14 coefficient matrix, {C} is a 14 × 1 vector of unknown amplitudes, $\{\mathrm{C}\}^{\mathrm{T}} = \{C_1\ C_2\ C_3\ C_4\ C_5\ C_6\ W_1\ W_2\ P_r\ P_{2i}\ P_{2r}\ P_{3i}\ P_{3r}\ P_t\}$. {B} is the 14 × 1 forcing vector.

Appendix D

Love's equations

Love's equation for the circular cylindrical shell:

$$L_1\{u_j^0, v_j^0, w_j^0\} = \rho_{sj} h_j \ddot{u}_j^0 \tag{D.1}$$

$$L_2\{u_j^0, v_j^0, w_j^0\} = \rho_{sj} h_j \ddot{v}_j^0 \tag{D.2}$$

$$L_3\{u_j^0, v_j^0, w_j^0\} + \Delta p_j = \rho_{sj} h_j \ddot{w}_j^0 \tag{D.3}$$

Differential Operators in above equations are expressed as

$$\begin{aligned} L_1\{u_j^0, v_j^0, w_j^0\} \;=\;& K_j \frac{\partial^2 u_j^0}{\partial z^2} + \frac{K_j(1+\mu_j)}{2R_j} \frac{\partial^2 v_j^0}{\partial z \partial \theta} \\ & + \frac{K_j(1-\mu_j)}{2R_j^2} \frac{\partial^2 u_j^0}{\partial \theta^2} + \frac{K_j \mu_j}{R_j} \frac{\partial w_j^0}{\partial z} \end{aligned} \tag{D.4}$$

$$\begin{aligned} L_2\{u_j^0, v_j^0, w_j^0\} \;=\;& \frac{K_j(1-\mu_j)}{2} \left(\frac{1}{R_j} \frac{\partial^2 u_j^0}{\partial z \partial \theta} + \frac{\partial^2 v_j^0}{\partial z^2} \right) \\ & + \frac{K_j}{R_j} \left(\mu_j \frac{\partial^2 u_j^0}{\partial z \partial \theta} + \frac{1}{R_j} \frac{\partial^2 v_j^0}{\partial \theta^2} + \frac{1}{R_j} \frac{\partial w_j^0}{\partial \theta} \right) \\ & + \frac{D_j(1-\mu_j)}{2R_j^2} \left(\frac{\partial^2 v_j^0}{\partial z^2} - 2 \frac{\partial^3 w_j^0}{\partial z^2 \partial \theta} \right) \\ & + \frac{D_j}{R_j^2} \left(\frac{1}{R_j^2} \frac{\partial^2 v_j^0}{\partial \theta^2} - \frac{1}{R_j^2} \frac{\partial^3 w_j^0}{\partial \theta^3} - \mu_j \frac{\partial^3 w_j^0}{\partial z^2 \partial \theta} \right) \end{aligned} \tag{D.5}$$

$$
\begin{aligned}
L_3\{u_j^0, v_j^0, w_j^0\} \quad = \quad & D_j \left[-\frac{\partial^4 w_j^0}{\partial z^4} + \frac{\mu_j}{R_j^2} \left(\frac{\partial^3 v_j^0}{\partial z^2 \partial \theta} - \frac{\partial^4 w_j^0}{\partial z^2 \partial \theta^2} \right) \right] \\
& + \frac{D_j(1-\mu_j)}{R_j^2} \left(\frac{\partial^3 v_j^0}{\partial z^2 \partial \theta} - 2 \frac{\partial^4 w_j^0}{\partial z^2 \partial \theta^2} \right) \\
& + \frac{D_j}{R_j^2} \left(\frac{1}{R_j^2} \frac{\partial^3 v_j^0}{\partial \theta^3} - \frac{1}{R_j^2} \frac{\partial^4 w_j^0}{\partial \theta^4} - \mu_j \frac{\partial^4 w_j^0}{\partial z^2 \partial \theta^2} \right) \\
& - \frac{K_j}{R_j} \left(\mu_j \frac{\partial u_j^0}{\partial z} + \frac{1}{R_j} \frac{\partial v_j^0}{\partial \theta} + \frac{w_j^0}{R_j} \right)
\end{aligned}
\qquad (D.6)
$$

where R_j is the radius of the shell. E_j, μ_j, $K_j = \frac{E_j h_j}{1-\mu_j^2}$ and $D_j = \frac{E_j h_j^3}{12(1-\mu_j^2)}$ are the Young's modulus and Poisson's ratio, membrane and bending stiffness of the shell, respectively.

Appendix E

BB configuration in the cylindrical shell system

The terms within Eq. (4.27) are expressed as

$A = \rho_{s1} h_1 \omega^2 - K_1 k_{1z}^2 - \frac{K_1(1-\mu_1)n^2}{2R_1^2}$, $B = -\frac{iK_1 k_{1z} n(1+\mu_1)}{2R_1}$, $C = -\frac{iK_1 \mu_1 k_{1z}}{R_1}$

$D = \frac{iK_1 k_{1z} n(1+\mu_1)}{2R_1}$, $E = \rho_{s1} h_1 \omega^2 - \frac{K_1 k_{1z}^2 (1-\mu_1)}{2} - \frac{K_1 n^2}{R_1^2} - \frac{D_1 k_{1z}^2 (1-\mu_1)}{2R_1^2} - \frac{D_1 n^2}{R_1^4}$

$F = -\frac{K_1 n}{R_1^2} - \frac{D_1 k_{1z}^2 n}{R_1^2} - \frac{D_1 n^3}{R_1^4}$, $G = H_n^2(k_{1r} R_1)$, $H = -H_n^1(k_{2r} R_1)$

$I = -H_n^2(k_{2r} R_1)$, $J = \frac{iK_1 \mu_1 k_{1z}}{R_1}$, $K = -\frac{D_1 k_{1z}^2 n}{R_1^2} - \frac{D_1 n^3}{R_1^4} - \frac{K_1 n}{R_1^2}$

$L = \rho_{s1} h_1 \omega^2 - D_1 k_{1z}^4 - \frac{2D_1 k_{1z}^2 n^2}{R_1^2} - \frac{D_1 n^4}{R_1^4} - \frac{K_1}{R_1^2}$

$M = k_{1r} H_n^{2\prime}(k_{1r} R_1)$, $N = -\rho_i(\omega - V k_{1z})^2$

$O = k_{2r} H_n^{1\prime}(k_{2r} R_1)$, $P = k_{2r} H_n^{2\prime}(k_{2r} R_1)$, $Q = -\rho_2 \omega^2$

$R = \rho_{s2} h_2 \omega^2 - K_2 k_{1z}^2 - \frac{K_2(1-\mu_2)n^2}{2R_2^2}$, $S = -\frac{iK_2 k_{1z} n(1+\mu_2)}{2R_2}$, $T = -\frac{iK_2 \mu_2 k_{1z}}{R_2}$

$U = \frac{iK_2 k_{1z} n(1+\mu_2)}{2R_2}$, $V = \rho_{s2} h_2 \omega^2 - \frac{K_2 k_{1z}^2 (1-\mu_2)}{2} - \frac{K_2 n^2}{R_2^2} - \frac{D_2 k_{1z}^2 (1-\mu_2)}{2R_2^2} - \frac{D_2 n^2}{R_2^4}$

$W = -\frac{K_2 n}{R_2^2} - \frac{D_2 k_{1z}^2 n}{R_2^2} - \frac{D_2 n^3}{R_2^4}$

$X = H_n^1(k_{2r} R_2)$, $Y = H_n^2(k_{2r} R_2)$, $Z = -H_n^1(k_{3r} R_2)$

$A1 = \frac{iK_2 \mu_1 k_{1z}}{R_2}$, $B1 = -\frac{K_2 n}{R_2^2} - \frac{D_2 k_{1z}^2 n}{R_2^2} - \frac{D_2 n^3}{R_2^4}$

$C1 = \rho_{s2} h_2 \omega^2 - D_2 k_{1z}^4 - \frac{2D_2 k_{1z}^2 n^2}{R_2^2} - \frac{D_2 n^4}{R_2^4} - \frac{K_2}{R_2^2}$

$D1 = k_{2r} H_n^{1\prime}(k_{2r} R_2)$, $E1 = k_{2r} H_n^{2\prime}(k_{2r} R_2)$, $F1 = -\rho_2 \omega^2$

$G1 = k_{3r} H_n^{1\prime}(k_{3r} R_2)$, $H1 = -\rho_t \omega^2$

$I1 = -p_0 \varepsilon_n (-i)^n J_n(k_{1r} R_1)$, $J1 = -p_0 \varepsilon_n (-i)^n k_{1r} J_n'(k_{1r} R_1)$

Appendix F

Matrix formulation of the cylindrical shell system in the BU configuration

Figure 4.1b shows that the double shells lined with porous in the BU configuration. It consists of incident region, porous material region, air gap and transmitted region. The fluid medium in the air gap region has physical property (ρ_3, c_3). $\rho_2 = \rho_{22}^*$ is treated as the equivalent density of porous material layer in low frequency range, while $\rho_2 = \rho_{11}^*$ in high frequency range. The pressure in each region can be expressed as

$$p_1^R(r,\theta,z,t) = \sum_{n=0}^{\infty} p_{1n}^R H_n^2(k_{1r}r) \cos n\theta e^{i(\omega t - k_{1z}z)} \tag{F.1}$$

$$p_2^T(r,\theta,z,t) = \sum_{n=0}^{\infty} p_{2n}^T H_n^1(k_{1r}r) \cos n\theta e^{i(\omega t - k_{1z}z)} \tag{F.2}$$

$$p_2^R(r,\theta,z,t) = \sum_{n=0}^{\infty} p_{2n}^R H_n^2(k_{1r}r) \cos n\theta e^{i(\omega t - k_{1z}z)} \tag{F.3}$$

$$p_3^T(r,\theta,z,t) = \sum_{n=0}^{\infty} p_{3n}^T H_n^1(k_{1r}r) \cos n\theta e^{i(\omega t - k_{1z}z)} \tag{F.4}$$

$$p_3^R(r,\theta,z,t) = \sum_{n=0}^{\infty} p_{3n}^R H_n^2(k_{1r}r) \cos n\theta e^{i(\omega t - k_{1z}z)} \tag{F.5}$$

$$p_4^T(r,\theta,z,t) = \sum_{n=0}^{\infty} p_{4n}^T H_n^1(k_{1r}r) \cos n\theta e^{i(\omega t - k_{1z}z)} \tag{F.6}$$

The wave numbers in Eqs.(F.1)-(F.6) are defined as

$$k_1 = \frac{\omega}{c_i}\frac{1}{1+M\sin(\alpha)},\ k_{1r} = k_1\cos\alpha,\ k_{1z} = k_1\sin\alpha. \tag{F.7}$$

$$k_{2z} = k_{1z},$$

$$\text{in low frequency range:} k_{2r} = \sqrt{k_{\mathrm{I}}^2 - k_{2z}^2}, \tag{F.8}$$

$$\text{in high frequency range:} k_{2r} = \sqrt{k_{\mathrm{II}}^2 - k_{2z}^2}$$

$$k_3 = \frac{\omega}{c_3},\ k_{3z} = k_{1z},\ k_{3r} = \sqrt{k_3^2 - k_{3z}^2}. \tag{F.9}$$

$$k_4 = \frac{\omega}{c_t},\ k_{4z} = k_{1z},\ k_{4r} = \sqrt{k_4^2 - k_{4z}^2}. \tag{F.10}$$

The governing equations for the two shells are

$$L_1\{u_1^0, v_1^0, w_1^0\} = \rho_{s1}h_1\ddot{u}_1^0 \tag{F.11}$$

$$L_2\{u_1^0, v_1^0, w_1^0\} = \rho_{s1}h_1\ddot{v}_1^0 \tag{F.12}$$

$$L_3\{u_1^0, v_1^0, w_1^0\} + [(p_1^I + p_1^R) - (p_2^T + p_2^R)] = \rho_{s1}h_1\ddot{w}_1^0 \tag{F.13}$$

$$L_1\{u_2^0, v_2^0, w_2^0\} = \rho_{s2}h_2\ddot{u}_2^0 \tag{F.14}$$

$$L_2\{u_2^0, v_2^0, w_2^0\} = \rho_{s2}h_2\ddot{v}_2^0 \tag{F.15}$$

$$L_3\{u_2^0, v_2^0, w_2^0\} + [(p_3^T + p_3^R) - p_4^T] = \rho_{s2}h_2\ddot{w}_2^0 \tag{F.16}$$

Boundary conditions:

$$\frac{\partial(p_1^I + p_1^R)}{\partial r} = -\rho_i\left(\frac{\partial}{\partial t} + \mathbf{V}\cdot\nabla\right)^2 w_1^0\Bigg|_{r=R_1} \tag{F.17}$$

$$\frac{\partial(p_2^T + p_2^R)}{\partial r} = -\rho_2\frac{\partial^2 w_1^0}{\partial t^2}\Bigg|_{r=R_1} \tag{F.18}$$

$$p_2^T + p_2^R = p_3^T + p_3^R|_{r=R_p} \tag{F.19}$$

$$v_2^T + v_2^R = v_3^T + v_3^R|_{r=R_p} \tag{F.20}$$

$$\frac{\partial(p_3^T + p_3^R)}{\partial r} = -\rho_3\frac{\partial^2 w_2^0}{\partial t^2}\Bigg|_{r=R_2} \tag{F.21}$$

$$\frac{\partial p_4^T}{\partial r} = -\rho_t\frac{\partial^2 w_2^0}{\partial t^2}\Bigg|_{r=R_2} \tag{F.22}$$

where R_p is the radius of the interface between porous material layer and air gap. v_2^T, v_2^R, v_3^T and v_3^R are the particle velocities in the acoustic space.

These twelve equations can be put into a matrix form as

$$\begin{bmatrix} 0 & 0 & 0 & 0 & 0 & 0 & A & B & C & 0 & 0 & 0 \\ 0 & 0 & 0 & 0 & 0 & 0 & D & E & F & 0 & 0 & 0 \\ G & H & I & 0 & 0 & 0 & J & K & L & 0 & 0 & 0 \\ M & 0 & 0 & 0 & 0 & 0 & 0 & 0 & N & 0 & 0 & 0 \\ 0 & O & P & 0 & 0 & 0 & 0 & 0 & Q & 0 & 0 & 0 \\ 0 & R & S & T & U & 0 & 0 & 0 & 0 & 0 & 0 & 0 \\ 0 & V & W & X & Y & 0 & 0 & 0 & 0 & 0 & 0 & 0 \\ 0 & 0 & 0 & 0 & 0 & 0 & 0 & 0 & Z & A1 & B1 \\ 0 & 0 & 0 & 0 & 0 & 0 & 0 & 0 & C1 & D1 & E1 \\ 0 & 0 & 0 & F1 & G1 & H1 & 0 & 0 & 0 & I1 & J1 & K1 \\ 0 & 0 & 0 & L1 & M1 & 0 & 0 & 0 & 0 & 0 & 0 & N1 \\ 0 & 0 & 0 & 0 & 0 & O1 & 0 & 0 & 0 & 0 & 0 & P1 \end{bmatrix} \left\{ \begin{matrix} p_{1n}^R \\ p_{2n}^T \\ p_{2n}^R \\ p_{3n}^T \\ p_{3n}^R \\ p_{4n}^T \\ u_{1n}^0 \\ v_{1n}^0 \\ w_{1n}^0 \\ u_{2n}^0 \\ v_{2n}^0 \\ w_{2n}^0 \end{matrix} \right\} = \left\{ \begin{matrix} 0 \\ 0 \\ Q1 \\ R1 \\ 0 \\ 0 \\ 0 \\ 0 \\ 0 \\ 0 \\ 0 \\ 0 \end{matrix} \right\} \tag{F.23}$$

where

$A = \rho_{s1} h_1 \omega^2 - K_1 k_{1z}^2 - \frac{K_1(1-\mu_1)n^2}{2R_1^2}$, $B = -\frac{iK_1 k_{1z} n(1+\mu_1)}{2R_1}$, $C = -\frac{iK_1 \mu_1 k_{1z}}{R_1}$

$D = \frac{iK_1 k_{1z} n(1+\mu_1)}{2R_1}$, $E = \rho_{s1} h_1 \omega^2 - \frac{K_1 k_{1z}^2 (1-\mu_1)}{2} - \frac{K_1 n^2}{R_1^2} - \frac{D_1 k_{1z}^2 (1-\mu_1)}{2R_1^2} - \frac{D_1 n^2}{R_1^4}$

$F = -\frac{K_1 n}{R_1^2} - \frac{D_1 k_{1z}^2 n}{R_1^2} - \frac{D_1 n^3}{R_1^4}$, $G = H_n^2(k_{1r} R_1)$, $H = -H_n^1(k_{2r} R_1)$

$I = -H_n^2(k_{2r} R_1)$, $J = \frac{iK_1 \mu_1 k_{1z}}{R_1}$, $K = -\frac{D_1 k_{1z}^2 n}{R_1^2} - \frac{D_1 n^3}{R_1^4} - \frac{K_1 n}{R_1^2}$

$L = \rho_{s1} h_1 \omega^2 - D_1 k_{1z}^4 - \frac{2D_1 k_{1z}^2 n^2}{R_1^2} - \frac{D_1 n^4}{R_1^4} - \frac{K_1}{R_1^2}$

$M = k_{1r} H_n^{2\prime}(k_{1r} R_1)$, $N = -\rho_i (\omega - V k_{1z})^2$

$O = k_{2r} H_n^{1\prime}(k_{2r} R_1)$, $P = k_{2r} H_n^{2\prime}(k_{2r} R_1)$, $Q = -\rho_2 \omega^2$

$R = H_n^1(k_{2r} R_p)$, $S = H_n^2(k_{2r} R_p)$, $T = -H_n^1(k_{3r} R_p)$, $U = -H_n^2(k_{3r} R_p)$

$V = \frac{H_n^1(k_{2r} R_p) \cos\alpha}{\rho_2 c_2}$, $W = -\frac{H_n^2(k_{2r} R_p) \cos\alpha}{\rho_2 c_2}$

$X = -\frac{H_n^1(k_{3r} R_p) \cos\alpha}{\rho_3 c_3}$, $Y = \frac{H_n^2(k_{3r} R_p) \cos\alpha}{\rho_3 c_3}$

$Z = \rho_{s2} h_2 \omega^2 - K_2 k_{1z}^2 - \frac{K_2(1-\mu_2)n^2}{2R_2^2}$, $A1 = -\frac{iK_2 k_{1z} n(1+\mu_2)}{2R_2}$, $B1 = -\frac{iK_2 \mu_2 k_{1z}}{R_2}$

$C1 = \frac{iK_2 k_{1z} n(1+\mu_2)}{2R_2}$, $D1 = \rho_{s2} h_2 \omega^2 - \frac{K_2 k_{1z}^2 (1-\mu_2)}{2} - \frac{K_2 n^2}{R_2^2} - \frac{D_2 k_{1z}^2 (1-\mu_2)}{2R_2^2} - \frac{D_2 n^2}{R_2^4}$

$E1 = -\frac{K_2 n}{R_2^2} - \frac{D_2 k_{1z}^2 n}{R_2^2} - \frac{D_2 n^3}{R_2^4}$

$F1 = H_n^1(k_{3r} R_2)$, $G1 = H_n^2(k_{3r} R_2)$, $H1 = -H_n^1(k_{4r} R_2)$

$I1 = \frac{iK_2\mu_1 k_{1z}}{R_2},\ J1 = -\frac{K_2 n}{R_2^2} - \frac{D_2 k_{1z}^2 n}{R_2^2} - \frac{D_2 n^3}{R_2^4}$

$K1 = \rho_{s2} h_2 \omega^2 - D_2 k_{1z}^4 - \frac{2D_2 k_{1z}^2 n^2}{R_2^2} - \frac{D_2 n^4}{R_2^4} - \frac{K_2}{R_2^2}$

$L1 = k_{3r} H_n^{1\prime}(k_{3r} R_2),\ M1 = k_{3r} H_n^{2\prime}(k_{3r} R_2),\ N1 = -\rho_3 \omega^2$

$O1 = k_{4r} H_n^{1\prime}(k_{4r} R_2),\ P1 = -\rho_t \omega^2$

$Q1 = -p_0 \varepsilon_n (-i)^n J_n(k_{1r} R_1),\ R1 = -p_0 \varepsilon_n (-i)^n k_{1r} J_n'(k_{1r} R_1)$

Appendix G

Matrix formulation of the cylindrical shell system in the UU configuration

Figure 4.1c shows that the double shells lined with porous in the UU configuration. It consists of incident region, porous material region, two air gaps and transmitted region. The fluid medium in the two air gap regions have physical property (ρ_2, c_2) and (ρ_4, c_4), respectively. Because the airborne wave is the dominant wave in this configuration, $\rho_3 = \rho_{22}^*$ is treated as the equivalent density of porous material layer over the entire frequency range. The pressure in each region can be expressed as

$$p_1^R(r,\theta,z,t) = \sum_{n=0}^{\infty} p_{1n}^R H_n^2(k_{1r}r) \cos n\theta e^{i(\omega t - k_{1z}z)} \tag{G.1}$$

$$p_2^T(r,\theta,z,t) = \sum_{n=0}^{\infty} p_{2n}^T H_n^1(k_{1r}r) \cos n\theta e^{i(\omega t - k_{1z}z)} \tag{G.2}$$

$$p_2^R(r,\theta,z,t) = \sum_{n=0}^{\infty} p_{2n}^R H_n^2(k_{1r}r) \cos n\theta e^{i(\omega t - k_{1z}z)} \tag{G.3}$$

$$p_3^T(r,\theta,z,t) = \sum_{n=0}^{\infty} p_{3n}^T H_n^1(k_{1r}r) \cos n\theta e^{i(\omega t - k_{1z}z)} \tag{G.4}$$

$$p_3^R(r,\theta,z,t) = \sum_{n=0}^{\infty} p_{3n}^R H_n^2(k_{1r}r) \cos n\theta e^{i(\omega t - k_{1z}z)} \tag{G.5}$$

$$p_4^T(r,\theta,z,t) = \sum_{n=0}^{\infty} p_{4n}^T H_n^1(k_{1r}r) \cos n\theta e^{i(\omega t - k_{1z}z)} \tag{G.6}$$

$$p_4^R(r,\theta,z,t) = \sum_{n=0}^{\infty} p_{4n}^R H_n^2(k_{1r}r) \cos n\theta e^{i(\omega t - k_{1z}z)} \tag{G.7}$$

$$p_5^T(r,\theta,z,t) = \sum_{n=0}^{\infty} p_{5n}^T H_n^1(k_{1r}r)\cos n\theta e^{i(\omega t - k_{1z}z)} \tag{G.8}$$

The wave numbers in Eqs.(G.1)-(G.8) are defined as

$$k_1 = \frac{\omega}{c_i}\frac{1}{1+M\sin(\alpha)},\ k_{1r} = k_1\cos\alpha,\ k_{1z} = k_1\sin\alpha. \tag{G.9}$$

$$k_2 = \frac{\omega}{c_2},\ k_{2z} = k_{1z},\ k_{2r} = \sqrt{k_2^2 - k_{2z}^2}. \tag{G.10}$$

$$k_{3z} = k_{1z},\ k_{3r} = \sqrt{k_{\mathrm{I}}^2 - k_{3z}^2} \tag{G.11}$$

$$k_4 = \frac{\omega}{c_4},\ k_{4z} = k_{1z},\ k_{4r} = \sqrt{k_4^2 - k_{4z}^2}. \tag{G.12}$$

$$k_5 = \frac{\omega}{c_t},\ k_{5z} = k_{1z},\ k_{5r} = \sqrt{k_5^2 - k_{5z}^2}. \tag{G.13}$$

The governing equations for the two shells are

$$L_1\{u_1^0, v_1^0, w_1^0\} = \rho_{s1}h_1\ddot{u}_1^0 \tag{G.14}$$

$$L_2\{u_1^0, v_1^0, w_1^0\} = \rho_{s1}h_1\ddot{v}_1^0 \tag{G.15}$$

$$L_3\{u_1^0, v_1^0, w_1^0\} + [(p_1^I + p_1^R) - (p_2^T + p_2^R)] = \rho_{s1}h_1\ddot{w}_1^0 \tag{G.16}$$

$$L_1\{u_2^0, v_2^0, w_2^0\} = \rho_{s2}h_2\ddot{u}_2^0 \tag{G.17}$$

$$L_2\{u_2^0, v_2^0, w_2^0\} = \rho_{s2}h_2\ddot{v}_2^0 \tag{G.18}$$

$$L_3\{u_2^0, v_2^0, w_2^0\} + [(p_4^T + p_4^R) - p_5^T] = \rho_{s2}h_2\ddot{w}_2^0 \tag{G.19}$$

Boundary conditions:

$$\frac{\partial(p_1^I + p_1^R)}{\partial r} = -\rho_i \left(\frac{\partial}{\partial t} + \mathbf{V}\cdot\nabla\right)^2 w_1^0 \bigg|_{r=R_1} \tag{G.20}$$

$$\frac{\partial(p_2^T + p_2^R)}{\partial r} = -\rho_2 \frac{\partial^2 w_1^0}{\partial t^2}\bigg|_{r=R_1} \tag{G.21}$$

$$p_2^T + p_2^R = p_3^T + p_3^R\big|_{r=R_{p1}} \tag{G.22}$$

$$v_2^T + v_2^R = v_3^T + v_3^R\big|_{r=R_{p1}} \tag{G.23}$$

$$p_3^T + p_3^R = p_4^T + p_4^R\big|_{r=R_{p2}} \tag{G.24}$$

$$v_3^T + v_3^R = v_4^T + v_4^R\big|_{r=R_{p2}} \tag{G.25}$$

$$\frac{\partial(p_4^T + p_4^R)}{\partial r} = -\rho_4 \frac{\partial^2 w_2^0}{\partial t^2}\bigg|_{r=R_2} \tag{G.26}$$

$$\frac{\partial p_5^T}{\partial r} = -\rho_t \frac{\partial^2 w_2^0}{\partial t^2}\bigg|_{r=R_2} \tag{G.27}$$

where R_{p1} and R_{p2} are the radius of the interface between porous material layer and the two air gaps, respectively. v_2^T, v_2^R, v_3^T, v_3^R, v_4^T and v_4^R are the particle velocities in the acoustic space.

These fourteen equations can be put into a matrix form as

$$\begin{bmatrix}
0 & 0 & 0 & 0 & 0 & 0 & 0 & 0 & A & B & C & 0 & 0 & 0 \\
0 & 0 & 0 & 0 & 0 & 0 & 0 & 0 & D & E & F & 0 & 0 & 0 \\
G & H & I & 0 & 0 & 0 & 0 & 0 & J & K & L & 0 & 0 & 0 \\
M & 0 & 0 & 0 & 0 & 0 & 0 & 0 & 0 & 0 & N & 0 & 0 & 0 \\
0 & O & P & 0 & 0 & 0 & 0 & 0 & 0 & 0 & Q & 0 & 0 & 0 \\
0 & R & S & T & U & 0 & 0 & 0 & 0 & 0 & 0 & 0 & 0 & 0 \\
0 & V & W & X & Y & 0 & 0 & 0 & 0 & 0 & 0 & 0 & 0 & 0 \\
0 & 0 & 0 & Z & A1 & B1 & C1 & 0 & 0 & 0 & 0 & 0 & 0 & 0 \\
0 & 0 & 0 & D1 & E1 & F1 & G1 & 0 & 0 & 0 & 0 & 0 & 0 & 0 \\
0 & 0 & 0 & 0 & 0 & 0 & 0 & 0 & 0 & 0 & 0 & H1 & I1 & J1 \\
0 & 0 & 0 & 0 & 0 & 0 & 0 & 0 & 0 & 0 & 0 & K1 & L1 & M1 \\
0 & 0 & 0 & 0 & 0 & N1 & O1 & P1 & 0 & 0 & 0 & Q1 & R1 & S1 \\
0 & 0 & 0 & 0 & 0 & T1 & U1 & 0 & 0 & 0 & 0 & 0 & 0 & V1 \\
0 & 0 & 0 & 0 & 0 & 0 & 0 & W1 & 0 & 0 & 0 & 0 & 0 & X1
\end{bmatrix}
\begin{Bmatrix}
p_{1n}^R \\ p_{2n}^T \\ p_{2n}^R \\ p_{3n}^T \\ p_{3n}^R \\ p_{4n}^T \\ p_{4n}^R \\ p_{5n}^T \\ u_{1n}^0 \\ v_{1n}^0 \\ w_{1n}^0 \\ u_{2n}^0 \\ v_{2n}^0 \\ w_{2n}^0
\end{Bmatrix}
=
\begin{Bmatrix}
0 \\ 0 \\ Y1 \\ Z1 \\ 0 \\ 0 \\ 0 \\ 0 \\ 0 \\ 0 \\ 0 \\ 0 \\ 0 \\ 0
\end{Bmatrix} \tag{G.28}$$

where

$A = \rho_{s1} h_1 \omega^2 - K_1 k_{1z}^2 - \frac{K_1(1-\mu_1)n^2}{2R_1^2}$, $B = -\frac{iK_1 k_{1z} n(1+\mu_1)}{2R_1}$, $C = -\frac{iK_1 \mu_1 k_{1z}}{R_1}$

$D = \frac{iK_1 k_{1z} n(1+\mu_1)}{2R_1}$, $E = \rho_{s1} h_1 \omega^2 - \frac{K_1 k_{1z}^2(1-\mu_1)}{2} - \frac{K_1 n^2}{R_1^2} - \frac{D_1 k_{1z}^2(1-\mu_1)}{2R_1^2} - \frac{D_1 n^2}{R_1^4}$

$F = -\frac{K_1 n}{R_1^2} - \frac{D_1 k_{1z}^2 n}{R_1^2} - \frac{D_1 n^3}{R_1^4}$, $G = H_n^2(k_{1r} R_1)$, $H = -H_n^1(k_{2r} R_1)$

$I = -H_n^2(k_{2r} R_1)$, $J = \frac{iK_1 \mu_1 k_{1z}}{R_1}$, $K = -\frac{D_1 k_{1z}^2 n}{R_1^2} - \frac{D_1 n^3}{R_1^4} - \frac{K_1 n}{R_1^2}$

$L = \rho_{s1} h_1 \omega^2 - D_1 k_{1z}^4 - \frac{2D_1 k_{1z}^2 n^2}{R_1^2} - \frac{D_1 n^4}{R_1^4} - \frac{K_1}{R_1^2}$

$M = k_{1r} H_n^{2\prime}(k_{1r} R_1)$, $N = -\rho_i(\omega - V k_{1z})^2$

$O = k_{2r} H_n^{1\prime}(k_{2r} R_1)$, $P = k_{2r} H_n^{2\prime}(k_{2r} R_1)$, $Q = -\rho_2 \omega^2$

$R = H_n^1(k_{2r} R_{p1})$, $S = H_n^2(k_{2r} R_{p1})$, $T = -H_n^1(k_{3r} R_{p1})$, $U = -H_n^2(k_{3r} R_{p1})$

$V = \frac{H_n^1(k_{2r} R_{p1}) \cos\alpha}{\rho_2 c_2}$, $W = -\frac{H_n^2(k_{2r} R_{p1}) \cos\alpha}{\rho_2 c_2}$

$X = -\frac{H_n^1(k_{3r} R_{p1}) \cos\alpha}{\rho_3 c_3}$, $Y = \frac{H_n^2(k_{3r} R_{p1}) \cos\alpha}{\rho_3 c_3}$

$Z = H_n^1(k_{3r} R_{p2})$, $A1 = H_n^2(k_{3r} R_{p2})$, $B1 = -H_n^1(k_{4r} R_{p2})$, $C1 = -H_n^2(k_{4r} R_{p2})$

$D1 = \frac{H_n^1(k_{3r} R_{p2}) \cos\alpha}{\rho_3 c_3}$, $E1 = -\frac{H_n^2(k_{3r} R_{p2}) \cos\alpha}{\rho_3 c_3}$

$F1 = -\frac{H_n^1(k_{4r} R_{p2}) \cos\alpha}{\rho_4 c_4}$, $G1 = \frac{H_n^2(k_{4r} R_{p2}) \cos\alpha}{\rho_4 c_4}$

$H1 = \rho_{s2} h_2 \omega^2 - K_2 k_{1z}^2 - \frac{K_2(1-\mu_2)n^2}{2R_2^2}$, $I1 = -\frac{iK_2 k_{1z} n(1+\mu_2)}{2R_2}$, $J1 = -\frac{iK_2 \mu_2 k_{1z}}{R_2}$

$K1 = \frac{iK_2 k_{1z} n(1+\mu_2)}{2R_2}$, $L1 = \rho_{s2} h_2 \omega^2 - \frac{K_2 k_{1z}^2(1-\mu_2)}{2} - \frac{K_2 n^2}{R_2^2} - \frac{D_2 k_{1z}^2(1-\mu_2)}{2R_2^2} - \frac{D_2 n^2}{R_2^4}$

$M1 = -\frac{K_2 n}{R_2^2} - \frac{D_2 k_{1z}^2 n}{R_2^2} - \frac{D_2 n^3}{R_2^4}$

$N1 = H_n^1(k_{4r} R_2)$, $O1 = H_n^2(k_{4r} R_2)$, $P1 = -H_n^1(k_{5r} R_2)$

$Q1 = \frac{iK_2 \mu_1 k_{1z}}{R_2}$, $R1 = -\frac{K_2 n}{R_2^2} - \frac{D_2 k_{1z}^2 n}{R_2^2} - \frac{D_2 n^3}{R_2^4}$

$S1 = \rho_{s2} h_2 \omega^2 - D_2 k_{1z}^4 - \frac{2D_2 k_{1z}^2 n^2}{R_2^2} - \frac{D_2 n^4}{R_2^4} - \frac{K_2}{R_2^2}$

$T1 = k_{4r} H_n^{1\prime}(k_{4r} R_2)$, $U1 = k_{4r} H_n^{2\prime}(k_{4r} R_2)$, $V1 = -\rho_4 \omega^2$

$W1 = k_{5r} H_n^{1\prime}(k_{5r} R_2)$, $X1 = -\rho_t \omega^2$

$Y1 = -p_0 \varepsilon_n (-i)^n J_n(k_{1r} R_1)$, $Z1 = -p_0 \varepsilon_n (-i)^n k_{1r} J_n'(k_{1r} R_1)$

Appendix H

BU configuration under TBL excitation

Figure 5.1b shows that double shells lined with porous in the BU configuration. The fluid medium in the air gap region has physical property (ρ_3, c_3). $\rho_2 = \rho_{22}^*$ is treated as the equivalent density of porous material layer in the low frequency range, while $\rho_2 = \rho_{11}^*$ in high frequency range [81]. The pressure in porous material, air gap and interior cavity can be respectively expressed as

$$\begin{aligned} p_2 &= \sum_{m=1,n=0}^{\infty} \left[p_{21mn} J_n(k_{2rm} r) + p_{2mn} Y_n(k_{2rm} r)\right] \Psi_{mn}(x,\theta) && \text{(H.1)} \\ p_3 &= \sum_{m=1,n=0}^{\infty} \left[p_{31mn} J_n(k_{3rm} r) + p_{32mn} Y_n(k_{3rm} r)\right] \Psi_{mn}(x,\theta) && \text{(H.2)} \\ p_4 &= \sum_{m=1,n=0}^{\infty} p_{4mn} J_n(k_{4rm} r) \Psi_{mn}(x,\theta) && \text{(H.3)} \end{aligned}$$

where $k_{2rm}^2 = k_2^2 - (m\pi/L)^2$, $k_{3rm}^2 = k_3^2 - (m\pi/L)^2$ and $k_{4rm}^2 = k_4^2 - (m\pi/L)^2$. $k_2 = k_{\mathrm{I}}$ is referred to as the airborne wave in low frequency range, $k_2 = k_{\mathrm{II}}$ is referred to as the frame wave in high frequency range [81]. p_{21mn}, p_{22mn}, p_{31mn}, p_{32mn} and p_{4mn} are unknown model coefficients.

At the interfaces between the elastic shells and the fluids, the following boundary conditions must be satisfied

$$\frac{\partial p_2}{\partial r} = \rho_2 \omega^2 w_1 \bigg|_{r=R_1} \tag{H.4}$$

$$p_2 = p_3 \big|_{r=R_p} \tag{H.5}$$

$$v_2 = v_3 \big|_{r=R_p} \tag{H.6}$$

$$\frac{\partial p_3}{\partial r} = \rho_3 \omega^2 w_2 \bigg|_{r=R_2} \tag{H.7}$$

$$\frac{\partial p_4}{\partial r} = \rho_i \omega^2 w_2 \bigg|_{r=R_2} \tag{H.8}$$

where the radius of the porous material bottom surface R_p equals $R_1 - h_p$.

Substituting the displacements Eqs.(5.12)-(5.14) and pressures Eqs.(H.1)-(H.3) into the shell motion equations Eqs.(5.1)-(5.3) and the boundary conditions Eqs.(H.4)-(H.8), the unknown model coefficients vector $\mathbf{x} = \{p_{21mn}, p_{22mn}, p_{31mn}, p_{32mn}, p_{4mn}, u_{1mn}, v_{1mn}, w_{1mn}, u_{2mn}, v_{2mn}, w_{2mn}\}$ can be obtained as

$$\mathbf{x} = \mathbf{H} p_{1mn} \tag{H.9}$$

where $\mathbf{H} = \{H_{p21mn}, H_{p22mn}, H_{p31mn}, H_{p32mn}, H_{p4mn}, H_{u1mn}, H_{v1mn}, H_{w1mn}, H_{u2mn}, H_{v2mn}, H_{w2mn}\}$ is a vector of frequency response functions due to the modal excitation p_{1mn} of the turbulent boundary layer.

Appendix I

UU configuration under TBL excitation

Figure 5.1c shows that double shells lined with porous in the UU configuration. The fluid medium in the two air gap regions have physical property (ρ_2, c_2) and (ρ_4, c_4), respectively. Since the airborne wave is the dominant wave in this configuration, $\rho_3 = \rho_{22}^{*}$ is treated as the equivalent density of porous material layer over the entire frequency range [81]. The pressure in air gap 1, porous material, air gap 2 and interior cavity can be respectively expressed as

$$p_2 = \sum_{m=1,n=0}^{\infty} \left[p_{21mn} J_n(k_{2rm} r) + p_{2mn} Y_n(k_{2rm} r)\right] \Psi_{mn}(x, \theta) \tag{I.1}$$

$$p_3 = \sum_{m=1,n=0}^{\infty} \left[p_{31mn} J_n(k_{3rm} r) + p_{32mn} Y_n(k_{3rm} r)\right] \Psi_{mn}(x, \theta) \tag{I.2}$$

$$p_4 = \sum_{m=1,n=0}^{\infty} \left[p_{41mn} J_n(k_{4rm} r) + p_{42mn} Y_n(k_{4rm} r)\right] \Psi_{mn}(x, \theta) \tag{I.3}$$

$$p_5 = \sum_{m=1,n=0}^{\infty} p_{5mn} J_n(k_{4rm} r) \Psi_{mn}(x, \theta) \tag{I.4}$$

where $k_{2rm}^2 = k_2^2 - (m\pi/L)^2$, $k_{3rm}^2 = k_3^2 - (m\pi/L)^2$, $k_{4rm}^2 = k_4^2 - (m\pi/L)^2$ and $k_{5rm}^2 = k_5^2 - (m\pi/L)^2$. $k_3 = k_{\mathrm{I}}$ is referred to as the airborne wave entire frequency range [81]. p_{21mn}, p_{22mn}, p_{31mn}, p_{32mn}, p_{41mn}, p_{42mn} and p_{5mn} are unknown model coefficients.

At the interfaces between the elastic shells and the fluids, the following boundary conditions must be satisfied

$$\frac{\partial p_2}{\partial r} = \rho_2 \omega^2 w_1 \bigg|_{r=R_1} \tag{I.5}$$

$$p_2 = p_3|_{r=R_{p1}} \tag{I.6}$$

$$v_2 = v_3|_{r=R_{p1}} \tag{I.7}$$

$$p_3 = p_4|_{r=R_{p2}} \tag{I.8}$$

$$v_3 = v_4|_{r=R_{p2}} \tag{I.9}$$

$$\frac{\partial p_4}{\partial r} = \rho_4 \omega^2 w_2 \bigg|_{r=R_2} \tag{I.10}$$

$$\frac{\partial p_5}{\partial r} = \rho_i \omega^2 w_2 \bigg|_{r=R_2} \tag{I.11}$$

where R_{p1} and R_{p2} are the radius of the interface between porous material layer and the two air gaps, respectively.

Substituting the displacements Eqs.(5.12)-(5.14) and pressures Eqs.(I.1)-(I.4) into the shell motion equations Eqs.(5.1)-(5.3) and the boundary conditions Eqs.(I.5)-(I.11), the unknown model coefficients vector $\mathbf{x} = \{p_{21mn}, p_{22mn}, p_{31mn}, p_{32mn}, p_{41mn}, p_{42mn}, p_{5mn}, u_{1mn}, v_{1mn}, w_{1mn}, u_{2mn}, v_{2mn}, w_{2mn}\}$ can be obtained as

$$\mathbf{x} = \mathbf{H} p_{1mn} \tag{I.12}$$

where $\mathbf{H} = \{H_{p21mn}, H_{p22mn}, H_{p31mn}, H_{p32mn}, , H_{p41mn}, H_{p42mn} H_{p5mn}, H_{u1mn}, H_{v1mn}, H_{w1mn}, H_{u2mn}, H_{v2mn}, H_{w2mn}\}$ is a vector of frequency response functions due to the modal excitation p_{1mn} of the turbulent boundary layer.

Bibliography

[1] Mixson, J. S., and Wilby, J. F., 1991. *Interior Noise in Aeroacoustic of Flight Vehicles: Theory and Practice.* NASA Reference Pbulication 1258, Vol. 2.

[2] Neple, P., 2010. "Interior noise and sound transmission". *Encyclopedia of Aerospace Engineering.*

[3] Wilby, J. F., 1996. "Aircraft interior noise". *Journal of Sound and Vibration,* ***190***(3), pp. 545–564.

[4] D'Angelo, J. P., 2004. "Attenuation of turbulent boundary layer induced interior noise using intergarted smart foam elements". PhD thesis, Virginia Polytechnic Institute and State University, VA, USA.

[5] Idrisi, K., 2008. "Heterogeneous blankets for improved aircraft interior noise reduction". PhD thesis, Virginia Polytechnic Institute and State University, VA, USA.

[6] Piersol, A. G., and Paez, T. L., 2009. *Harris' Shock and Vibration Handbook (Six Edition).* McGraw-Hill.

[7] Hickey, D. H., 1969. "Characteristics of noise generated by ducted propellers and fans". Conference on STOL Transport Aircraft Noise Certification.

[8] Smith, M. J. T., 1989. *Aircraft Noise.* Cambridge University Press.

[9] Bhat, W. V., 1971. "Use of correlation technique for estimating in-flight noise radiated by wing-mounted jet engines on a fuselage". *Journal of Sound and Vibration,* ***17***(3), pp. 349–355.

[10] Lyrintzis, C. S., and Vaicaitis, R., 1987. "Structure-borne noise generation and transmission". *Probabilistic Engineering Mechanics,* ***2***(3), pp. 114–120.

[11] Landaluze, J., Portilla, I., Pagalday, J. M., Martinez, A., and Reyero, R., 2003. "Application of active noise control to an elevator cabin". *Control Engineering Practice,* ***11***(12), pp. 1423–1431.

[12] Roussos, L. A., Powell, C. A., Grosveld, F. W., and Koval, L. R., 1984. "Noise transmission characteristics of advanced composite structural materials". *Journal of Aircraft,* ***21***(7), pp. 528–535.

[13] Sagartzazu, X., Hervella-Nieto, L., and Pagalday, J. M., 2008. "Review in sound absorbing materials". *Archives of Computational Methods in Engineering,* ***15***(3), pp. 311–342.

[14] Tran, K. D., 2002. "Burn-through resistance of fibre/felt materials for aircraft fuselage insulation blankets". *Fire and Materials,* ***26***(1), pp. 1–6.

[15] Gandhi, S., Lyon, R., and Speitel, L., 1999. "Potential health hazards from burning aircraft composites". *Journal of Fire Sciences,* ***17***(1), pp. 20–41.

[16] Grooteman, F. P., 2006. "Transmission loss analyses on fuselage panels". *National Aerospace Laboratory NLR Report,* ***479***, pp. 1–24.

[17] C. Resewski, W. B., 2003. "Properties of new polyimide foams and polyimide foam filled honeycomb composites". *Materialwissenschaft und Werkstofftechnik,* ***34***(4), pp. 365–369.

[18] Silcox, R. J., Cano, R. J., Howerton, B., Bolton, J. S., and Kim, N. N., 2013. "Development of polymide foam for aircraft sidewall applicants". 51st AIAA Aerospace Science Meeting.

[19] Foams, S. *Guidance of AC-530 polyimide foam.* Evonik Industries, USA.

[20] Renninger, J. *Aircraft interior acoustic.* Structural Test Article.

[21] Rao, M. D., 2003. "Recent applications of viscoelastic damping for noise control in automobiles and commercial airplanes". *Journal of Sound and Vibration,* ***262***(1), pp. 457–474.

[22] Gardonio, P., 2010. "Active noise control". *Encyclopedia of Aerospace Engineering.*

[23] Ozcan, H. K., and Nemlioglu, S., 2006. "In-cabin noise levels during commercial aircraft flights". *Canadian Acoustics,* ***34***(4), pp. 31–35.

[24] Campolina, B. L., 2012. “Vibro-acoustic modelling of aircraft double-walls with structural links using statistical energy analysis”. PhD thesis, Airbus Operations SAS, Acoustic and Environmental Department, Toulouse, France.

[25] London, A., 1950. “Transmission of reverberant sound through double walls”. *Journal of the Acoustical Society of America,* ***22***(2), pp. 270–279.

[26] Mulholland, K. A., Parbrook, H. D., and Cummings, A., 1967. “The transmission loss of double panels”. *Journal of Sound and Vibration,* ***6***(3), pp. 324–334.

[27] Legault, J., and Atalla, N., 2010. “Sound transmission through a double panel structure periodically coupled with vibration insulators”. *Journal of Sound and Vibration,* ***329***(15), pp. 3082–3100.

[28] Bolton, J. S., Shiau, N. M., and Kang, Y. J., 1996. “Sound transmission through multi-panel structures lined with elastic porous materials”. *Journal of Sound and Vibration,* ***191***(3), pp. 317–347.

[29] Biot, M. A., 1956. “Theory of propagation of elastic waves in a fluid-saturated porous solid. I. Low-frequency range”. *Journal of the Acoustical Society of America,* ***28***(2), pp. 168–178.

[30] Wang, J., Lu, T. J., Woodhouse, J., Langley, R. S., and Evans, J., 2005. “Sound transmission through lightweight double-leaf partitions: theoretical modeling”. *Journal of Sound and Vibration,* ***286***(4), pp. 817–847.

[31] Ingard, K. U., 1959. “Influence of fluid motion past a plane boundary on sound refection, absorption, and transmission”. *Journal of the Acoustical Society of America,* ***31***(7), pp. 1035–1036.

[32] Koval, L. R., 1976. “Effect of air flow, panel curvature, and internal pressurization on field-incidence transmission loss”. *Journal of the Acoustical Society of America,* ***59***(6), pp. 1379–1385.

[33] Xin, F. X., Lu, T. J., and Chen, C. Q., 2009. “External mean flow influence on noise transmission through double-leaf aeroelastic plates”. *AIAA Journal,* ***47***(8), pp. 1939–1951.

[34] Xin, F. X., and Lu, T. J., 2010. “Analytical modeling of sound transmission across finite aeroelastic panels in convected fluids”. *Journal of the Acoustical Society of America,* ***128***(3), pp. 1097–1107.

[35] Koval, L. R., 1976. “On sound transmission into a thin cylindrical shell under flight condition”. *Journal of Sound and Vibration,* ***48***(2), pp. 265–275.

[36] Koval, L. R., 1978. “Effects of cavity resonances on sound transmission into a thin cylindrical shell”. *Journal of Sound and Vibration,* ***59***(1), pp. 23–33.

[37] Koval, L. R., 1979. “On sound transmission into an orthotropic shell”. *Journal of Sound and Vibration,* ***63***(8), pp. 51–59.

[38] Koval, L. R., 1980. “Sound transmission into a laminated composite cylindrical shell”. *Journal of Sound and Vibration,* ***71***(4), pp. 523–530.

[39] Liu, B. L., Feng, L. P., and Nilsson, A., 2007. “Influence of overpressure on sound transmission through curved panels”. *Journal of Sound and Vibration,* ***302***(4), pp. 760–776.

[40] Lee, J. H., and Kim, J., 2003. “Study on sound transmission characteristics of a cylindrical shell using analytical and experimental models”. *Applied acoustics,* ***64***(6), pp. 611–632.

[41] Lee, J. H., and Kim, J., 2002. “Analysis and measurement of sound transmission through a double walled cylindrical shell”. *Journal of Sound and Vibration,* ***251***(4), pp. 631–649.

[42] Tang, Y. Y., Robinson, J. H., and Richard, J. S., 1996. “Sound transmission through a cylindrical sandwich shell with honeycomb core”. 34th AIAA Aerospace Sciences Meeting and Exhibit.

[43] Tang, Y. Y., Robinson, J. H., and Richard, J. S., 1996. “Sound transmission through two concentric cylindrical sandwich shells”. Proceedings of 14th International Modal Analysis Conference.

[44] Liu, B., and Feng, L., 2003. “Sound transmission through a double walled cylindrical shell”. Tenth International Congress on Sound and Vibration.

[45] Cousin, G., 1998. "Sound from TBL-induced vibrations". 4th AIAA/CEAS Aeroacoustics Conference.

[46] Bishop, D. E., 1961. "Cruise flight noise levels in a turbojet transport airplane.". *Noise Control,* ***7***(2), pp. 37–42.

[47] Dowell, E. H., 1969. "Transmission of noise from a turbulent boundary layer through a flexible plate into a closed cavity". *Journal of the Acoustical Society of America,* ***46***(1), pp. 238–252.

[48] Davies, H. G., 1971. "Sound from turbulent-boundary-layer-excited panels". *Journal of the Acoustical Society of America,* ***49***(3), pp. 878–889.

[49] Tang, Y. Y., Silcox, R. J., and Robinson, J. H., 1996. "Modeling of sound transmission through shell structures with turbulent boundary layer excitation". Proceedings of the 1996 National Conference on Noise Control Engineering.

[50] Tang, Y. Y., Silcox, R. J., and Robinson, J. H., 1996. "Sound transmission through cylindrical shell structures excited by boundary layer pressure fluctuations". 2nd AIAA/CEAS Aeroacoustics Conference.

[51] Maury, C., Gardonio, P., and Elliott, S. J., 2002. "Model for active control of flow-induced noise transmitted through double partitions". *AIAA Journal,* ***40***(6), pp. 1113–1121.

[52] Graham, W. R., 1996. "Boundary layer induced noise in aircraft, part I: the flat plate model". *Journal of Sound and Vibration,* ***192***(1), pp. 101–120.

[53] Graham, W. R., 1996. "Boundary layer induced noise in aircraft, part ii: the trimmed flat plate model". *Journal of Sound and Vibration,* ***192***(1), pp. 121–138.

[54] Maury, C., Gardonio, P., and Elliott, S. J., 2002. "A wavenumber approach to modelling the response of a randomly excited panel, part I: general theory". *Journal of Sound and Vibration,* ***252***(1), pp. 83–113.

[55] Maury, C., Gardonio, P., and Elliott, S. J., 2002. "A wavenumber approach to modelling the response of a randomly excited panel, part II: application to aircraft panels excited by a turbulent boundary layer". *Journal of Sound and Vibration,* ***252***(1), pp. 115–139.

[56] Liu, B., Feng, L., Nilsson, A., and Aversano, M., 2012. "Predicted and measured plate velocities induced by turbulent boundary layers". *Journal of Sound and Vibration,* ***331***(24), pp. 5309–5325.

[57] Gardonio, P., 2013. "Boundary layer noise–part 2: interior noise radiation and control". *Fundamentals and Applications,* ***545***, pp. 379–448.

[58] Bies, D. A., and Hansen, C. H., 2003. *Engineering Noise Control.* Spon Press, London.

[59] Gibson, L. J., and Ashby, M. F., 1997. *Cellular Solids: Structures and Properties (Second Edition),.* Cambridge University Press.

[60] Lu, T. J., Kepets, M., and Dowling, A. P., 2008. "Acoustic properties of sintered fecraly foams with open cells (I): Static flow resistance". *Science in China Series E: Technological Sciences,* ***51***(11), pp. 1803–1811.

[61] Mills, N. J., Stpfli, R., Marone, F., and Brhwiler, P. A., 2009. "Finite element micromechanics model of impact compression of closed-cell polymer foams". *International Journal of Solids and Structures,* ***46***(3–4), pp. 677–697.

[62] Allard, J. F., and Atalla, N., 2009. *Propagation of Sound in Porous Media: Modelling Sound Absorbing Materials.* John Wiley and Sons, Ltd., West Sussex.

[63] Champoux, Y., Stinson1, M. R., and Daigle1, G. A., 1991. "Air-based system for the measurement of porosity". *Journal of the Acoustical Society of America,* ***89***(2), pp. 910–916.

[64] Johnson, D. L., Koplik, J., and Dashen, R., 1987. "Theory of dynamic permeability and tortuosity in fluid-saturated porous media". *Journal of Fluid Mechanics,* ***176***, pp. 379–402.

[65] Delaney, M. E., and Bazley, E. N., 1970. "Acoustical properties of fibrous absorbent materials". *Applied Acoustics,* ***3***(2), pp. 105–116.

[66] Bies, D. A., and Hansen, C. H., 1980. "Flow resistance information for acoustical design". *Applied Acoustics,* ***13***(5), pp. 357–391.

[67] Zwikker, C., and Kosten, C. W., 1949. *Sound Absorbing Materials.* Elsevier, New York.

[68] Champoux, Y., and Allard, J., 1991. "Dynamic tortuosity and bulk modulus in air-saturated porous media". *Journal of Applied Physics,* ***70***(4), pp. 1975–1979.

[69] Pride, S. R., Morgan, F. D., and Gangi, A. F., 1993. "Drag forces of porous-medium acoustics". *Physical Review B,* ***47***(9), pp. 4964?–4978.

[70] Lafarge, D., Lemarinier, P., and Allard, J. F., 1997. "Dynamic compressibility of air in porous structures at audible frequencies". *Journal of the Acoustical Society of America,* ***102***(4), pp. 1995–2006.

[71] Attenborough, K., 1982. "Acoustical characteristics of porous materials". *Physics Reports,* ***82***(3), pp. 179–227.

[72] Atalla, N., Panneton, R., and Debergue, P., 1998. "A mixed displacement-pressure formulation for poroelastic materials". *Journal of the Acoustical Society of America,* ***104***(3), pp. 1444–1452.

[73] Kidner, M. R. F., and Hansen, C. H., 2008. "A comparison and review of theories of the acoustics of porous materials". *International Journal of Acoustics and Vibration,* ***13***(3), pp. 112–119.

[74] Forest, L., Gibiat, V., and Woignier, T., 1998. "Biot's theory of acoustic propagation in porous media applied to aerogels and alcogels". *Journal of Non-Crystalline Solids,* ***225***(1), pp. 287–292.

[75] Dazel, O., and Tournat, V., 2010. "Nonlinear biot waves in porous media with application to unconsolidated granular media". *Journal of the Acoustical Society of America,* ***127***(2), pp. 692–702.

[76] Dalrymple, R. A., Losada, M. A., and Martin, P. A., 1990. "Reflection and transmission from porous structures under oblique wave attack". *Journal of Fluid Mechanics,* ***224***, pp. 625–644.

[77] Berryman, J. G., 1988. "Seismic wave attenuation in fluid-saturated porous media". *Pure and Applied Geophysics,* ***128***(1–2), pp. 423–432.

[78] Hosokawa, A., and Otani, T., 1997. "Ultrasonic wave propagation in bovine cancellous bone". *Journal of the Acoustical Society of America,* ***101***(1), pp. 558–562.

[79] McKelvie, M. L., and Palmer, S. B., 1991. “The interaction of ultrasound with cancellous bone”. *Physics in Medicine and Biology,* ***36***(10), pp. 1331–1340.

[80] Cremer, L., Heckl, M., and Ungar, E. E., 1973. *Structure-borne Sound.* Springer, Berlin.

[81] Lee, J. H., Kim, J., and Kim, H. J., 2001. “Simplified method to solve sound transmission through structures lined with elastic porous material”. *Journal of the Acoustical Society of America,* ***110***(5), pp. 2282–2294.

[82] Panneton, R., and Atalla, N., 1996. “Numerical prediction of sound transmission through finite multilayer systems with poroelastic materials”. *Journal of the Acoustical Society of America,* ***100***(1), pp. 346–354.

[83] Díaz-Cereceda, C., Poblet-Puig, J., and Rodríguez-Ferran, A., 2012. “The finite layer method for modelling the sound transmission through double walls”. *Journal of Sound and Vibration,* ***331***(22), pp. 4884–4900.

[84] Fahy, F., and Gardonio, P., 2007. *Sound and Structural Vibration Radiation, Transmission and Response.* Elsevier, Oxford.

[85] Norton, M. P., and Karczub, D. G., 2003. *Fundamentals of Noise and Vibration Analysis for Engineers.* Cambridge University Press, Cambridge.

[86] Makris, S. E., Dym, C. L., and Smith, M., 1986. “Transmission loss optimization in acoustic sandwich panels”. *Journal of the Acoustical Society of America,* ***79***(6), pp. 1833–1843.

[87] Morse, P. M., and Ingard, K. U., 1968. *Theoretical Aoustics.* McGraw-Hill.

[88] Blauert, J., and Xiang, N., 2009. *Acoustics for Engineers Troy Lectures (Second Edition).* Springer, Berlin.

[89] Yerges, L. F., 1978. *Sound Noise and Vibration Control (Second Edition).* Van Nostrand Reinhold, New York.

[90] Cao, Y., 2007. “Pareto front in file exchange of matlab central”. MathWorks, Inc.

[91] Qatu, M. S., 2004. *Vibration of Laminated Shells and Plates.* Elsevier Academic Press.

[92] Matsikoudi-Iliopoulou, M., and Trochidis, A., 1992. “Sound transmission through composite laminates”. *Acustica,* ***76***(7), pp. 38–44.

[93] Soedel, W., 1993. *Vibrations of Shells and Plates.* Marcel Dekker, New York.

[94] Blaise, A., Lesueur, C., Cotteland, M., and Barbe, D., 1991. “On sound transmission into an orthotropic infinite shell: comparison with koval’s results and understanding of phenomena”. *Journal of Sound and Vibration,* ***150***(2), pp. 233–243.

[95] Manconi, E., and Mace, B., 2009. “Wave characterization of cylindrical and curved panels using a finite element method”. *Journal of the Acoustical Society of America,* ***125***(1), pp. 154–163.

[96] Ghinet, S., Atalla, N., and Osman, H., 2006. “Diffuse field transmission into infinite sandwich composite and laminate composite cylinders”. *Journal of Sound and Vibration,* ***289***(4–5), pp. 745–778.

[97] White, P., 1966. “Sound transmission through a finite, closed, cylindrical shell”. *Journal of the Acoustical Society of America,* ***40***(5), pp. 1124–1130.

[98] Sgard, F., Atalla, N., and Nicolas, J., 1994. “Coupled fem-bem approach for mean flow effects on vibro-acoustic behaviour of planar structures”. *AIAA Journal,* ***32***(12), pp. 2351–2358.

[99] Corcos, G. M., 1963. “Resolution of pressure in turbulence”. *Journal of the Acoustical Society of America,* ***35***(2), pp. 192–199.

[100] Efimtsov, B. M., 1982. “Characteristics of the field of turbulent wall pressure fluctuations at large reynolds numbers”. *Soviet Physics Acoustics,* ***28***(4), pp. 289–292.

[101] Miller, T. S., 2011. “Turbulent boundary layer models for acoustic analysis”. PhD thesis, Wichita State University, USA.

[102] Graham, W. R., 1997. “A comparison of models for the wavenumber–frequency spectrum of turbulent boundary layer pressures”. *Journal of Sound and Vibration,* ***206***(4), pp. 541–565.

[103] Hwang, Y. F., Bonness, W. K., and Hambric, S. A., 2009. “Comparison of semi-empirical models for turbulent boundary layer wall pressure spectra”. *Journal of Sound and Vibration,* ***319***(1–2), pp. 199–217.

[104] Airbus, 2013. *Airbus family figures.* Airbus.

[105] Koval, L. R., 1977. “Effect of stiffening on sound transmission into a cylindrical shell in flight”. *AIAA Journal,* ***15***(7), pp. 899–900.

[106] Koval, L. R., 1980. “On sound transmission into a stiffened cylindrical shell with rings and stringers treated as discrete elements”. *Journal of Sound and Vibration,* ***71***(4), pp. 511–521.

[107] Lee, J. H., and Kim, J., 2002. “Sound transmission through periodically stiffened cylindrical shells”. *Journal of Sound and Vibration,* ***251***(3), pp. 431–456.

[108] Mead, D. J., and Pujara, K. K., 1971. “Space-harmonic analysis of periodically supported beams: response to convected random loading”. *Journal of Sound and Vibration,* ***14***(4), pp. 525–541.

[109] Efimtsov, B. M., and Lazarev, L. A., 2011. “Sound pressure in cylindrical shells with regular orthogonal system of stiffeners excited by a random fields of forces”. *Journal of Sound and Vibration,* ***330***(15), pp. 3684?–3697.

[110] Liu, B. L., Feng, L. P., and Nilsson, A., 2007. “Sound transmission through curved aircraft panels with stringer and ring frame attachments”. *Journal of Sound and Vibration,* ***300***(3–5), pp. 949–973.

[111] Fuller, C. R., 1987. “Structural influence of the cabin floor on sound transmission into aircraft - analytical investigations”. *Journal of Aircraft,* ***24***(10), pp. 731–736.

[112] Missaoui, J., and Cheng, L., 1999. “Vibroacoustic analysis of a finite cylindrical shell with internal floor partition”. *Journal of Sound and Vibration,* ***226***(1), pp. 101–123.